METAL OXIDE PHOTOCATALYTIC NANOSTRUCTURES FABRICATED BY DYNAMIC SHADOWING GROWTH

By

PRADIP BASNET

(Under the Direction of Yiping Zhao)

ABSTRACT

Metal oxides (MOs) nanostructures, as visible light active photocatalysts, are widely used in applications such as solar energy conversion, biocidal coating, and environmental remediation. This dissertation investigates the morphological, structural, optical, and photocatalytic properties of some visible light active MO photocatalysts, WO_3, Cu_xO ($x = 1, 2$), and α-Fe_2O_3 nanostructures fabricated by the dynamic shadowing growth for above mentioned applications.

Dye adsorption and photodegradation property of WO_3 nanorods (NRs) has first been studied. The porous and amorphous WO_3 NRs are observed to exhibit superior methylene blue (MB) adsorption capability in aqueous solution due to its large specific surface area and active surface functionality. The adsorption of MB on the surface of WO_3 NRs are well described by Langmuir isotherm behavior. Photocatalytic MB degradation with WO_3 NRs under UV irradiation is observed to be relatively higher than that under visible light.

The solar water splitting reaction in a photoelectrochemical (PEC) cell and photocatalytic dye degradation behavior of Cu_xO ($x=1,2$) NR arrays have been studied under visible light irradiation. Both single phase Cu_2O and CuO, and mixed phase Cu_2O/CuO polycrystalline NRs are observed to exhibit excellent visible light induced photocatalytic activity for both cationic (MB) and anionic (methyl orange) dye degradation. When used as a photocathode, they also show good PEC performance, especially for the mixed phase Cu_2O/CuO NRs. The maximum stable photocurrent density is observed to be -0.24 mA/cm^2 under a simulated solar light (AM 1.5G) at an applied bias potential of -0.5 V (versus Ag/AgCl reference electrode). About 20% and 44% incident photon-to-current conversion efficiency are obtained at incident light wavelengths $\lambda = 500$ nm and 400 nm respectively.

Finally, both MB degradation and bactericidal activities are studied for the α-Fe_2O_3 NR arrays and films under the ambient light conditions. The α-Fe_2O_3 NR arrays annealed at 350 °C exhibit an enhanced bactericidal performance in inactivating *E. coli* O157:H7, when compared to α-Fe_2O_3 film. Mathematical models are used to correlate the observed photocatalytic activities.

INDEX WORDS: metal oxide, semiconductor bandgap, band edges, electronic structure, photocatalyst, oblique angle deposition, glancing angle deposition, dynamic shadowing growth, thin films, nanorods, charge transfer, charge recombination, water splitting, solar conversion efficiency, IPCE, dye degradation, bactericidal

METAL OXIDE PHOTOCATALYTIC NANOSTRUCTURES FABRICATED BY DYNAMIC SHADOWING GROWTH

by

PRADIP BASNET

M.S., University of Massachusetts, Dartmouth, 2010

A Dissertation Submitted to the Graduate Faculty of the University of Georgia in Partial
Fulfillment of the Requirements for the Degree

DOCTOR OF PHILOSOPHY

ATHENS, GEORGIA

2015

METAL OXIDE PHOTOCATALYTIC NANOSTRUCTURES FABRICATED BY DYNAMIC SHADOWING GROWTH

by

PRADIP BASNET

Major Professor:	Yiping Zhao
Committee:	Jason Locklin Tho Nguyen Zhengwei Pan Susanne Ullrich

Electronic Version Approved:

Julie Coffield
Interim Dean of the Graduate School
The University of Georgia
May 2015

DEDICATION

This dissertation is dedicated to my family, lovely wife Prashikshya, and lovely twin sons Pratul and Prabal, all of them. None of this work would be possible without their love, sacrifice, patience and constant encouragement during the most difficult phase of my Ph.D.

ACKNOWLEDGEMENTS

First, I would like to thank my advisor Dr. Yiping Zhao for the help and support he provided me since I joined his research group at the University of Georgia. This work would not be possible without his ideas, constant guidance, and encouragement. Dr. Zhao has taught me enough to handle the research problems as well as writing skills. He has been an invaluable mentor, a great friend, and an inspirational person.

I would also like to extend my sincere gratitude to my committee members, Dr. T. Nguyen, Dr. J. Locklin, Dr. Z. Pan, and Dr. S. Ullrich for their professional suggestions and review of my dissertation. They have provided me many helpful suggestions throughout my dissertation. It’s my honor to have these Professors in my advisory committee. I am grateful to Dr. Uwe Happek for his moral and financial support, without which the completion of this dissertation would not be possible. I owe a special thanks to one of our senior group members, the now Dr. Larsen (George), who is one of my irreplaceable friends, who taught me the research techniques that are essential to the completion of this dissertation.

I am certainly deeply appreciative and thankful to many friends and colleagues that I have come to know in the pursuit of my Ph.D. In particular, I would like to acknowledge many of my fellow lab members and outside, both in past and the present, for their help over the years: Dr. K. Yao, Dr. W. Smith, Dr. J. Abell, Dr. E. White, Dr. Manjare (Manoj), Mr. Weijie Huang, Dr. Y-j Chuang, Mr. Rui Cheng, Mr. J. Noah Ashby, Mr. Taku Cowger, Mr. Steven Larson, Mr. Layne Bradley, Dr. X. Wu, Ms. Whitney, Dr. X. B. Li, Dr. P. Dong for their scientific insights and kind support in experiments.

I cannot express the depth of my gratitude in words to my parents and parents-in-law, for all the unconditional love and their affection and I cannot think of any way right now to return their great love and sacrifice for me. I am thankful for everything that they have given me.

Finally, I offer my regards and blessings to the Physics department, faculty and staffs for providing me with the help and guidance throughout my time, as a graduate student, at the University of Georgia.

TABLE OF CONTENTS

Page

CHAPTER

APPENDIX

LIST OF TABLES

Page

LIST OF FIGURES

CHAPTER 1

INTRODUCTION

1.1 Motivation and Challenges

Recently, the use of semiconductor photocatalysts for renewable energy and environmental remediation applications has drawn significant attention.[5-12] These applications involve a combination of photochemistry and catalysis. The term "photocatalysis" herein implies that both light and a catalyst are essential to enhance the rates of thermodynamically favored, but kinetically sluggish, photophysical and photochemical transformations. The fundamental and applied research on this subject has been performed for more than three decades. Nowadays, the main goal of this research is to develop a stable, efficient, non-toxic, and visible light active photocatalyst (VLAP).[13-15] Since the work of Honda and Fujishima in 1972, TiO_2 has always been the most popular material in this field due to its unique and outstanding physiochemical properties such as high photocatalytic performance, stability against photocorrosion, and non-toxicity.[14-19] Practical application of TiO_2 for harvesting the solar energy is limited due to its high bandgap value, $E_g \geq 3.2$ eV as shown in Fig.1.1.[1, 2, 8, 14, 20] In lieu of this, the most commonly used TiO_2 photocatalyst cannot function efficiently when irradiated under sunlight, as the solar spectrum is only 5% UV, while a large portion is visible and NIR (43% and 52% respectively). As a result, the theoretically predicted solar-to-hydrogen efficiency (STH) of both Anatase (A) and Rutile (R) -TiO_2 is less than 3%. In addition to this limitation, the use of UV light that is required to activate the TiO_2 is potentially quite hazardous particularly for indoor applications. It is advantageous to develop material which absorbs visible (or possibly NIR) radiation so that an even higher STH efficiency under solar illumination can be achieved. As predicted by J. Li and N. Wu and shown in Fig. 1.1.[20] This efficiency increases to 4.8%, 12.9%, and 26.5% for WO_3, Fe_2O_3, and, CuO respectively, as their bandgaps decrease. Subsequently, if one could develop a suitable photocatalyst whereby E_g ~1.5 eV, one could expect an STH efficiency about 38% (see Fig. 1.1). A Similar trend is observed for the photocurrent density (mA/cm^2) generated at 1 sun (AM 1.5G): CuO exhibits the highest value (= 21.5 mA/cm^2) with the lowest bandgap, E_g ~ 1.7 eV, and A-TiO_2 exhibits the lowest value (= 1.1 mA/cm^2) with E_g ~ 3.2 eV.

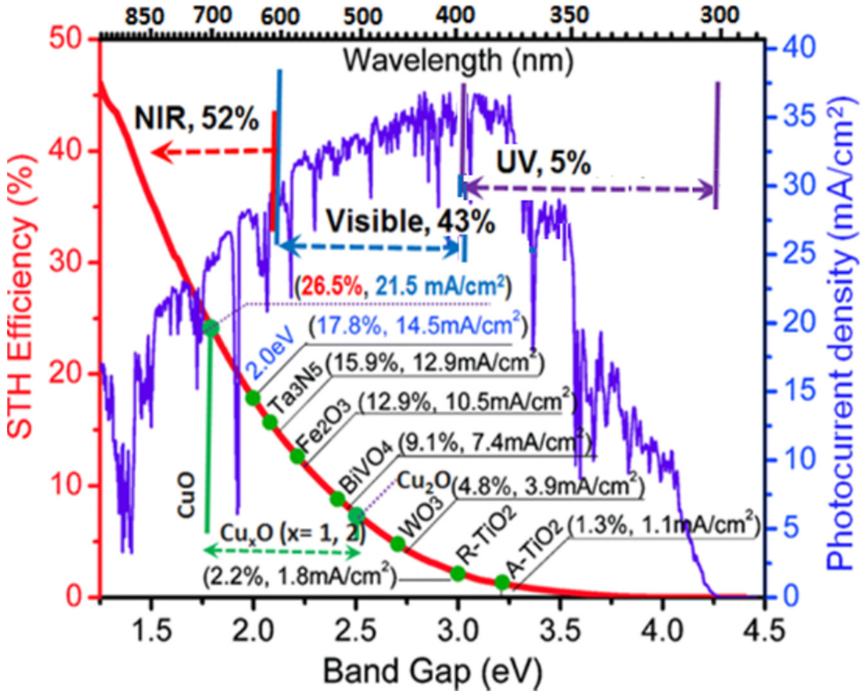

Fig. 1.1 Spectrum of solar radiation versus theoretically predicted solar-to-hydrogen (STH) efficiency and the photocurrent density for some of the UV and visible light active photocatalysts under AM 1.5G (1000 W/m^2; 1 sum equivalent).

The greatest challenge for a high efficient photocatalyst is the requirement of lower bandgap materials, with $E_g \leq 3.0$ eV. To tackle this challenge, researchers are either attempting to either lower the E_g of traditional photocatalysts, such as TiO_2, ZnO, WO_3 etc., or to find new class of materials with lower E_g. Typically, doping, or co-doping of the higher bandgap materials with non-metals (such as carbon, sulfur, fluorine, nitrogen etc.),[21-26] transition metals (such as silver, gold, platinum etc.),[14, 15] and making heterojunctions[14, 16, 21] are the common approaches to reduce E_g values of high E_g MO. Some of the lower bandgap materials that work under the visible light irradiation include CuO, Cu_2O, α-Fe_2O_3, CoO, Bi_2O_3, $BiVO_4$, CdS etc.[27-31] The photocatalytic performances of these materials can expected to be different based on their optical, structural, electronic properties as mentioned above. In addition, the nature of applications can be a factor to optimize the overall photocatalytic performance. Thus, in this dissertation we study some of the VLAP materials for dye degradation, solar energy conversion, and bactericidal applications to find their optimal efficiencies. This work is mainly based on the three major challenges in the heterogeneous photocatalysis, and that can be categorized as:

1. Visible light active materials: requires $E_g \leq 3.0$ eV.
2. Material types: requires high natural abundance, stability, non-toxicity, etc.
3. Methods of preparation: requires a reliable and applicable for large-scale production.

1.2 The Fundamental of Photocatalysts

1.2.1 Electronic Band Structure

The photocatalytic activity of a semiconductor is strongly affected by the amount of light absorption by the material, which is mainly determined by its E_g value. In this section, we introduce the electronic band structure of semiconductors and how it determines the materials' optical and electronic properties. Let's consider a single hydrogen atom, according to quantum mechanics, its outer electron has discrete energy levels. The electronic energy states are characterized by its principal quantum numbers. If two atoms are brought close enough to each other, to form a H_2 molecule, then the electrons surrounding each atom start to interfere, and their wave functions start to overlap. As a result, each energy level of the single atom will split into two due to the Pauli Exclusion Principal, *i.e.*, bonding and antibonding states. If many atoms are brought together, like those in a solid, the subsequent splitting of energies will create closely spaced energy levels. When the number of atoms, *N,* becomes large, the energy levels are so closely spaced and it is possible to consider them as continuum energy states; and the continuum energy levels are called "electronic energy band".[32, 33] This process is illustrated in Fig. 1.2. Figure 1.2 shows the change of the electronic structure of a semiconductor as *N* increases from unity to clusters of more than 2000 units.[1] Thus, the electronic energy structure within a semiconductor consists of three distinguish regimes, conduction band (CB), valance band (VB), and the forbidden band. The forbidden band represents a region in which, for an ideal, intrinsic semiconductor, energy states do not exist. Energy states only exists above and below this region. A brief derivation is shown below.

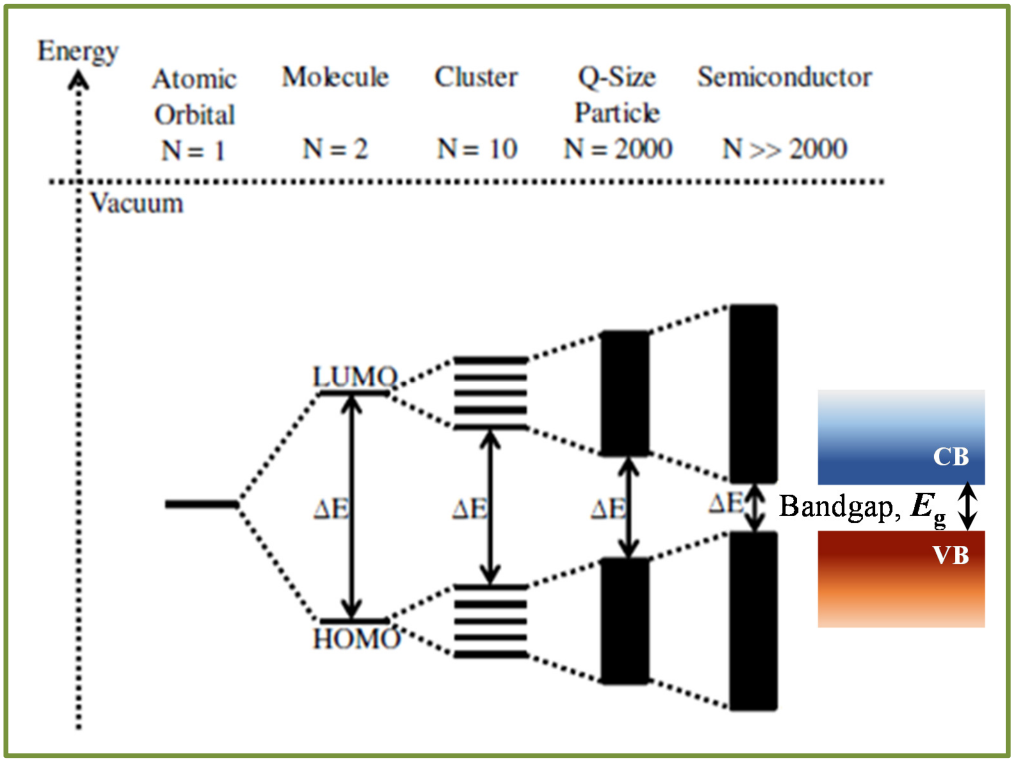

Fig. 1.2 Schematic diagram showing energy level splitting and forming of the energy bands as the number of atoms (N of monomeric units) increases from unity to clusters of more than 2000 units. Figure (left part) after the reference [1]

A semiconductor's energy band structure can be calculated using the Schrödinger's equation, with a periodic potential due to the crystal lattice,[32]

$$i\hbar \frac{\partial \psi(\mathbf{r},\, t)}{\partial t} = \left[-\frac{\hbar^2}{2m_0} \nabla^2 + V(\mathbf{r}) \right] \psi(\mathbf{r}, t)\,, \tag{1.1}$$

where $\hbar = h/2\pi$, h is the Plank's constant, $\psi(\mathbf{r},t)$ is the electron wave function, m_0 is the mass of a free electron and $V(\mathbf{r})$ is the periodic potential, $V(\mathbf{r}) = V(\mathbf{r} + \mathbf{R})$, where $\mathbf{R}$ is the translation vector of the crystal lattice. For a conservative system, $\psi(\mathbf{r},t)$ can be written as $\psi(\mathbf{r})\, e^{-iEt/\hbar}$, therefore

$$\left[\frac{\mathbf{P}^2}{2m_0}+V(\mathbf{r})\right]\psi(\mathbf{r})=E\psi(\mathbf{r}), \tag{1.2}$$

which is referred to as the time-independent Schrödinger equation. Here, $\mathbf{P}=-i\hbar\nabla$ is the momentum operator. Solution to Eqn. (1.2) is a Bloch function, defined as,

$$\psi_{n\mathbf{k}}(\mathbf{r})=e^{i\mathbf{k}.r}u_{n\mathbf{k}}(\mathbf{r}), \tag{1.3}$$

where *n*, *k*, and $u_{n\mathbf{k}}(\mathbf{r})$ are the band index, electron wave vector, and a function with the same periodicity as $V(\mathbf{r})$. By substituting Eqn. (1.3) into Eqn. (1.2), we can derive

$$\left[\frac{\mathbf{P}^2}{2m_0}+\frac{\hbar\mathbf{k}\cdot\mathbf{P}}{m_0}+\frac{\hbar^2k^2}{2m_0}+V\right]u_{n\mathbf{k}}=E_{n\mathbf{k}}u_{n\mathbf{k}}. \tag{1.4}$$

At zone center, i.e., K = (0, 0, 0), Eqn. (1.4) reduces to,

$$\left[\frac{\mathbf{P}^2}{2m_0}+V\right]u_{n0}=E_{n0}u_{n0}, \tag{1.5}$$

where E_{n0} and u_{n0} are the zone center band energies and Bloch functions, respectively. The solution to Eqn. (1.4) for $K\neq(0,0,0)$ can be found using degenerate and non-degenerate perturbation theory.[32] The formalism is referred to as the **k.p** method, where the $\hbar\mathbf{k}\cdot\mathbf{P}/m_0$ and $\hbar^2\mathbf{k}^2/2m_0$ terms are treated as perturbations to zone center solutions. The optical properties, and electronic properties of semiconductors therefore can be modeled as parabolic band structure of a direct bandgap as photons primarily interact at the zone center as shown in Fig. 1.3(a). The transition probability from one energy state $|i\rangle$ to a final state $|j\rangle$ is governed by the Fermi's Golden rule,

$$W_{i\to f} = \frac{2\pi}{\hbar}\left|\left\langle f\left|H^{'}\right|i\right\rangle\right|^{2} g(h\upsilon), \qquad (1.6)$$

where $\left\langle f\left|H^{'}\right|i\right\rangle$ is the matrix element for the perturbation between the final state $\left|j\right\rangle$ and initial state $\left|i\right\rangle$ and $g(hv)$ is the density of electron states in the valance and conduction bands (see Fig. 1.3). Eqn. (1.6) is a useful way to calculate the transition rate of electron from one energy state to another due to a perturbation. For photoexcitation, the perturbation is the incident light with frequency v. The electron in the VB can only be excited to CB by a photon with energy hv larger or equivalent to bandgap energy E_g. This process occurs under the restrictions of energy and momentum conservation. Photons travel at the speed of light, so they have almost negligible momentum relative to electrons' momentum in the crystal. This makes the electronic transition perfectly "vertical" in E-k diagram (Fig. 1.3(a)), *i.e.,* the initial and final states have the same k vector as it occurs in the direct bandgap materials (and exceptions are phonon assisted transitions in indirect transition as shown in Fig. 1.3(b)). The optical absorbance depends on the nature of the electron transition, *i.e.*, whether the transition is a direct or indirect transition. In a direct bandgap material, light penetration depth is lower at the bandgap energy since all light is absorbed close to the surface. As a result a film with relatively small thickness is enough to absorb more photons. In an indirect bandgap material, VB maximum and the CB minimum lie at different k-vector locations (see Fig. 1.3(b)) such that a light absorption must be assisted by a third (quasi) particle called phonon (lattice vibration) in order to conserve the E and k.[34, 35] In this case, the absorption coefficient is less at the bandgap energy (or close to it), so relatively thicker films are required to absorb more photons.

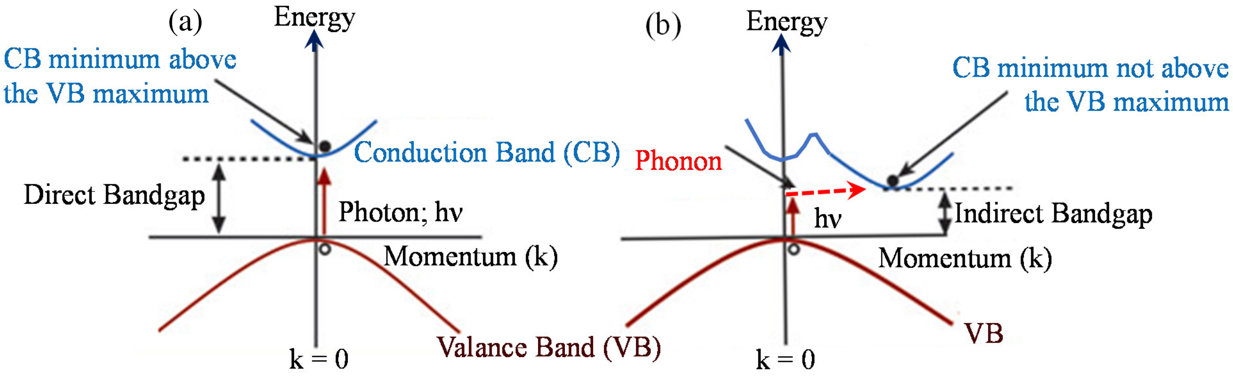

Fig.1.3 Illustration of an electron excitation in a (a) direct and (b) indirect bandgap semiconductor. Upward arrow represents the photon absorption. Light absorption in (b) is executed by a photon and a phonon in combination to conserve momentum and energy.

Based on the bandgap E_g of a solid state material, materials can be categorized into metal, semiconductor, and insulator, as shown in Fig. 1.4.[34] The E_g values of semiconductors are in the range of about 1 eV to 4 eV, while metal has no bandgap, and insulator are typically characterized $E_g \geq 4$ eV. The VB is also referred to as the highest occupied molecular orbitals (HOMO), which are the highest orbitals that an electron can be naturally found in a material; while the CB is referred to as the lowest unoccupied molecular orbital (LUMO), because it is the next stable electron orbit that is not already occupied by the electron.

The Fermi energy level is defined as the energy level at which the probability of electron occupation at 0 K is equal to 50% (all bands are either full or empty).[34] The location of E_F relative to the allowed energy bands is crucial in determining the properties of semiconductors based on their types (intrinsic, n-type, and p-type as shown in Fig. 1.4). The free carriers in n-type semiconductor is dominated by electrons in the CB; while the holes in VB are dominant charge carriers in the p-type semiconductors. Note that intrinsic semiconductors are poor electrical conductors at low temperatures. They only conduct when carriers are thermally excited across the bandgap (by energy, $E = K_BT$, where K_B is the Boltzmann's constant and T is the absolute temperature). At room temperature this energy can be approximated to be 25 meV.

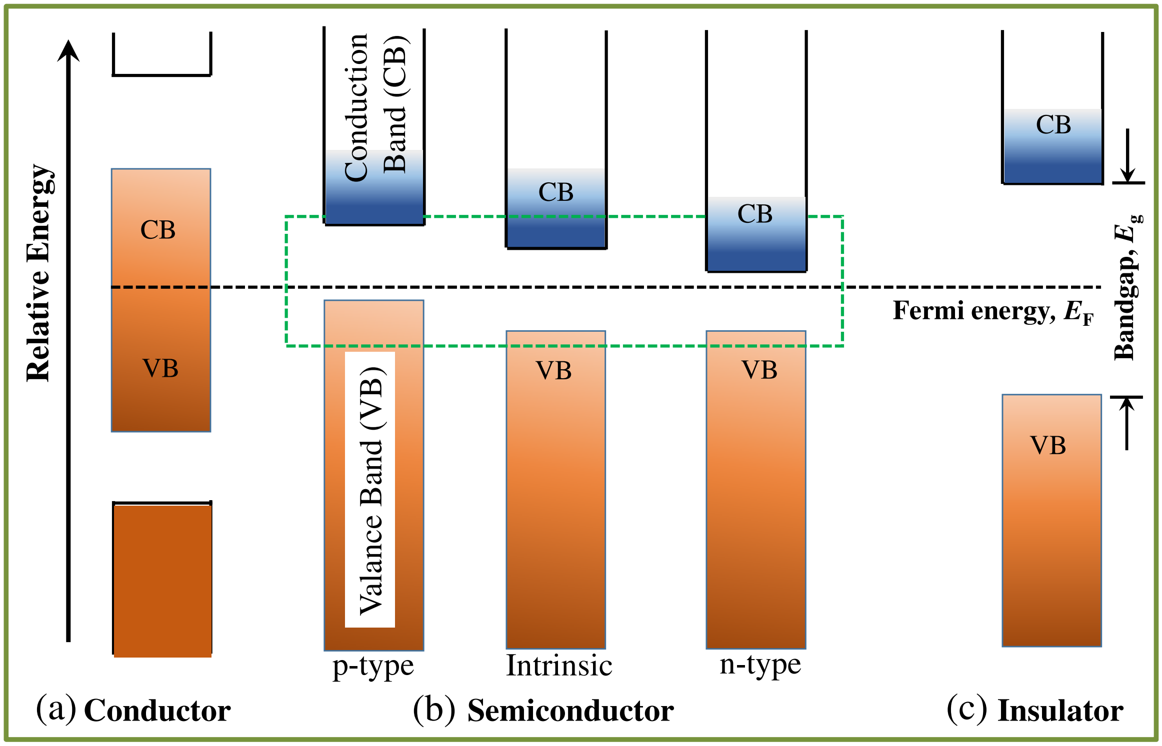

Fig.1.4 Energy bandgaps and the electronic band structure in materials: Fermi level position for (a) metal or conductor, (b) semiconductors (intrinsic, p-type, and n-type), and (c) insulator. Note that the Fermi level E_F is approximately in the middle of bandgap for intrinsic semiconductor; for p-type semiconductor, E_F is close to VB (and the CB is far above); for n-type E_F is close to CB (and the VB is far below), as represented by dotted green box.

Comparing the E_g of a semiconductor and the thermal energy at room temperature (25 meV), the electron transition from VB to CB is most likely impossible to occur. When the temperature is above the absolute zero, at thermal equilibrium, the electrons do not simply fill the lowest energy states first. In this case, we need to consider the Fermi-Dirac statistics which gives the probability distribution of an electron of energy E at temperature T,[36]

$$f_e(E) = \frac{1}{1+\exp\left(\frac{E-E_F}{K_B T}\right)}. \tag{1.7}$$

The Fermi-Dirac distribution $fe(E)$ is equal to unity, for $E < E_F$ at $T = 0$ K while $fe(E) = 0$ for $E > E_F$. Electrons will be thermally excited around E_F, and $fe(E) < 1$ near E_F ($E < E_F$) while $fe(E) > 0$ at $E > E_F$. At $E = E_F$, $fe(E) = 1/2$ regardless of temperature. A typical plot for three different temperatures are illustrated in Fig. 1.5.

Note that the $fe(E)$ can be replaced by $f_h(E)$ (=1- $fe(E)$) representing the density of holes in the VB, and can be written as,

$$f_h(E) = \frac{1}{1+\exp\left(\frac{E_F-E}{K_B T}\right)}, \tag{1.8}$$

which gives the probability of the state at E not to be occupied by an electron (and thus to be occupied by a hole).[36] In fact, more general formulation of Fermi-Dirac statistics involves a chemical potential μ' instead of E_F. This chemical potential depends on the temperature and the applied potential. But in most cases of semiconductors, the difference between μ' and E_F is very small at the temperature we usually considered.

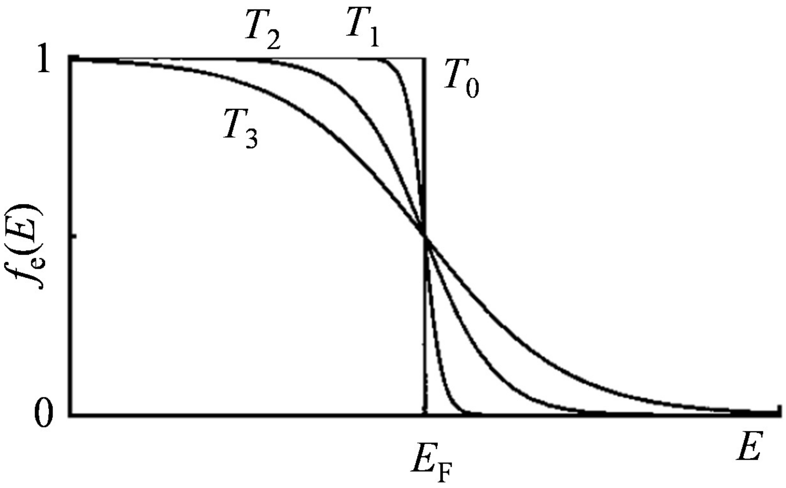

Fig. 1.5 Fermi-Dirac distribution function at different temperatures: $T_3 > T_2 > T_1$ *(and* $T_0 = 0$ *K). At the absolute zero temperature (*T_0*), the probability of an electron to have an energy below the Fermi energy EF is equal to 1, while the probability to have higher energy is zero.*

1.2.2 Elementary Steps in Heterogeneous Photocatalytic Systems

Photocatalytic systems are classified into homogeneous and heterogeneous systems depending on the material states of photocatalysts and the reactants (or the chemical environments). In a homogeneous system, both the reactants and the photocatalysts are in the same state such as they are all gas state or liquid state, while in a heterogeneous system, the photocatalysts are usually in solid state and the reactants are either in liquid state or in gas state. Since we are using the solid metal oxide (MO) semiconductor photocatalysts for the photocatalytic dye degradation (PDD), photocatalytic water splitting (PWS), and bactericidal activity, the photocatalytic reactions we are dealing with are heterogeneous.

For any heterogeneous photocatalyst, to carry out the photocatalytic reaction, it involves at least two process, the processes intrinsic to the photocatalyst, *i.e.*, the generation and transportation of photogenerated charge carriers, and the detailed photoreaction process between the photocatalyst and its environment. Inside the photocatalytic material or on its surface, the heterogeneous photocatalytic reactions mainly involve four key processes as shown in Fig. 1.6,[37]: i) the absorption of photons with energy equal or higher than the photocatalyst's bandgap, ii) the generation of electron-hole pairs (e^-- h^+) where e^- and h^+ represent the photo-generated electrons in CB and holes in VB, iii) the diffusion or transport of the photogenerated charge carriers on the surface or in the bulk, and iv) the recombination, collection, and separation of photogenerated charges on surface or in the bulk (Paths (A) & (B) in Fig. 1.6). The separated charge carriers are responsible for photocatalytic reactions (reduction by electrons as shown in Path (C) and oxidation by holes as shown in Path (D)). For all photocatalytic reactions, above four steps are essential. Below we will discuss them in detail.

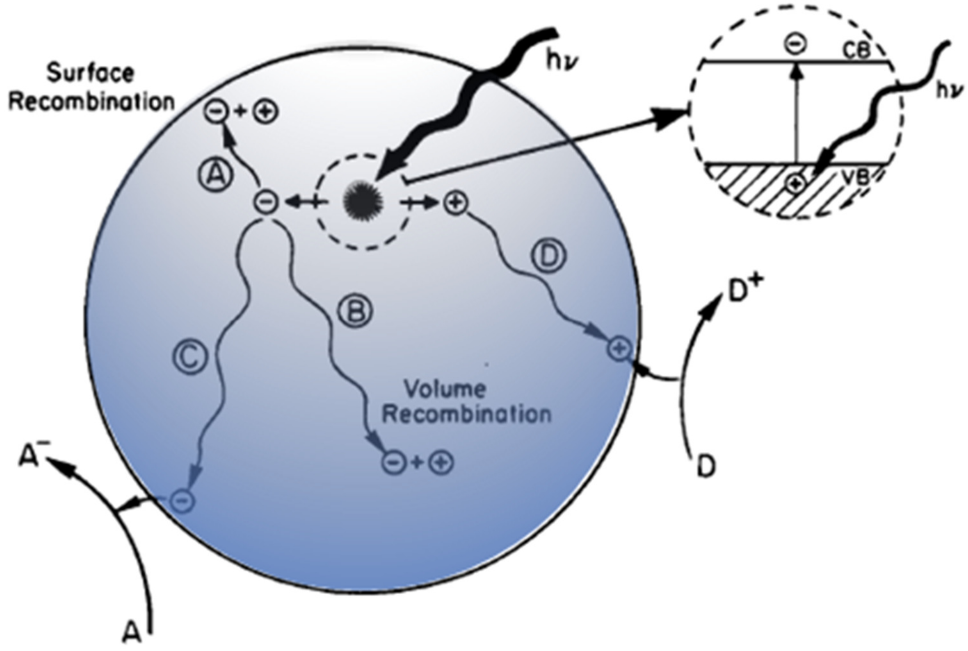

Fig. 1.6 Schematic diagram showing the typical process occurring during the photocatalysis, i.e. including the photoexcitation in a semiconductor photocatalyst followed by redox reactions and deexcitation events.

1.2.2.1 Light Absorption and Charge Carrier Generation

The amount of light absorption by a thin layer of photocatalyts is crucial for charge carrier generation and the absorption intensity may depend on various factors such as crystal structures, bandgap energy, presence of defects and foreign elements inside the photocatalyst.[2, 32] The light transmitted through a thin layer (thickness x) of photocatalysts follows the Beer's law,

$$I_t = I_0 e^{-\alpha x} \tag{1.9}$$

where I_0 is the incident light intensity, I_t is the transmitted intensity (see Fig. 1.7), and α is the absorption coefficient (cm^{-1}). Alternatively, Eqn. (1.9) can be rewritten as,

$$\alpha(\lambda) = \frac{1}{x}\ln\left(\frac{I_0}{I}\right) = \frac{1}{x}\ln\left(\frac{1}{T(\lambda)}\right). \tag{1.10}$$

where $T(\lambda)$ is the transmittance of the photocatalyst. If one assumes that all loss of light is due to absorbance, the total absorbance $A(\lambda)$ can be estimated as,

$$A(\lambda) = (I_0 - I)/I_0 = (1 - e^{-\alpha x}). \tag{1.11}$$

It is worthy to note that above equations are only valid for the photocatalyst with negligible reflectance and scattering. In real cases, one needs to include the effect of reflectance $R(\lambda)$ (and scattering but usually we assume scattering is much smaller than reflectance) so that a better estimation of absorbance will be achieved. As shown in Fig. 1.7, by considering the $R(\lambda)$, Eqns. (1.11) and (1.12) will be changed to,

$$\alpha(\lambda) = \frac{1}{x}\ln\left(\frac{1-R(\lambda)}{T(\lambda)}\right), \tag{1.12}$$

and,

$$A(\lambda) = 1 - T(\lambda) - R(\lambda). \tag{1.13}$$

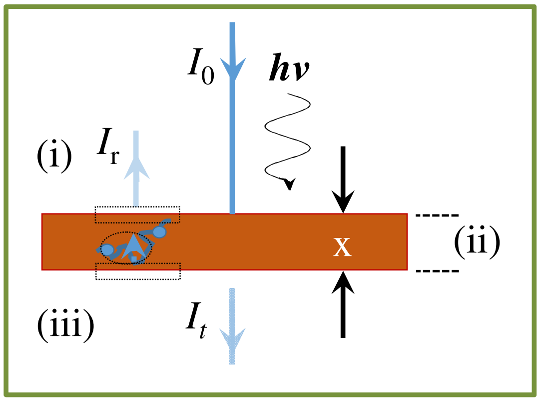

Fig. 1.7 Schematic diagram showing the typical process occurring when incident light beam (of intensity I_0) hits a thin film semiconductor (of thickness x): a part of initial beam will be reflected (shown in region (i)), a part of it will be transmitted (shown in region (iii)) and the rest will be either absorbed or scattered (shown in region (iii); and scattering is neglected in our calculation).

The charge generation rate, G for photons with energy at or above its bandgap energy can be estimated as,

$$G(\lambda) = \eta(\lambda) \cdot A(\lambda) \cdot N_0(\lambda) \tag{1.14}$$

where η (≤ 1) is the quantum efficiency of e^-- h^+ pair generation, $N_0(\lambda)$ is the photon flux at surface of the photocatalyst. The quantity η can be measured experimentally while N_0 can be obtained from incident light intensity,

$$N_0 = I_0 \cdot S_0 \left(\frac{\lambda}{hc} \right), \tag{1.15}$$

where I_0 is the intensity of incident light, S_0 is the illumination area. Thus, Eqn. (1.15) can be rewritten as,

$$G(\lambda) = \varphi(\lambda)[(1 - e^{-\alpha x}) - R(\lambda)], \tag{1.16}$$

where $\varphi(\lambda)$ is defined to be $[\eta(\lambda) \cdot I_0 \cdot S_0 \cdot \lambda]/hc$, which is a constant at a given wavelength. Eqn. (1.16) reveals an exponential decrease in carrier generation rate as a function of the thickness of the material (for a given $\varphi(\lambda)$ and $R(\lambda)$). It means that more e^- - h^+ pairs are created closer to the surface of the photocatalyst than in the bulk. This information can be used to design the semiconductor photocatalysts of appropriate thickness, which not only minimize cost but also improve the photocatalytic efficiency.

1.2.2.2 Electron-Hole Pair Recombination

Unlike the process of charge carrier generation, the recombination process is characterized by the annihilation of e^-- h^+ pairs. This process is an undesired process in photocatalysis as it reduce the photocatalytic performance. The recombination of e^-- h^+ pairs can occur anywhere on the surface or in bulk of a photocatalyst as shown in Fig. 1.6. Even though there is no such a clear explanation about the "recombination" in the literate, various factors have been introduced. Some of the materials related factors are impurities, defects, degree of crystallinity, surfaces, etc.[38, 39] And other factors, related to experimental constraints, are also reported, such as reaction temperature, concentration/ionic strength of the reactant solution, intensity and wavelength of the light source, and so on. Overall, recombination process in photocatalyts can be categorized into radiative and non-radiative as illustrated in Fig. 1.8(a) - (c).[40]

A radiative recombination shown in Fig. 1.8(a) is characterized by emission of a photon when a CB electron combining with a VB hole. It can be described in terms of carrier concentrations in their respective bands. The recombination rate is proportional to the electron and hole occupation probability.[32, 40] A nonradiative recombination process, does not generate a photon emission as shown in Fig. 1.8(b) and (c)), and in general, is predominant within the bulk structure of a photocatalyst forming a band-to-band recombination. These processes can be categorized into Auger recombination and recombination at defect or surface states. In Auger processes, an electron or hole transfers its momentum and energy to a third electron or hole as shown in Fig. 1.8(b). And the Auger recombination rate is determined by the types of charge carriers involved.[40]

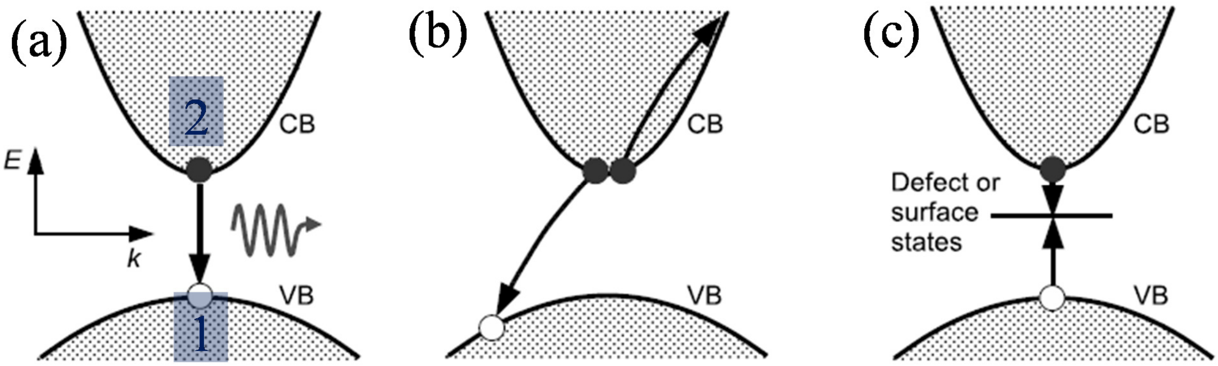

Fig.1.8 Electron-hole pair recombination mechanisms in semiconductors: (a) radiative recombination, (b) auger recombination (shown only for electrons; similar process possible for holes), (c) recombination at defect or surface states.

Recombination at defect or surface is another common process and it can be described by Shockley-Read-Hall (SRH) recombination (also called a recombination center), which is an allowed energy state within the forbidden bandgap as shown in Fig. 1.9.[35] In this route, the trap can capture both electrons and holes with almost equal probability. Process I shows that an electron hope down trap and ultimately destroy by a hole, i.e. being captured. Similarly, other Processes II-IV lead to electron capture and emission.[35]

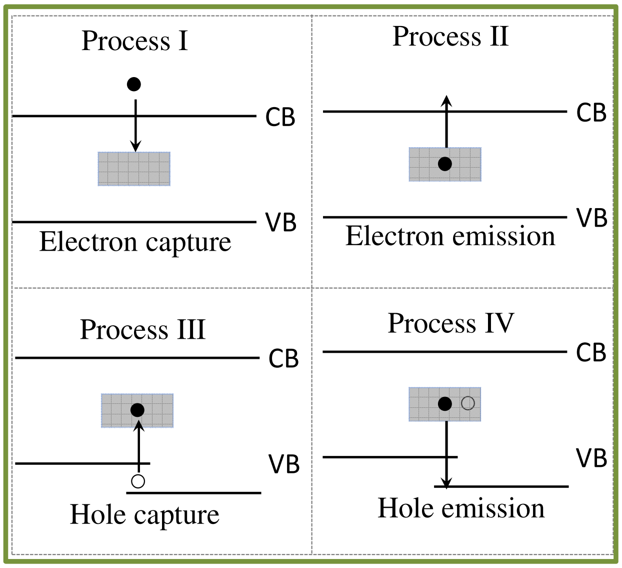

Fig.1.9 Four basic trapping and emission process for the case of acceptor-type trap.

1.2.2.3 Separation and Transportation of Charge Carriers

The photocatalytic performance of a photocatalyst is determined by the photocarrier's life time and their transport properties. Based on the principle of quantum mechanics, the absorption process of light with energy $hv \geq E_g$ pumps the electrons from VB into CB, leaving holes in the VB. This process is called the "charge separation". When the e^-- h^+ pairs are generated by light absorption, they are typically separated for a finite and pre-determined amount of time that is intrinsic to the material. The longer life time of the charge carriers is favorable for better photocatalytic activity. The life time τ_n of the photocarrier is determined by the electron and hole densities of the CB and VB, and the recombination process. The charge generation rate can be expressed as,

$$\frac{dn}{dt} = G - R_n + G_n, \tag{1.17}$$

where G_n is the thermally excitation rate of free carrier, R_n is the recombination rate. R_n is a linear function of the carrier density n and concentration of the defect states N, and can be written as,

$$R_n = C_n \cdot N \cdot n \,. \tag{1.18}$$

The proportionality constant C_n is called electron capture rate. The photoinduced electron concentration in the CB, after removing the light source and ignoring the thermal generation, can be written as,

$$\frac{dn}{dt} = -R_n = -C_n \cdot N \cdot n \,. \tag{1.19}$$

Thus,

$$n(t) = n_0\, e^{-C_n \cdot N \cdot t} = n_0\, e^{-t/\tau_n} \,, \tag{1.20}$$

where the electron life time $\tau_n = 1/(N \cdot C_n)$. Note that the similar expression can be used to represent the hole capture rate and its life time. Therefore, under an equilibrium photogeneration process, $dn/dt = dp/dt = 0$, we can estimate the effective generation rate G_{eff} as,

$$G_{eff} \equiv G_n - R_n = G_p - R_p \,. \tag{1.21}$$

It can be shown that the Eqn. (1.21) gives,

$$R_{eff} = \frac{C_n C_p N (n \cdot p - n_i^2)}{C_n (n + n_1) + C_p (p + p_1)} \,, \tag{1.22}$$

where n, p, N, C_n have their usual meaning and C_p is the hole capture rate. n_1 and p_1 are the equilibrium concentrations of free electrons and holes, which satisfies the relation $n_i^2 = n_1\, p_1$ for intrinsic carrier concentration when the Fermi energy level coincided with the energy level of traps. For an undoped semiconductor, *i.e.* $n = p >> n_1.\, p_1$, thus,

$$R_{eff} = n \cdot \frac{C_n C_p N}{C_n + C_p} = \frac{n}{\tau_n + \tau_p}. \quad (1.23)$$

This equation makes a perfect sense based on the fact that at high charge densities the recombination rate involves both the life time of electrons and holes. By rearrange Eqn. (1.23), the total life time of the charge carrier can be written as,

$$\frac{1}{\tau} = \frac{1}{\tau_{nonrad}} + \frac{1}{\tau_{rad}}, \quad (1.24)$$

where τ_{nonrad} and τ_{rad} are the lifetimes due to non-radiative and radiative recombination. In general, the nonradiative recombination processes are much faster than the radiative ones, they will dominate the recombination statistics if either the excitation is very high or if the number of defects in the material is appreciable. However, from the experimental point of view, it is very difficult to differentiate the radiative or nonradiative recombination times as described by Eqn. (1.24) because they leave no trace of evidence but disappear very rapidly (see Fig. 1.10). Some of the literatures have reported experimental techniques to observe dynamics of charge carriers on semiconductors.[41, 42] To be quantitative, the life time of the charge carriers in the excited state is on the order of nanoseconds in semiconductors in contrast to femtoseconds in metals.[14, 37, 41]

Fig. 1.10 shows a comparison of time scale for charge generation, recombination/ relaxation and for surface reactions.[2] The time scales shown in the figure may vary significantly by many orders of magnitudes depending on the processes. For example, at room temperature the "thermal diffusion" of carriers to the band edges occurs in less than 100 fs while the decay across the bandgap is extremely slow, by about nine orders of magnitude.[43] The charge separation life time could be further improved by a well-known process called "band bending".[1, 44, 45] This process involves both effect of material composition and the reaction environment in the case of heterogeneous photocatalysis. For example, the use of heterojunctions metal-semiconductor, and double or multilayers of semiconductor-semiconductor compositions have reported to exhibit the photocatalytic activity improved due to charge separation.[5, 44-46]

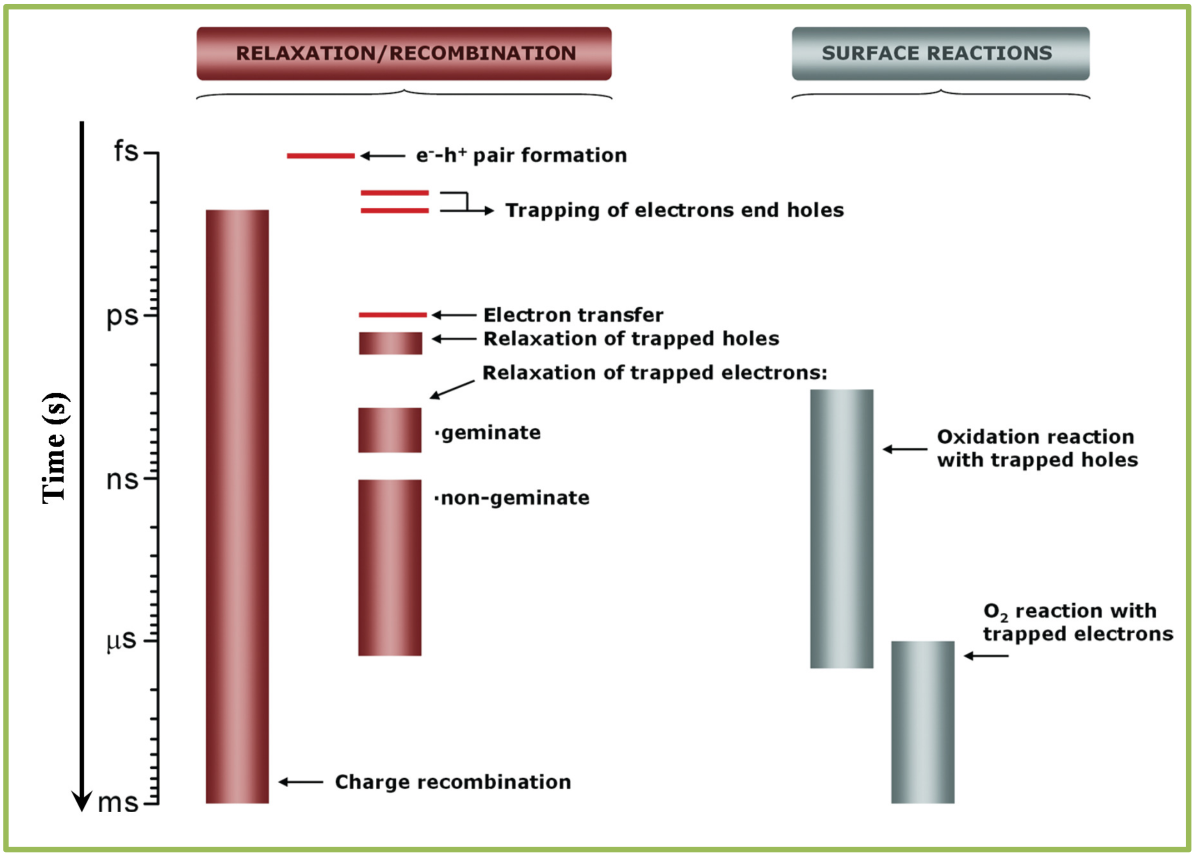

Fig. 1.10 Charge carrier generation, diffusion and transport processes in a semiconductor photocatalyst: time scales of "elemental steps" occurring in a heterogeneous photocatalytic process. Figure from Ref. [2].

Fig. 1.11 shows an example of enhanced life time of photogenerated charge carriers:[5] in the CB, the photogenerated electrons of Cu_2O transfer towards the ZnO and then towards the TiO_2 while the holes transport in the VB in the opposite direction. Thus more electrons are accumulated in CB of TiO_2 while more holes are in VB of Cu_2O. Such a process spatially separates *e*⁻ and *h*⁺, and extend their lifetime. This kind of series of charge transfer process from one material to the other would be helpful to design an efficient photocatalyst.

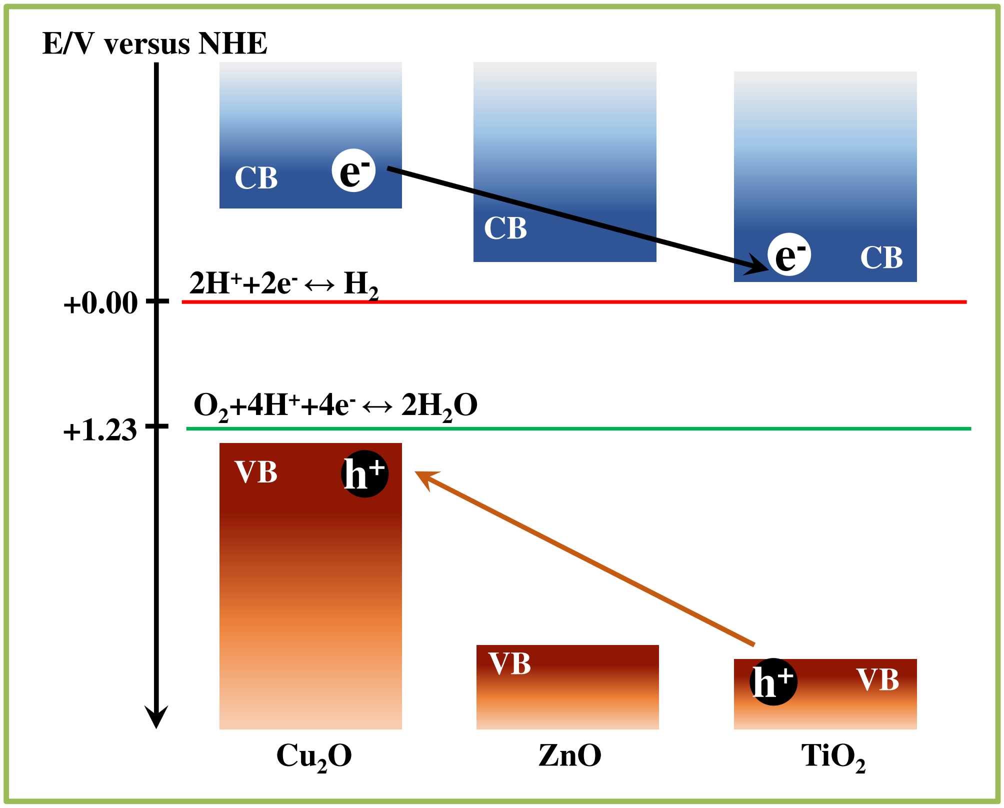

Fig. 1.11 Schematic diagram for composite photocatalyst, showing an enhanced charge transport process. Note that the directions of the charge transport represent towards the low energies, i.e. for both photogenerated holes and electrons in the VB and CB respectively.

Another important process that is affected by the carrier life time is the carrier transport process. The transport and life time of photogenerated charge carriers are interrelated. With other parameters the same, charge carriers having longer life time can transport longer distance in the crystal and *vice versa*. The characteristic transport time, τ_d , is also a very important parameter that can be used to analyze the photocatalytic activity. The τ_d can be approximated from random walk calculation, *i.e.*, based on the material's thickness.[2] As a rough approximation, electron diffusion coefficient D_n can be obtained from the Frohlich theory and τ_d can be expressed as,

$$\tau_d = \frac{L^2}{D_n}, \tag{1.25}$$

where L is the active film thickness. Similarly, the diffusion length, L_n, which is defined as an average distance that a carrier diffuses before disappearing, can be written as

$$L_n = \sqrt{D_n \tau_n} . \tag{1.26}$$

As mentioned above, Eqns. (1.25) and (1.26) require $L_n > L$ in order for a good amount of charges carriers to diffuse to the "surface" of the photocatalyst and to be involved in a catalytic reaction.

1.2.2.4 Photocatalytic Processes

Once the free charge carriers e^- and h^+ are generated, they both tend to diffuse to the surface of photocatalyst in order to participate the photocatalytic reaction. The photocatalytic processes may involve the entire or part of redox reactions depending on the photocatalyst's intrinsic properties and experimental parameters. Regardless of the material's intrinsic property, the reactants and the external bias potential are the two important parameters that determine the photocatalytic activities of a photocatalyst. In all PDD, bactericidal, and PWS processes, light absorption process and the charge carrier dynamics are similar while thermodynamics of reactions, properties of the reactants, and the role of adsorption/desorption, are different. In general, no external bias will be applied for both PDD and bactericidal activity while the PWS reactions will be conducted in certain range of external biased potential.

1.2.2.4.1 Photocatalytic Dye Degradation

The PDD process is thermodynamically a downhill reaction (- ΔG) such that a spontaneous reaction will occur by utilizing the light absorption, *i.e.*, providing $hv \geq E_g$. The redox reactions with the e^-- h^+ pair generated in the PDD can be summarized as,

Oxidation: $H_2O + h^+ \rightarrow OH^\bullet + H^+$ (1.27)a

$OH^-_{(ads)} + h^+ \rightarrow OH^\bullet_{(ads)}$, leading to $2OH^\bullet \rightarrow H_2O_2$ (1.27)b

Reduction: $O_{2(ads)} + e^- \rightarrow O_2^{\bullet -}$ (1.28)

where $OH^\bullet$ and $O_2^{\bullet -}$ are hydroxyl radicals and superoxide radical ions respectively. These radicals including the H_2O_2 are called reactive oxygen species (ROS). The PDD activity is strongly dependent on the amount of ROS generated. Eqn. (1.28) shows that the activated oxygen species may take part in the oxidation of the organic electron donor. On the other hand, photogenerated holes can oxidize the electron donor (also referred to as the "hole scavenger"), either *via* the formation of reactive species such as surface-bound $OH^\bullet$ radicals or through direct reaction with adsorbed organic molecules (see Fig. 1.12). Based on the fact that the photocatalytic reactions that occur on the surface of a photocatalyst, a well-known Langmuir-Hinshelwood kinetic equation can be introduced to explain the PDD activity. In particular, the kinetics of the PDD reaction is controlled by the adsorption of reactants (in this case, dye molecules). So, the general equation for the dye adsorption rate (onto the photocatalyst) can be written as,

$$r_{ads} = \frac{KC}{1+KC}, \tag{1.29}$$

where K is called the Langmuir adsorption coefficient for dye and C is the dye concentration (see Appendix A for full derivation).

The concentration profile of a dye in heterogeneous photocatalysis can be estimated by using a pseudo-first order reaction model. From the Beer's law (Absorbance coefficient $\alpha \propto C$), by measuring the optical absorbance of the dye during photocatalytic reaction, we have

$$\alpha(t) = \alpha(0)e^{-k_c t}, \tag{1.30}$$

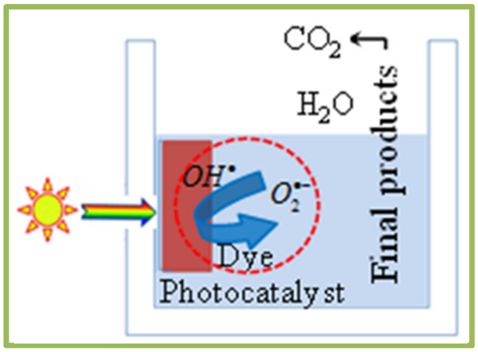

Fig. 1.12 Schematic diagram showing photocatalytic dye degradation reaction in a Cuvette where the photocatalyst is irradiated light through the window.

where $\alpha(0)$ is the initial absorbance of the dye at time $t = 0$ min and κ_c is the dye degradation rate constant. Eqn. (1.30) can be used to estimate the dye degradation rates κ_c, which can be used to characterize the photocatalytic activity. Another important factor that determines the κ_c is the color of the dye such that the amount of light absorption by the dye can enhance the charge separation by injecting the photoexcited charge carriers of the dye molecules into the photocatalyst, resulting in better performance (see Fig. 1.12). In PDD reaction, this process is called a dye sensitization. In this case, the overall photocatalytic activity will be determined by the direct semiconductor photoexcitation and indirect dye photosensitization.[47-49] The indirect photosensitization involves a two-step process: excitation of dye *via* visible light absorption and transfer/injection of excited electron(s) onto the CB of a photocatalyst (if the band alignment is matching well), and the possible reactions can be summarized as,

$$Dye_{(ads)} + h\nu \rightarrow Dye^{*}_{(ads)} \tag{1.31}$$

$$Dye^{*}_{(ads)} + MO \rightarrow Dye^{\bullet+}_{(ads)} + MO(e^{-}) \tag{1.32}$$

$$Dye^{*}_{(ads)} + O_2 \rightarrow Dye_{(ads)} + {}^{1}O_2 \tag{1.33}$$

$$Dye + MO(e^{-}) \rightarrow Dye^{\bullet-} \tag{1.34}$$

$$Dye + h^{+}_{VB} \rightarrow Dye^{\bullet+} \tag{1.35}$$

where $Dye^{*}_{(ads)}$ represents the dye in the excited state and MO(e^-) refers the MO with transferred electron. ${}^{1}O_2$ is singlet oxygen which is also detrimental for the organic pollutants including both the dye and bacteria.

1.2.2.4.2 Bactericidal

Bactericidal activity is also believed to be controlled by the amount of ROS generated during the photocatalytic reactions. Thus, bactericidal activity also requires the

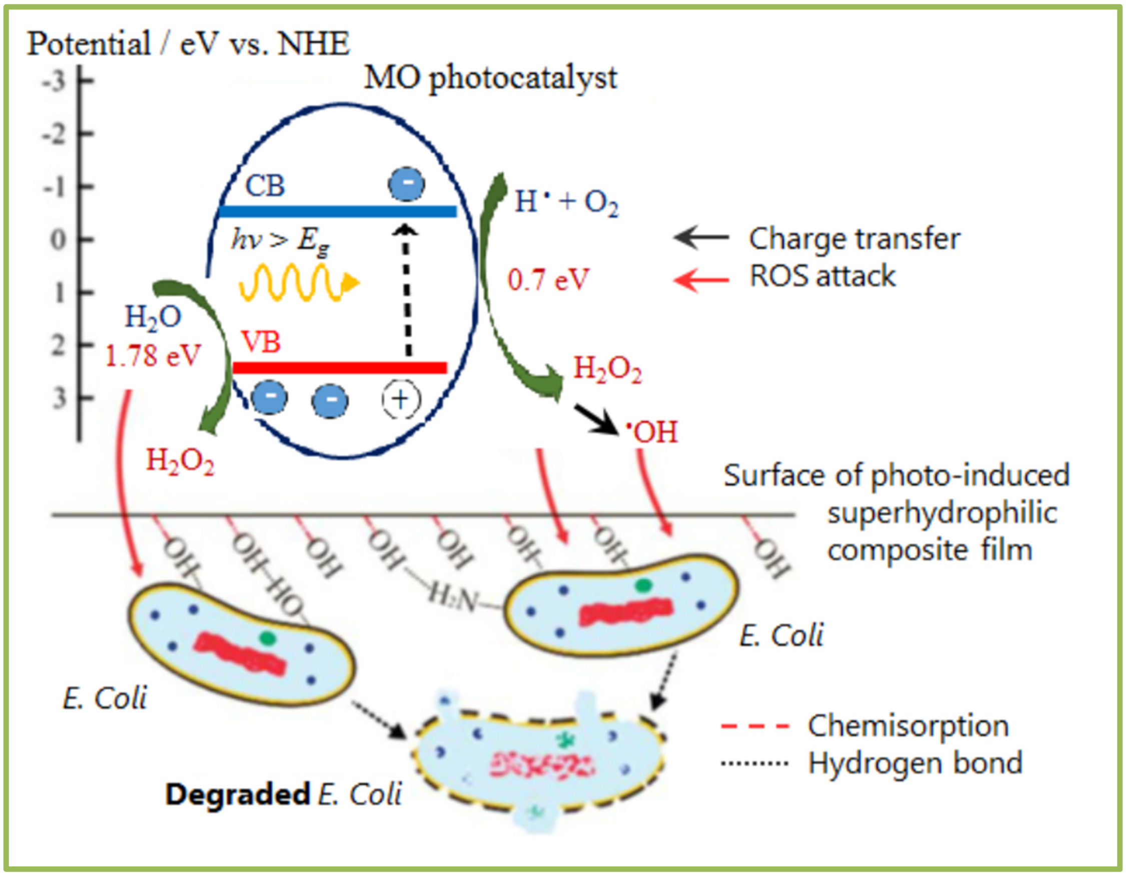

Fig. 1.13 Schematic diagram showing the overall bactericidal mechanism: generation and transfer process of photocarrier, after light absorption, creating ROS species and finally leading to the cell degradation. Figure from Ref.[3].

same redox reactions. Fig. 1.13 shows the bactericidal mechanism based on the photocarrier generation and production of ROS. From the figure, it is clear that the activity depends on various factors: material's bandgap, band edges of both the CB and VB, surface contact with the bacteria, and charge transfer. The effect of band edges is relatively more important in generating the ROS as it requires to have enough potentials for multiple charge transfer at the solid-liquid interface. In this viewpoint, all different species of ROS ($O_2^{\cdot -}$,

$^{\cdot}OH$, H_2O_2, and so on) can cause a photochemical oxidation of intracellular coenzyme A, which alters the respiratory activities leading to the cell damage.[50, 51] Representative SEM images in Fig. 1.14 show evidence that this lethal action is due to outer membrane and cell wall damage.[4]

By comparing the experimental setup and parameters for the PDD and bactericidal reactions, the reactants, including their physical sizes and the final products, can be regarded as the main difference. For instance, dye molecules are of less than a few nanometers in size but the bacteria are of about a few micrometer (see Fig. 1.14). This factor might affect the overall bactericidal activity especially when one uses the immobilized photocatalyst that cannot move towards to bacteria. These dissimilarities may create a problem in making a direct quantitative comparison between PDD and bactericidal activity.

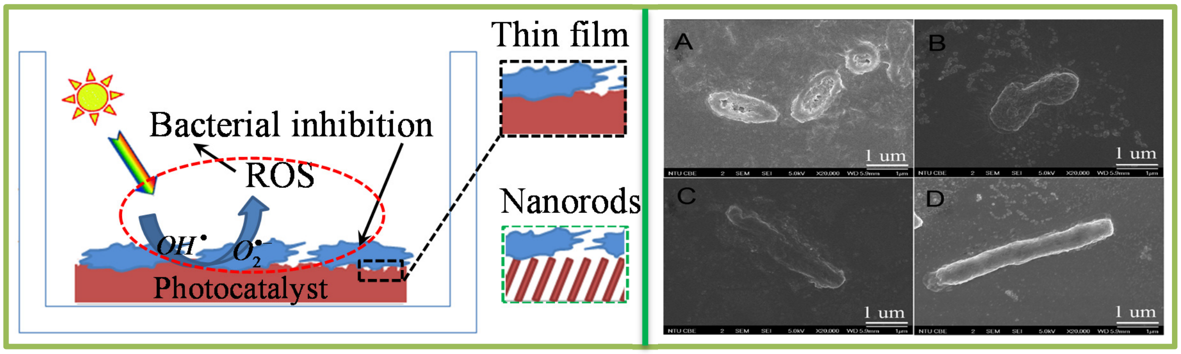

Fig. 1.14 Schematic diagram showing bacterial inhibition on the surface of photocatalyst where the light is irradiated from the top (onto the bacterial suspension). Note that the figures in the middle represent the two situations: (top) when the photocatalyst is thin film which has comparatively more smooth surface contact with bacteria than the contact with nanorods (bottom). SEM images on the right show the representative image for cell damage due to ROS (a)-(c) and (d) is from control experiment, i.e. without photocatalyst and light; image from Ref. [4].

1.2.2.4.3 Photoelectrochemical

The photocatalyst in a PEC cell can be used in three different ways, namely: i) particulate semiconductor, ii) semiconductor photoanode/cathode, and iii) tandem configuration.[44, 45, 52] In this work, we deal with the PEC system of type (ii) to characterize the PWS reaction. Thus, we will only discuss the photoanode/cathode, throughout this work, unless otherwise mentioned. Fig. 1.15 illustrate a general schematic for the PWS reaction, which does not represent any specific type of electrode but both photo-cathode and anode. The surface reaction on the photocatalyst has not defined specifically for either hydrogen evolution reaction (HER) or oxygen evolution reaction (OER) (see Fig. 1.15). Regardless of the electrode type, the half reaction of water splitting can be written as,

Oxidation: $2H_2O + 4h^+ \rightarrow O_2 + 4H^+$ (1.36)a

Reduction: $2H^+ + 2e^- \rightarrow H_2$ (1.36)b

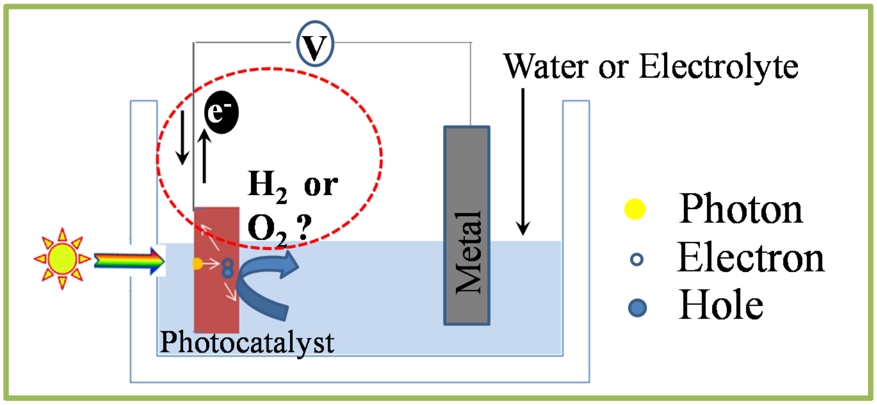

Fig. 1.15 Schematic showing water splitting in a PEC cell. Note that the question mark after H_2 or O_2 represents the possibility for both oxygen evolution reaction (OER) or hydrogen evolution reaction (HER) that is determined by the photocatalyt whether it is a photoanode (usually n-type) or a photocathode (usually p-type) respectively.

The overall PWS reaction is an uphill reaction (ΔG = +237 KJ/mol), and can be written as,

$$H_2O + 2h\nu \rightarrow H_2(g) + 1/2\, O_2(g)\,. \tag{1.37}$$

By knowing the majority (or the minority) charge carriers on the photocatalyst, we can predict the HER or OER onto the photocatalyt's surface: if the photocatalyst is of n-type and hence used as a photoanode, it should oxidize the water such that at the counter electrode (usually Pt) H_2 evolution occurs and *vice versa*. It is well known that besides the measurements of H_2 and O_2 evolutions, the PEC properties of a photocatalyst can be compared in several different ways. For instance, photoinduced photocurrent I (or photocurrent density, j_{ph}) with the known input power and area of incident light beam (or the number of photons absorbed) can be utilized to compare the PEC performances.[52-57] In this dissertation, we estimate the IPCE for quantitative comparison, which follows

$$IPCE\,\% = \frac{I(\text{in amp})}{P(\text{in w})} \times \frac{1240}{\lambda(\text{in } nm)} \times 100\,, \tag{1.38}$$

where $I(\lambda)$ and $P(\lambda)$ are the photocurrent and power of the incident light respectively (see Appendix B for full derivation).

It is worth to mention that the external bias potential (cathodic or anodic) has a strong effect on photocatalytic performances, including HER, OER and IPCE, that is depending on the band edge position as well as the type of photocatalyst.[17, 44, 58] Besides, the band bending at the semiconductor-electrolyte interface also affects the performance when the external bias potential is applied as shown in Fig. 1.16.[52] This activity may change regardless of other experimental conditions but the material's intrinsic property. As seen in the Fig. 1.16, the VB and the CB are bent down within the space charge layer representing the *n*- type semiconductor. This is because of the formation of a depletion layer at the interface where the minority carriers are consumed faster than that generated by anodic applied bias. The opposite can be expected with *p*-type semiconductor, which result in an upward bending.

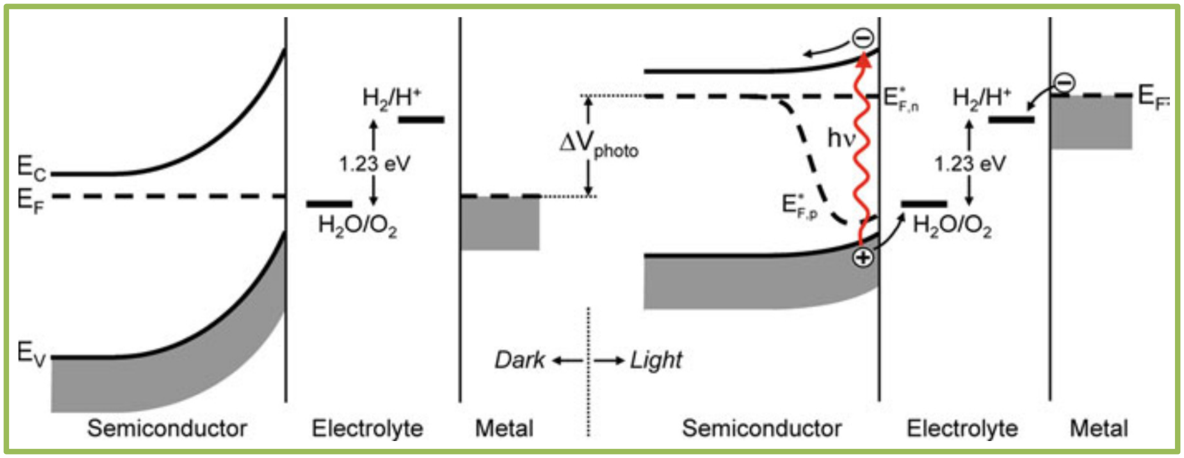

Fig. 1.16 Energy diagram of Fig. 1.15, obtained by assuming the photocatalyst is an n-type (photoanode) that is connected to a metal counter electrode; in equilibrium dark (left) and under the light illumination (right). Illumination raises the Fermi level and decrease the band bending. Note that near the semiconductor/electrolyte interface, the Fermi level splits into quasi-Fermi level for the electrons and holes.

1.3 Ways to Improve the Photocatalytic Activity

Based on the heterogeneous photocatalytic principles and proposed mechanisms described above, the photocatalytic activity of MO photocatalysts will be influenced by various factors such as, 1) absorption capacity and bandgaps, 2) morphology, 3) phase, 4) crystallinity and crystal facets, 5) crystal size, 6) preparation methods, 7) crystal defects, 8) surface property, and so on. Therefore, every single improvement in each of these properties will have a positive influence on photocatalytic activity. Specifically, light absorption properties can be tuned by choosing a right material of a suitable bandgap (see Fig. 1.17). Usually, crystallinity and crystal facets can be tuned by varying the post deposition treatment, for example, annealing at different temperature for different time intervals. Based on our observation, crystalline size of the nanostructures usually increases with the annealing temperature and photocatalytic efficiency decreases with increasing size. So, an improved photocatalytic activity is expected with decreasing both the particle and crystal sizes. Preparation methods may play more than one role in photocatalytic performance. For example, a method that produces more porous structure will result in a better photocatalyst. Similarly different surface properties of the photocatalysts may yield different activities based on the preparation techniques. Control the defect and defect density is essential for recombination rate optimization. Based on above discussion, in this dissertation, I want to explore how different factors affect the photocatalytic performance. Thus, we will adapt the following two strategies (have discussed in next sections).

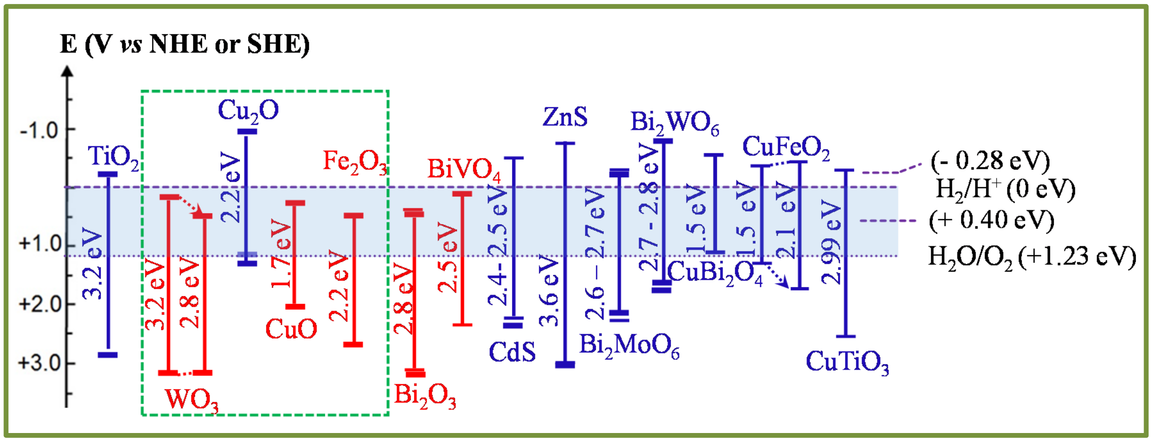

Fig. 1.17 Bandgaps and band-edge positions of some selected semiconductors photocatalysts at pH = 0. Note that the number shown in right are redox potentials of some useful couples that will be discussed more in detail in the next sections.

1.3.1 Material Selection

Material selection is not only based on its bandgap (or light responsivity) but also depends on many other factors that could affect the overall photocatalytic performance, especially depending on the nature of application. The bandgap and band edge location will dominate the material selection. As shown in Fig. 1.17, all the photocatalysts represented by red color have their CB edge at higher (positive) potential compared to the ones that are represented by blue colors (and the CB of photocatalysts in blue color are all at negative potential). In this case, the photocatalysts that are represented by blue colors should exhibit more reduction power (compared to the ones in red color) or *vice versa*. In a close inspection, almost all photocatalysts, except the $CuBi_2O_4$, have their VB at positive enough potential to oxidize O_2 (+ 0.40 V) and water (+1.23 V). So, all the photocatalyts represented by blue color (except $CuBi_2O_4$) are more favorable to exhibit overall PDD and bactericidal activities. In this dissertation, we choose the photocatalysts, namely WO_3 (E_g ~2.8 to 3.2), Cu_2O (E_g ~ 2.2 eV), CuO (E_g ~ 1.7 eV), and Fe_2O_3 (E_g ~ 2.2 eV) to study their dye adsorption, PDD, PEC, and bactericidal properties. The main reason for choosing WO_3 is because it is amorphous when as prepared and has high porosity due to our fabrication method. As a result we can expect an enhanced dye adsorption capability, which is of advantage for the wastewater treatment. In addition, the surface functionality of WO_3 is favorable for cationic dye adsorption due to electrostatic interaction between the negatively charged surface of WO_3 and the positively charged dye molecules. The choice of Cu_xO (x = 1, 2) is due to three main reasons: 1) single phases Cu_2O and CuO and the mixed phase Cu_2O/CuO can be obtained easily by tuning the oxidation condition (annealing temperature), 2) suitable bandgap for visible light absorption, and 3) band edges of each phase are perfectly aligned such that we can tune the external potential bias to optimize the solar conversion efficiency. In addition, we can also compare the PDD efficacy for all single and mixed phases based on the redox potential and the charge transfer at interfaces. Finally, the choice of Fe_2O_3 for PDD and bactericidal application is due to the fact that it is naturally abundant, cost-effective, highly stable, efficient in visible light absorption, and more importantly it is approved by the Food and Drug Administration (FDA) to be used in human, which is critical for antimicrobial coatings in food related applications. It is important to make a note that the CB and VB positions of these photocatalyst may change slightly depending on the reaction environment so that different redox reactions can be expected *via* multiple electron transfer. Besides, Cu_2O is a p-type semiconductor while both WO_3 and Fe_2O_3 are n-type so that different photocatalytic activity can be expected. The advantage of CB of Cu_2O being strongly negative can be utilized to split the water by reduction. The Cu_2O can also be optimized for charge transfer when mix with Fe_2O_3 or lower bandgap CuO.

1.3.2 Dynamic Shadowing Growth

Another critical factor for photocatalysts is the fabrication. Compared to various other popular wet chemical and vapor deposition methods, dynamic shadowing growth (DSG) is a scalable, reliable and simple nanofabrication technique. DSG method has been used in fabricating various nanostructures materials, *i.e.*, from simple component to complex geometry and composition.[59, 60] DSG grown nanostructures have been used extensively for photocatalysts.[10, 61-63] DSG is a process based on the geometric shadowing effect and substrate rotation in a physical vapor deposition (PVD) system as illustrated in

Fig. 1.18. As shown in the figure, the DSG process is associated with the so-called oblique angle deposition (OAD). By changing orientation of the substrate's azimuthal and polar angles with respect to the incoming vapor flux, the shadowed area can be controlled dynamically resulting different nanostructures (see Fig. 1.19(a)-(e)). A simplest case, at θ = 0° a continuum film will be obtained regardless of the substrate's rotation (Fig. 1.19 (a)). At higher deposition angle, typically $\theta \geq 70°$, and without substrate's rotation tilted nanorods will be formed (see Fig. 1.19 (b) and (d)). At $\theta \geq 70°$ and with a rotating substrate, *i.e.*, at a certain speed ω, vertical nanorods can be produced (see Fig. 1.19 (b) and (e)). During the DSG or OAD process, the arriving material accumulates into islands or nuclei that are randomly distributed along the surface of the substrate. The size of these nuclei depends on the adatom mobility. For instance, faster adatoms create nuclei with larger diameters while slow diffusion of adatoms result the smaller nuclei. As a result, the taller islands act as the shadowing centers due to the geometric shadowing effect and block material accumulation on the smaller islands during the deposition. This random competitive process will eventually produce nanorod arrays that are tilted towards vapor incident direction as shown in Fig. 1.19 (d).

It is worth noting that the nanorod tilting angle β does not follow the same angle as vapor incidence angle θ. As shown in Fig. 1.19 (c) the OAD process for tilted nanorods depends upon a collimated vapor flux that is incident on a bare substrate at angle θ.[64] The two most established theoretical models for the prediction of β are given by so called tangent[65] and cosine rules,[66]

$$\tan\alpha = 2\tan\beta, \tag{1.39}$$

and,

$$\beta = \alpha - \arcsin\left[\left(1 - \cos\alpha\right)/2\right] \text{ respectively.} \tag{1.40}$$

The detail of growth mechanism of nanorods in OAD is a complex process. For example, the growth of OAD nanorods depends on shadowing between columns, deposition temperature, deposition rate, deposition pressure, vacuum composition, substrate type, and also the preferred crystallinity of the deposited material. Detailed descriptions of the growth process can be found in some of recent review articles.[67, 68]

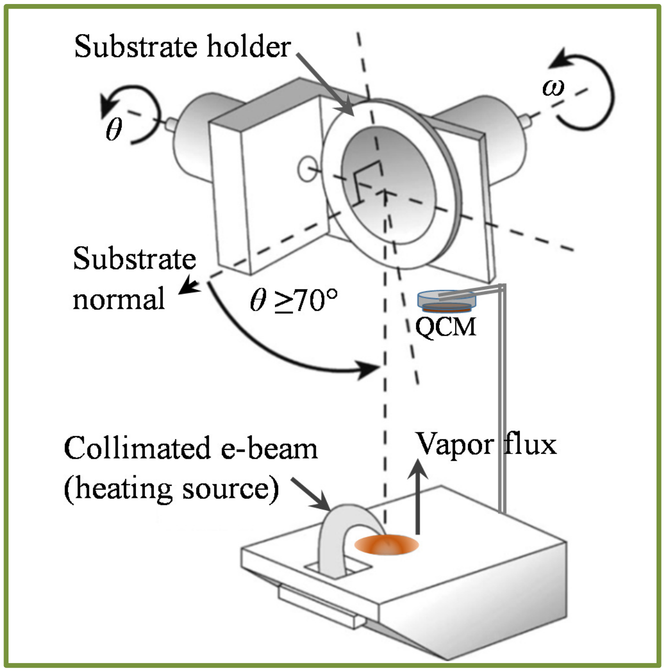

Fig. 1.18 Schematic diagram of dynamic shadowing growth (DSG) deposition.

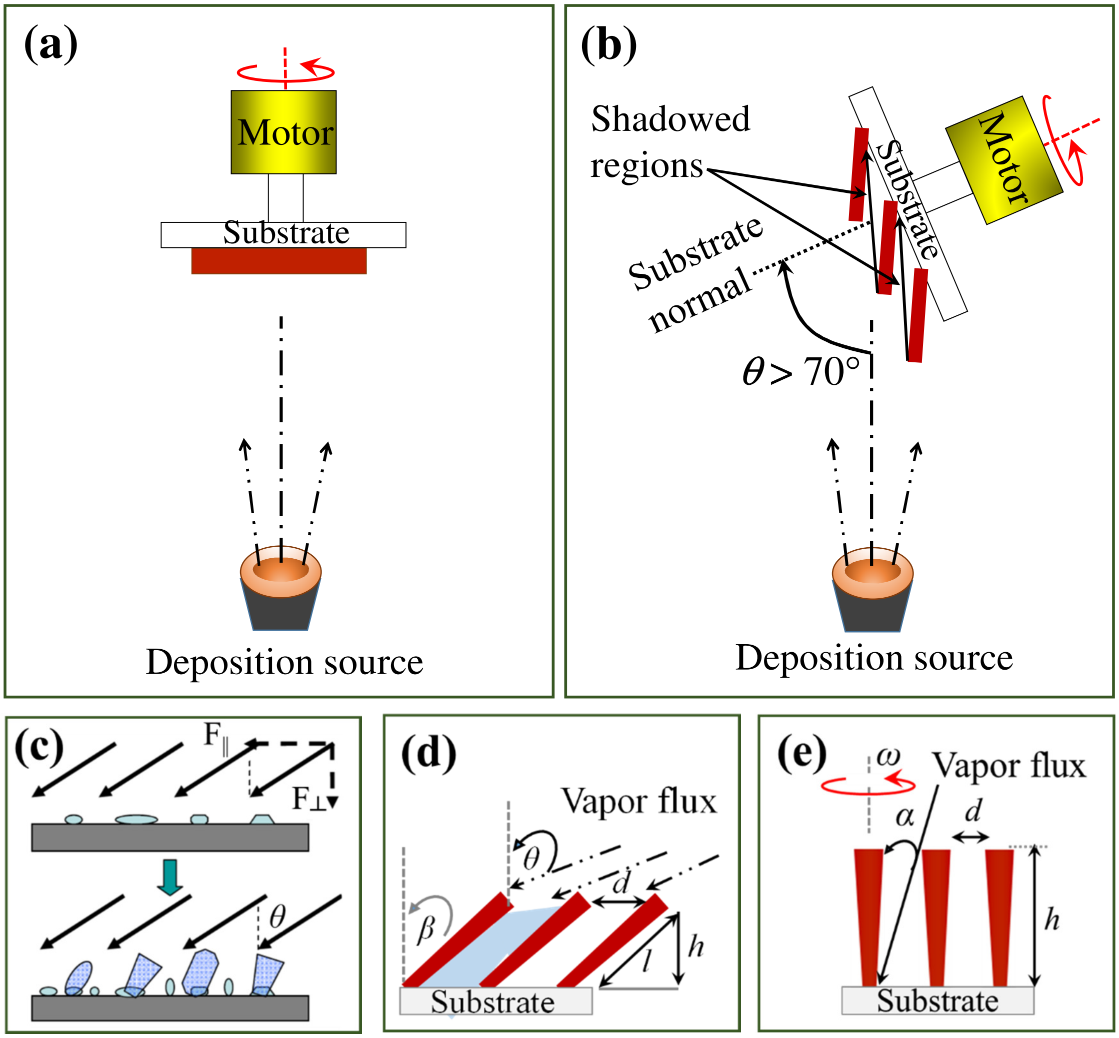

Fig. 1.19 Schematic showing e-beam depositions for (a) Thin Films at normal incidence and (b) Nanorod (NR) arrays at Oblique/Glancing Angle Depositions (OAD/GLAD). (c) Initial nuclei formation (top) and subsequent nanorod growth (bottom), (d) OAD deposited tilted NR arrays, and (e) GLAD deposited vertically align NRs.

Overall, the DSG process is advantageous based on the fact that one can control the porosity of nanostructured thin films.[10, 11, 62, 69, 70] Table 1.1 below summarize some of the important features including pros and cons of the DSG system.

Table. 1.1 summary: some of the important features of DSG system configured with e-beam.

System	Features	Pros	Cons	Ref.
DSG configured with e-beam evaporator	Films (both thin & thick), nanorods, nanocolumns can grow fairly easily, quickly and at low cost under the high vacuum.	1.Flexible; Versatile; Inexpensive 2. Scalable fabrication 3.Precise control over morphology 4.Almost no material limitation (metals, MOs, metal sulfides etc.) 5.Highly porous nanostructure (large surface area) 6.High reproducibility	1. Stability 2. Typically amorphous 3.Random nucleation	11, 61, 71-74

1.4 Dissertation Overview

This dissertation is divided into six Chapters. Chapter 1 serves as an introduction to this dissertation. It begins by describing the need of VLAP mainly focusing on three applications such as dye degradation, solar energy conversion, and bactericidal application. Then it presents the fundamental principles for heterogeneous photocatalysis based on the properties of MO semiconductors and discuss the need for a simple and scalable fabrication method, the DSG. A brief summary of other Chapters is given below.

Chapter 2 presents some specialized measurement techniques I developed for photocatalytic activity characterizations, including reflectance measurement, dye degradation experiment, PEC measurement, and bactericidal process. The detailed experimental setup and data analysis are presented.

Chapter 3 addresses the cationic and anionic dye adsorption behavior of DSG deposited amorphous WO_3 sub-micron rods (SMRs). In this Chapter, we use an analytical model for equilibrium dye adsorption and kinetics.

Chapter 4 presents that the different phase of Cu_xO ($x = 1, 2$) nanorods show different photocatalytic activities for dye degradation and PEC. Photocatalytic degradation of MB (as cationic probe) and methyl orange (Meth.O) (as anionic probe) are characterized with single phases Cu_2O, CuO, and mixed phase Cu_2O/CuO. We find that the Cu_2O/CuO nanorods exhibit the excellent photocatalytic activity under visible light irradiation for both PDD and solar energy conversion. About 44% incident photon-to-current efficiency is obtained at incident light of wavelengths 400 nm.

Chapter 5 discusses the photocatalytic activity of α-Fe_2O_3 nanostructures for MB degradation and bactericidal activity under visible light irradiations. Both α-Fe_2O_3 film and OAD deposited nanorods (NRs) are used to compare the photocatalytic activity. We mainly focus on the morphology and photon absorption of these nanostructures to analyze the observed photocatalytic performances. The thin film samples are more efficient for MB degradation while the nanorod arrays are more efficient for inactivating *E. coli* O157:H7.

Chapter 6 gives the conclusions and future work.

CHAPTER 2

CHARACTERIZATIONS OF PHOTOCATALYST MATERIALS

2.1 General Characterization Techniques

As described in Chapter 1, the morphology, structure, composition, optical properties, etc. are important factors to determine the photocatalytic performance of a MO catalyst. Therefore, a thorough morphological, structural, composition, and optical characterization is important.[14, 15, 26, 39, 75] The morphology of the nanostructures will be examined by a field-emission scanning electron microscope (SEM) equipped with an energy dispersive X-ray spectroscopy (FEI Inspect F) and a transmittance electron microscopy (TEM) (FEI Tecnai 20). X-ray Diffraction (XRD) patterns are used to analyze the structural properties. The PANalytical X'Pert PRO MRD X-ray diffractometer is used to collect the XRD data with a fixed incidence angle of 1.5°. The XRD patterns are recorded with Cu Kα radiation (λ = 1.5405980 Å) in the 2θ range from 20°-80° at a step size of 0.014°. Ultraviolet-visible (UV-Vis) transmittance and extinction (absorption + scattering) spectroscopy are used to analyze the optical and electronic properties. A double beam UV-Vis light spectrophotometer (JASCO V-570) is used for the measurements. The range of scanning wavelengths is fixed from 200 to 850 nm. Additional characterization techniques for the above properties are also utilized when appropriate (and they are presented in the next chapters). After these general property characterizations, the photocatalytic performance of the samples is evaluated with respect to the above mentioned applications. Below we give a brief overview of the advanced characterization techniques we use and design in the dissertation.

2.2 Optical Characterization

It is very important to obtain an accurate estimation of the absorbance, A, of the photocatalytic films in order to accurately determine the bandgap of the material as well as the photocarrier generation rate. As we discussed in Chapter 1, usually people directly use the optical transmittance to estimate the optical absorbance. Such a procedure overestimates A since there are other losses that are counted for the absorbance, *i.e*, the reflectance and scattering (see Fig. 1.7, in Chapter 1). Usually, compare to the reflectance, scattering is small. Therefore, to better estimate A, one should take the reflectance into account. As shown in Chapter 1, the absorbance can be estimated by Eqn. (1.13), which means one need to measure both transmittance and reflectance at zero incident angle. In most cases, the transmittance can be measured by the commercially available instrument (UV-Vis JASCO- V570, in our case). However, not many commercial spectrophotometers can give a zero incident angle reflectance measurement. In order to obtain $R(\lambda)$, I have set up a custom reflectance measurement system as shown in Fig. 2.1. The system includes a monochromator (APEX Newport Corp., Model: 74100), a calibrated Si detector (Model: 70356) with a Lock-in amplifier (Merlin, Model: 70104), a 50/50 beam splitter (BS; THORLABS Inc. Model: 50/50 BSW26), and a focusing lens. Using this system, the reflectance ($R(\lambda)$) of a photocatalyst sample can be estimated by following three-step measurements. For clarity, the setup diagrams are shown in Figs. 2.1(A), (B) and 2.2(A),(B). First, we focus the light beam such that it does not cover the whole area of the detector and as a result all the incident light will be detected (in our case, beam size should be $\leq$ 10 mm × 10 mm). Then one records the intensity of the light source, $I_0(\lambda)$, without BS. Then, a BS is inserted at 45°, and the intensities of transmitted light $I_1(\lambda)$ and reflected light, $I_2(\lambda)$, are measured (see Fig. 2.2(A)). Finally, the BS is rotated 90° and the reflected intensity, $I_3(\lambda)$ from the sample is measured, *i.e.*, at 90° with respect to its previous position (see Fig. 2.2(B)).

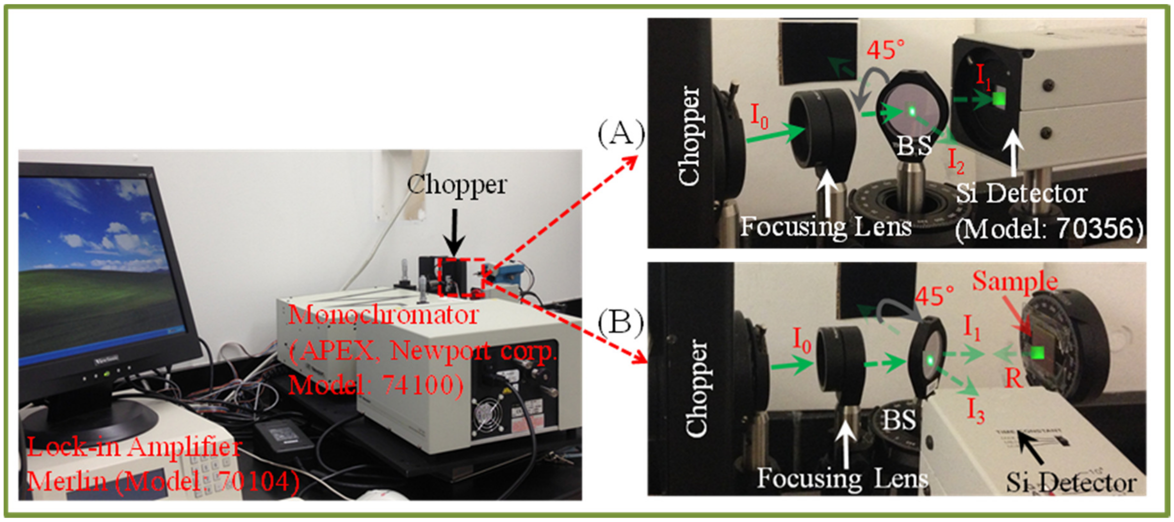

Fig. 2.1 Experimental configuration for reflectance, %R (λ), measurement at zero incidence angle: (fig. on left) shows monochromator assembly, (fig. on top right) shows the configuration for $I_0(\lambda)$, $I_1(\lambda)$, and $I_2(\lambda)$ measurements, and (fig. on bottom right) shows for the $I_3(\lambda)$ measurement, which include the reflectance of the sample.

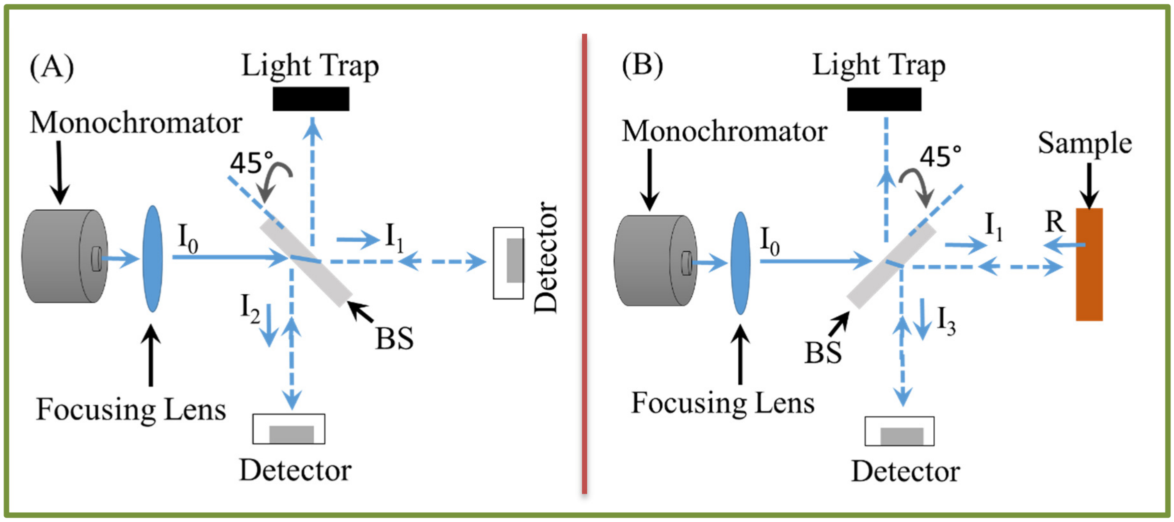

Fig. 2.2 Schematic diagram showing the reflectance, %R (λ) measurement using a calibrated 50/50 beam-splitter (BS): equivalent figures for Fig. 2.1 (A)-(B).

From the Figs. 2.2(A) and 2.2(B), the transmittance (T_{BS}) and the reflectance (R_{BS}) through the BS, are given by,

$$T_{BS}(\lambda) = \frac{I_1(\lambda)}{I_0(\lambda)}, \text{ and } R_{BS}(\lambda) = \frac{I_2(\lambda)}{I_0(\lambda)}. \tag{2.1}$$

And the reflectance of the sample can be estimated as,

$$R(\lambda) = \left(\frac{I_3(\lambda)}{I_0(\lambda) \cdot T_{BS}(\lambda) \cdot R_{BS}(\lambda)} \right), \tag{2.2}$$

where $T_{\mathrm{BS}}(\lambda)$ and $R_{\mathrm{BS}}(\lambda)$ are obtained from Eqn. (2.1). For an accurate measurement, a reflection calibration is carried out. For example, in our case, we measured the reflectance of a standard silver mirror (THORLABS Inc. Model: PF10-03-P01) whose reflectance is provided by the company. Replacing the sample by a silver mirror, its reflectance can be estimated as,

$$R_{Ag}(\lambda) = \left(\frac{I_3^{Ag}(\lambda)}{I_0(\lambda) \cdot T_{BS}(\lambda) \cdot R_{BS}(\lambda)} \right), \tag{2.3}$$

where $I_3^{Ag}(\lambda)$ is the reflected power of Ag mirror recorded on the detector (see Fig. 2.2 (B)). Dividing Eqn. (2.2) by (2.3), one can estimate the reflectance of sample $R(\lambda)$ by substituting the known ($R_{Ag}(\lambda)$) and measured quantities in equation,

$$R(\lambda) = R_{Ag}(\lambda) \cdot \left(\frac{I_3(\lambda)}{I_3^{Ag}(\lambda)} \right). \tag{2.4}$$

By substituting the estimated $R(\lambda)$ (and $T(\lambda)$) in Eqn. (1.13), one can estimate $A(\lambda)$ or $\alpha(\lambda)$. The $\alpha(\lambda)$ can further be used to estimate the optical band gap of a photocatalyst using a Tauc plot with the following relationship,[76-79]

$$\alpha h\upsilon = \alpha_0 (h\upsilon - E_g)^m, \tag{2.5}$$

where "hv" is the photon energy, "α_0" is a constant relative to the material, and "m" is an exponent indicating a direct bandgap material ($m = 1/2$) and an indirect bandgap material ($m = 2$).

2.3 Photocatalytic Dye Degradation

Photocatalytic dye degradation (PDD) activities of the prepared VLAP samples are evaluated by the degradation of MB (a cationic dye) and/or methyl orange (Meth.O; an anionic dye) aqueous solutions under visible light irradiations. All the experiments are conducted in the home-made photodecay system containing a photoreactor connected with an in-situ UV-Vis spectrophotometer as shown in Fig. 2.3. Dye degradation activity of a VLAP sample is measured at room temperature and ambient condition. In order to avoid the heat problem, caused by the light source, a running water filter is placed in between the sample and the light source. During the experiment, a Cuvette filled with a fixed concentration of dye is used, and the VLAP sample is placed on the side of Cuvette and illuminated by the excitation light. A 250 W quartz halogen lamp (UtiliTech) covering wavelength range from 400 to 800 nm is used. The incident light intensity on the sample is kept constant at 65 mW/cm^2 as measured by an optical power meter (Thorlabs PM100D/S310C). After a certain period of time, the UV-Vis absorbance spectrum of the dye solution is measured and analysed. We usually choose a characteristic absorbance peak of the dye to represent the relative dye concentration, as long as the concentration of dye satisfies the Beer's law. The absorbance peak will be normalized by the initial absorbance peak and is plotted as a function of time. From such a plot, we can use Eqn. (1.36) to obtain the photodegradation rate, k_c, according to the exponential relationship, $\alpha(t) = \alpha(t)e^{-k_c t}$.

Finally, the photocatalytic degradation results will be compared with control experiments performed without the VLAP and/or the light source.

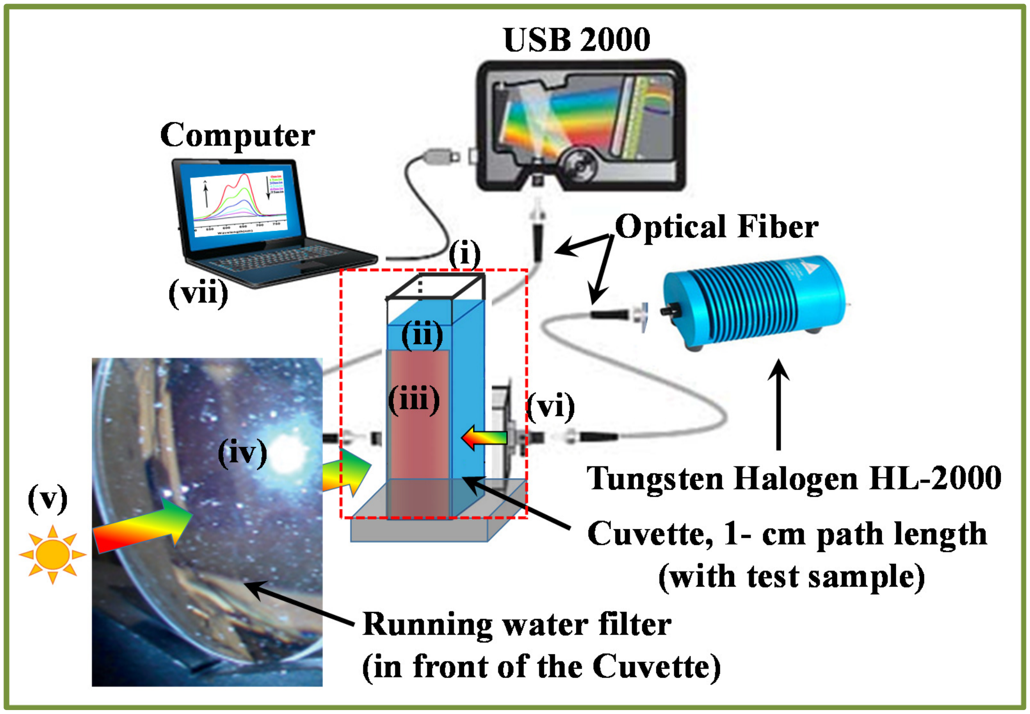

Fig. 2.3 Schematic diagram showing an experimental setup used for testing the photocatalytic dye degradation. Picture shows different parts in the setup: (i) Cuvette, (ii) MB aqueous solution (to be tested for degradation), (iii) VLAP sample whose activity is to be tested, (iv) running water filter (kept in front of the VLAP sample), (v) broad-band light source, (vi) optical fiber of UV-Vis spectrophotometer, (vii) monitor shows the absorbance of MB in time acquisition mode. The photoreactor (covered by red-dotted lines) is connected to a UV-Vis spectrophotometer (vi). Light source (v) is adjusted to focus towards the sample that passes through the running water filter.

2.4 Photoelectrochemical (PEC) Characterization

As mentioned in Chapter 1, we use a home-made PEC cell to characterize the solar conversion efficiency of the VLAP samples. The photocurrent and incident-photon-to-current conversion efficiency (IPCE) are the two most important parameters people used to characterize the PEC performance of the photocatalyst. I have set up a PEC cell to carry out such a characterization. A general diagram of the PEC cell using the catalyst as a photocathode is shown in Fig. 2.4, where the cathode is to reduce water and producing H_2 while O_2 is evolved at the counter electrode. The overall reaction is called the water splitting induced by the photocathode, which is usually a p-type semiconductor (Cu_xO in our case). In contrast, a photoanode (of n-type semiconductor) can be used to oxidize the water on its surface while the counter electrode reduce the water as a half-cell reaction.[5, 26] Experimentally, PEC measurements may require one or two separate units depending upon whether the source light is a monochromator or a broad-band.

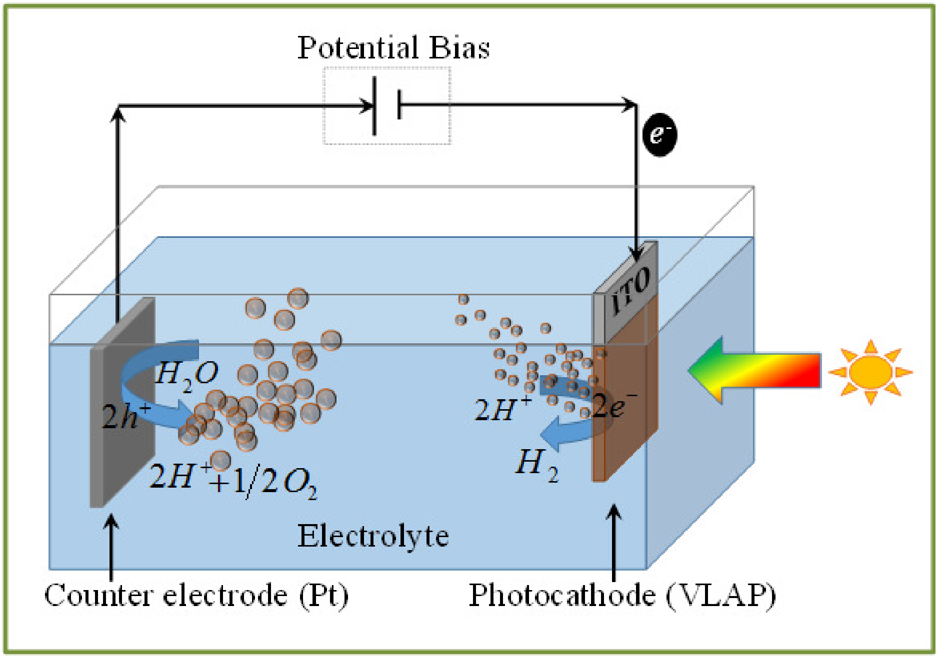

Fig. 2.4 Illustration of photocatalytic water splitting with a VLAP photocathode, as a working electrode. Note that the PEC cell shown here is an arbitrary showing only two-electrodes (cathode, the working electrode and the counter electrode, Pt wire).

For photocurrent I (or photocurrent density, j_{ph} (= I /Area of the sample)) *versus* time plot, we use a solar simulator (AM 1.5G, Oriel instruments, U.S.A., Newport corp. Model# 69911) while for IPCE we use a monochromator (APEX, Newport corp. Model: 74100) as shown in Fig. 2.5. Fig. 2.5 shows a complete setup for photocurrent measurement, which comprises mainly of three units: (i) a monochromator, (ii) a PEC cell, and (iii) a Potentiostat. A monochromator is required to compare the solar conversion efficiency as a function of wavelength so that we can obtain photocurrent $I(\lambda)$; otherwise, we replace it by a solar simulator to get only a photocurrent measurement. Fig. 2.6 shows a detail specification of the PEC cell, including the electrode's configurations.

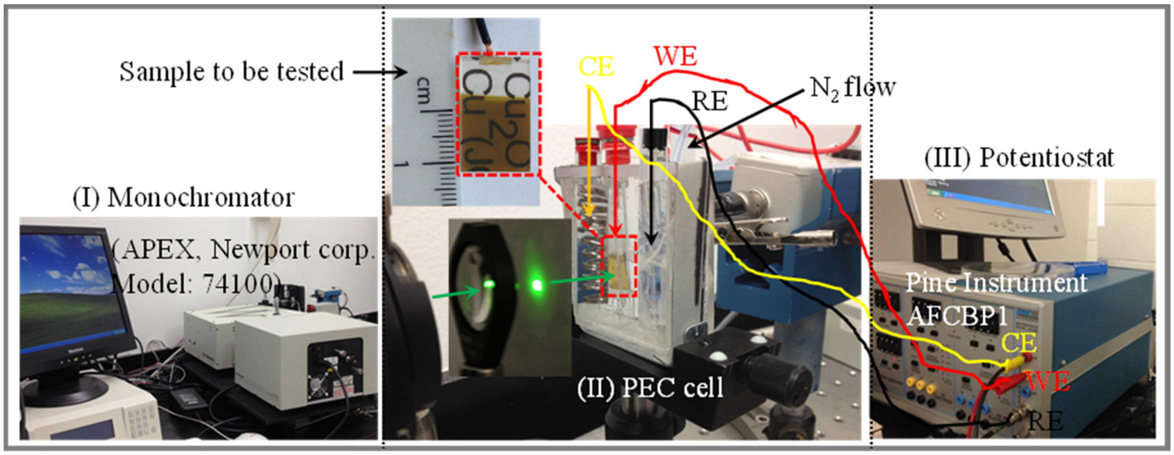

Fig. 2.5 Experimental setup for the photocurrent, $I(\lambda)$ measurement, in a PEC cell using, (i) a monochromator, (ii) a PEC cell, and (iii) a Potentiostat. Note that the sample to be tested (WE) is in figure insert (ii).

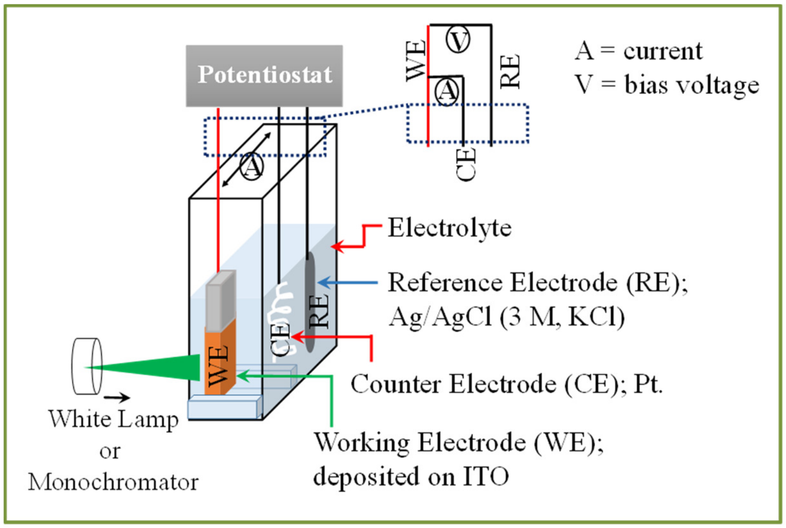

Fig. 2.6 A detail schematics of the PEC cell used for PEC characterization of the photocatalyst sample: part (ii) of the Fig. 2.5.

As seen in Fig. 2.6, we use a Potentiostat system (Pine Instrument AFCBP1 Bipotentiostat) to measure the photocurrent or the photogenerated current. We can set a required potential for chronoamperommettery measurements (I *or* j_{ph} - t relationship). Finally, from the known incident power spectrum $P(\lambda)$ and the stable photocurrent I, we estimate the IPCE, using the relation,

$$IPCE\% = \frac{I(\text{in amp})}{P(\text{in watt})} \times \frac{1240}{\lambda(\text{in nm})} \times 100 \,. \tag{2.6}$$

The detail derivation of Eqn. (2.6) is presented in Appendix. Note that we have measured and confirmed the reliability of measured $P(\lambda)$ of the monochromator's light by using a calibrated diode and the Si detector (of known responsivity [amp/w]). And we apply a suitable bias potential V (*vs* Ag/AgCl) to record the photocurrent I under the light illumination. The V (*vs* Ag/AgCl) is not the same as reversible Hydrogen electrode (RHE) or normal Hydrogen electrode (NHE) potentials, but they can be converted according to[56] V(RHE or NHE) = $V_{\mathrm{Ag/AgCl}}$ + 0.197 V + pH (0.059 V). All the potential values reported in this work are V versus $V_{\mathrm{Ag/AgCl}}$, unless otherwise stated.

2.5 Bactericidal Activity Characterization

The bactericidal activity of some selected VLAP samples are evaluated by the degradation of *E. coli* O157:H7 under the visible light irradiation. Fig. 2.7 shows the main steps for bactericidal activity tests: left column represents the steps for sample preparation of bacterial suspension and right column for the photocatalyst activity test. The predetermined initial concentration (10^7 CFU/ml) of the bacterial suspension are prepared by appropriate serial dilution in phosphate buffered saline (PBS, pH = 7). The VLAP samples and the clean glass samples (for control experiments) are first disinfected by irradiating them under the 30 W UV light (Osram Sylvania lighting Inc., Danvers, MA) for 30 min in a biological safety cabinet (Class II Type A/B3, NuAire, Inc., Plymouth, MN). Then 100 μl bacterial suspension is pipetted to each VLAP and glass substrates following the visible light irradiation for bactericidal activity measurements. The fluorescent light (Model 13 equipped with F13T5 lamps, StockerYale Inc, Salem, NH) is used by maintaining the fixed intensity (=10 mW/cm^2) onto the sample's surface for all experiments that are performed in cardboard enclosure at room temperature. Bacterial counting are performed for both VLAP and control samples at a regular time intervals and estimated the bacterial log reduction. Since the principle mechanisms of PDD and the bactericidal activity are the same (based on ROS; as described in Chapter 1), the bactericidal and dye degradation activity results are compared.

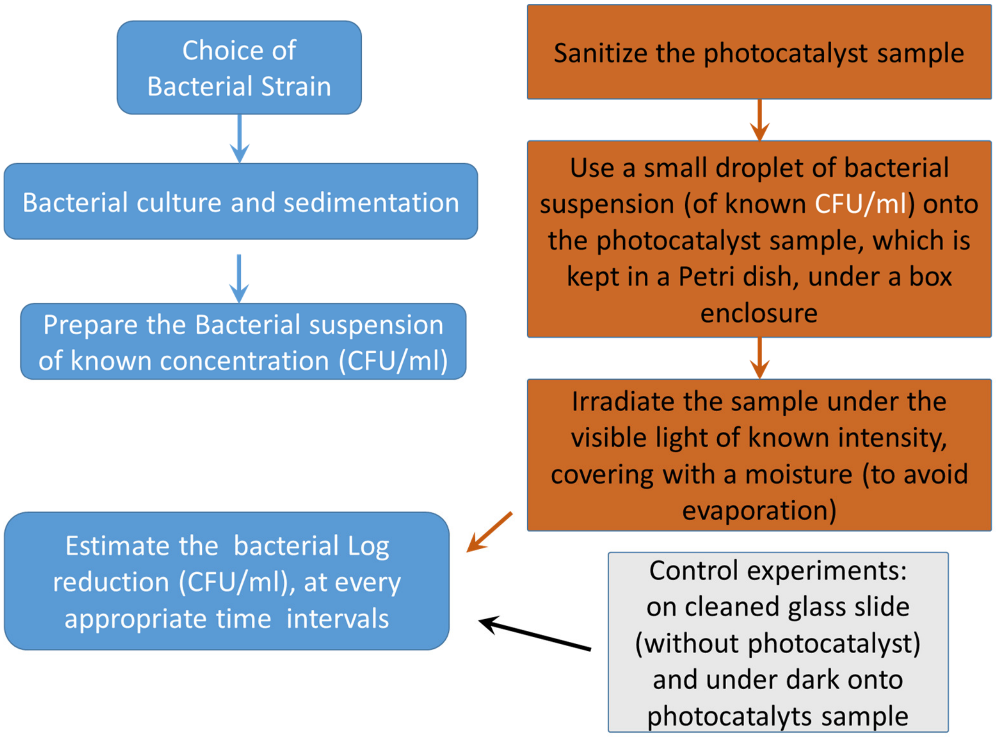

Fig. 2.7 flowchart showing the main steps in bactericidal activity test: left column represent the experiments carried out to prepare the required bacterial concentration and counting to estimate the log reduction and the right column represents the photocatalytic and control experiments.

CHAPTER 3

WO_3 SUB-MICRON RODS (SMRs) ARRAY AND DYE ADSORPTION

3.1 Introduction

The removal of reactive dye(s) from wastewater has attracted a lot of attention because most of the dyes are non-biodegradable, significantly toxic, and some of them are also carcinogenic.[49, 80-83] Adsorption has been found to be one of the most efficient ways to remove the dye effluents from the environment.[82-84] The use of Silica, Zeolites, Peat, and Chitin as adsorbents is limited as they cannot meet the growing industrial demand due to limited adsorption capacity.[82, 85-88] Powdered or granular activated carbon has been considered as the excellent adsorbent materials.[84, 89-91] Nevertheless, carbon-based materials must be treated as hazardous waste when thorough removal is required for trace amount of toxic dye effluents.[92] It is clear that the ideal material for the removal of toxic dye effluents should offer both excellent adsorption capability and surface activity that can degrade harmful pollutants.

Nanostructured semiconductor photocatalysts not only can have high dye adsorption capability, but can also generate e^-- h^+ pairs upon photon absorption. They can degrade toxic pollutants into harmless by-products through photocatalytic reactions. In particular, tungsten trioxide (WO_3) has recently emerged as an excellent photocatalytic material for dye removal.[93-95] However, their adsorption capability varies a lot depending on the morphology and preparation techniques, as summarized in Table 3.1. Compared to good carbon materials, the adsorption capability of WO_3 is still low.

In this Chapter, we report that amorphous WO_3 sub micrometer rods (SMRs) fabricated by glancing angle deposition have superior cationic dye adsorption capability that is comparable to that of the granular activated carbon. In addition, the photodecay performance of WO_3 SMR samples under UV irradiation increases when samples are annealed at higher temperatures.

Table 3.1 Summary of equilibrium adsorption capacities (q_e) of WO_3 related adsorbents, including experimental parameters.

Adsorbent/ Phase	Dye/ C_0 (μM)	m/V (mg/mL)	q_e (mg/g)	Ref.
WO_3 particles / Monoclinic	MB/ 50.0	500/250	~ 8	Morales *et. al.*[93]
WO_3 NRs[a]/ Hexagonal	MB/ 187.0	70/50	10 to 73	Zhu *et. al.*[96]
WO_3 NRs[a]/ Hexagonal	MB/ 312.6	10/10	88	Wang *et. al.*[97]
Commercial AC[b]/(N/A)	MB/ 312.6	10/10	85.9	Wang *et. al.*[97]
WO_3 SMRs/Amorphous	MB/ 50.0	0.48/3.0	149.8	Our work
WO_3 SMRs /Amorphous	R6G/ 50.0	0.48/3.0	176.5	Our work
WO_3 SMRs / Monoclinic	MB/ 50.0	0.48/3.0	29.5	Our work
WO_3 SMRs / Mixed[c]	MB/ 50.0	0.48/3.0	22.8	Our work

[a]NRs (nanorods). [b]AC (activated carbon). [c]Mixed = monoclinic + orthorhombic + hexagonal (mixed phase).

3.2 Experimental Methods

3.2.1 Fabrication

We used the GLAD technique discussed in Chapter 1 to fabricate amorphous WO_3 nanorod arrays onto glass and silicon substrates. The source material, Tungsten Oxide pieces, WO_3 (99.99+%, metal base), was purchased from Kurt J. Lesker (Clairton, PA) and used without further purification. The WO_3 SMR arrays were fabricated by a custom designed vacuum deposition system equipped with an electron-beam evaporation source (Torr International, Inc.). Both cleaned glass microscope slides (Gold Seal ® Catalog No.

3010) and Si (100) wafer (Montco Silicon Technologies Inc.) were used as substrates. The glass substrates were cut into sizes of 9.0 mm × 27.0 mm while Si substrates were cut into size of 10.0 mm × 10.0 mm. Glass substrates were cleaned with a mixture of sulfuric acid (H_2SO_4) and hydrogen peroxide (H_2O_2) solution, in a 4:1 ratio, by boiling about 15 mins and dried with nitrogen (N_2) flow. Si wafers were cleaned in a mixture solution of de-ionized (DI) water, H_2O_2, and ammonium hydroxide (NH_4OH) in a ratio of 5:1:1, boiling for 15 mins and dried with N_2 flow. For glancing angle deposition (GLAD), the deposition angle, the angle between the substrate surface normal and the incident vapor direction, was fixed to 86°. Prior to the deposition, the vacuum chamber was evacuated to a pressure of less than 1×10^{-6} Torr whereas during the deposition, the pressure was maintained to be in the range of $(3\text{-}7) \times 10^{-6}$ Torr. During the deposition, the substrate holder was rotated continuously and azimuthally at a speed of 0.25 rpm. The deposition rate and the deposited thickness were monitored by a quartz crystal microbalance (QCM) positioned directly facing the incident vapor. The deposition rate was maintained at 0.4 nm/s, and the final QCM thicknesses reading was 3 μm. The mass of the deposited materials was estimated by weighing the substrates before and after deposition using a high precision electron microbalance (Model: XP56, METTLER TOLEDO). For photocatalytic activity comparison of the amorphous (as-deposited) and crystalline WO_3 SMR samples, we annealed the as-prepared glass deposited WO_3 SMR samples at various temperatures, T = 300, 400, 500 and 550 °C, respectively, in a quartz tube furnace (Lindberg/Blue M Company) for 4 h in open air.

3.2.2 Morphology and Structure Characterization

As-deposited WO_3 SMRs on Si substrates were used for SEM and EDX analysis while samples deposited on glass substrates were used for the XRD analysis. As shown by the SEM (Fig. 3.1a & 3.1b) TEM (Fig. 3.1c) images, the as-deposited WO_3 films consist of an array of well-aligned and fibrous SMRs. From the SEM images, the SMRs are found to have an average length, $L = 1130 \pm 30$ nm, average diameter at top, $d = 180 \pm 40$ nm, average SMRs separation, $S = 130 \pm 40$ nm, and average SMRs density, $\eta = 12 \pm 3\ \mu m^{-2}$.

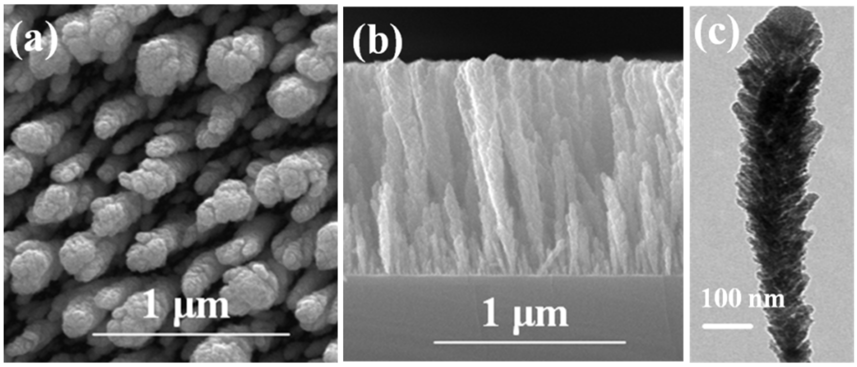

Fig. 3.1 (a) Top-view and (b) cross-section SEM micrographs of as-deposited WO_3 GLAD microrods arrays. (c) A TEM image showing the highly porous morphology of WO_3 microrods.

Fig. 3.2(a) shows the XRD patterns of as-deposited and annealed WO_3 SMR samples. No crystalline peaks are presented in the spectrum of as-deposited WO_3 SMR samples, indicating that the as-deposited WO_3 SMRs are in amorphous phase. From the figure, all annealed samples exhibited the polycrystalline WO_3 phases (mixed phases of Monoclinic (JCPDS ref: 43-1035), Orthorhombic (JCPDS ref: 20-1324) and Hexagonal phases (JCPDS ref: 85-2459)). A slight evidence of emergence of monoclinic phase was observed with a noticeable peak at $2\theta = 23.12°$ for $T = 300$ °C annealed samples, and was followed by above mentioned mixed phases with all discern peaks for $T \geq 300$ °C (up to $T = 550$ °C). For samples annealed at higher temperatures, i.e. 400 °C $< T \leq 550$ °C, hexagonal phase appeared to be dominating by comparing the relative peak intensity ratios. Fig. 3.2(b) shows the EDX spectrum of as-deposited WO_3 SMRs. Besides a strong Si peak coming from the Si substrate, the EDX spectrum only consists of O and W peaks.

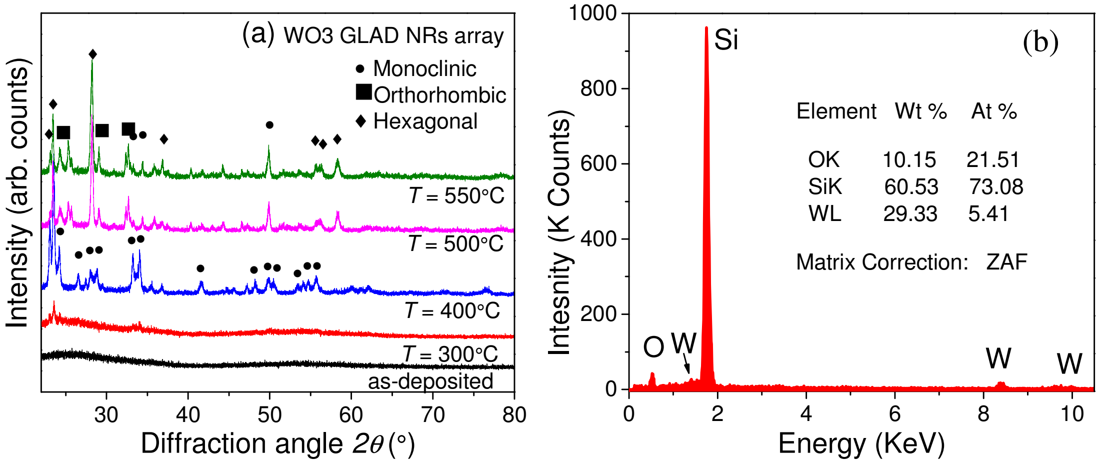

Element	Wt %	At %
OK	10.15	21.51
SiK	60.53	73.08
WL	29.33	5.41

Fig.3.2 (a) XRD spectrum of as-deposited and annealedWO_3 SMR samples, and (b) EDX spectrum of as-deposited WO_3 SMR sample.

3.2.3 Optical Characterization

The optical properties of the as-deposited and annealed WO_3 SMR samples on glass substrates were characterized by the UV-Vis spectrometer. Fig. 3.3 shows the UV-Vis absorbance spectra of as-deposited and annealed WO_3 SMR samples. Note that the absorbance spectra were recorded at normal incidence by neglecting the reflectance. Absorption edges are observed blue shifted with annealing temperature and extended beyond 800 nm when annealed at $T \geq 500$ °C (see Fig. 3.3).

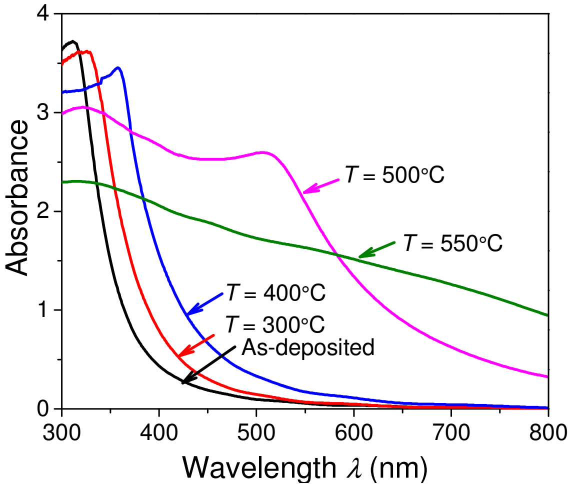

Fig. 3.3 Optical absorbance spectrum of as-deposited and annealed WO_3 SMR samples.

3.2.4 Zeta Potential Measurement

The Zeta-potential of the as-deposited WO_3 SMRs suspensions in pure DI water (18 MΩ·cm) were measured using Dynamic Light Scattering, Malvern Zetasizer Nano ZS (Model: ZN3600). The average Zeta-potential after 20 scan were recorded to be - 39 mV, at pH 8.1, indicating that the as-deposited WO_3 SMRs have an overall negative surface charge at slightly basic condition.

3.2.5 Adsorption Experiments

MB adsorption characterizations of the WO_3 SMRs samples in aqueous solution were performed at room temperature (25 ± 1 °C) with different initial MB concentrations C_0 (from 50 to 100 μM). All experiments were performed with predetermined mass, m = 1.52 ± 0.04 mg of WO_3 SMR samples and with a fixed volume, V =14 mL of MB solution. The prepared MB aqueous solutions were observed to have maximum absorbance at wavelength, λ_{max} = 664 nm (see UV-Vis spectra in Fig. 3.4(a)). A stock solution of MB was prepared by dissolving the accurately weighed quantity of MB powder, m = 64 mg, in DI water (18 MΩ·cm) to make 200 μM (initial concentration, C_0). To make a homogeneous solution, it was magnetically stirred for 12 h at room temperature. Experimental solutions of the desired concentrations of 50, 70, 80, 90 and 100 μM were obtained by sequentially diluting the base solution with DI water. The pH values of as-prepared MB aqueous solutions of 100 μM and 50 μM were slightly acidic, in the range of pH 6.2-6.7, respectively. A 50 ml glass bottle was used to perform the adsorption experiment with MB solutions. The bottle with a mixture of WO_3 SMRs (with glass substrate) and MB solution, of known mass and concentration, was shaken immediately (i.e. after immersing the glass-deposited WO_3 SMR sample in the MB solution) on an orbital shaker (Southwest Digital Shaker, Model: SBT300) at 300 rpm for the predetermined time (see Fig. 3.5). For lower concentrations ($C_0 \leq 70$ μM), the shaking time was chosen to be every 5 min while for higher concentrations, $C_0 \geq 80$ μM it was chosen to be every 10 min, until the adsorption get saturated. An aliquot sample (2 ml; solution mixture of WO_3 SMRs and MB solution) was taken out at every predetermined time, as mentioned above, and the absorbance spectrum was measured. Two successive experiments were performed in order to obtain the absorbance spectra of aliquot samples. In one experiment UV-Vis absorbance measurements were performed without centrifuging (WOC) the aliquot samples, and in the other experiment, the absorbance measurements were performed with centrifuging (WC) the aliquot samples at 15, 000 rpm (Eppendorf Centrifuge, Model: 5424). Then supernatant solution was taken out gently for the absorbance measurement, and the same procedure for absorbance measurements of all WC experiments was repeated. Two- to four-fold dilutions of the aliquot samples were performed, before absorbance measurements, if the expected concentration was higher than 30 μM, i.e., to make the concentration of MB solution ≤ 30 μM. As demonstrated by the MB solution calibration curve in Fig. 3.4(b), 30 μM was a concentration limit below which we can apply a linear calibration curve to estimate the concentration. All the adsorption experiments were conducted in duplicates, and only the mean values of remaining MB solution concentrations were reported for each concentration profile, $C(t)$. The maximum deviation in the remaining concentration values, in our experiments, was usually less than 5%. The control adsorption experiments without WO_3 SMR samples were also conducted to ensure that the decrease in the concentration was actually due to the adsorption of WO_3 SMRs.

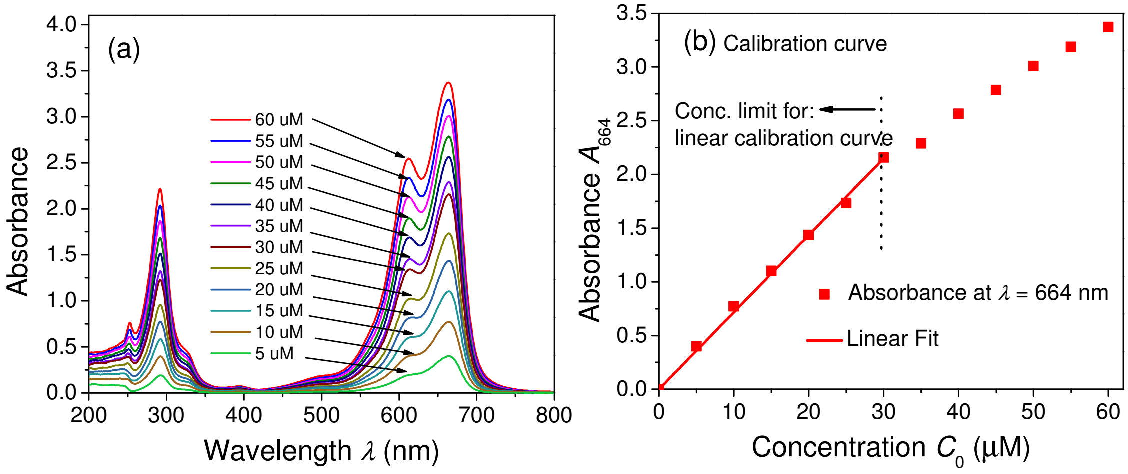

Fig.3.4 (a) UV-Vis absorbance spectra of MB aqueous solution with known concentrations and (b) calibration curve obtained from (a) using absorbance at λ = 664 nm.

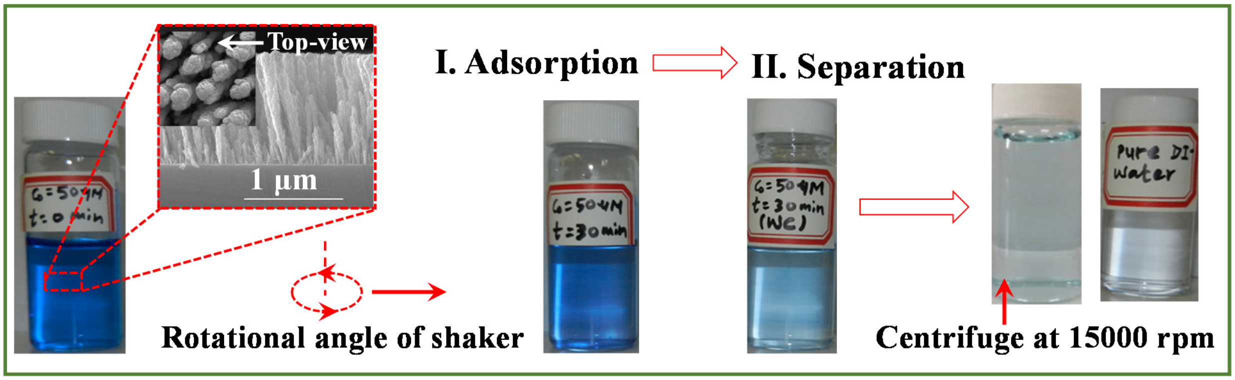

Fig. 3.5 Schematic diagram illustrating the decolorization of MB solution via adsorption onto WO_3 SMRs with and without centrifugation. Color change represents an equilibrium intake for total time of 30 minutes. The final color of the MB solution after separation of WO_3 SMRs through centrifugation is compared with pure DI water (two bottles in the right most corner).

3.2.6 FT-IR

Fourier transform infrared (FT-IR) and UV-Vis absorbance spectra were used to confirm the adsorbance of MB on the surface of WO_3 NRs and photocatalytic degradation under UV irradiation. Fig. 3.6 shows the FT-IR spectra of the WO_3 SMRs, MB, and MB-adsorbed WO_3 SMRs (MB/WO_3 complex). For FT-IR measurements, we used the as-deposited WO_3 SMRs sonicated off from the substrate in de-ionized (DI) water and MB solution, 50 µM. About 50 µL of each sample solution was pipetted on three-individual cleaned glass substrates and air dried. The same process was repeated about 10 times to form multiple layers of each type sample on the substrates before the measurements were performed. Then the FT-IR spectra were recorded for 500 to 4000 cm^{-1} at 120 scans with a spectral resolution of 2 cm^{-1} using Thermo-Nicolet 6700. Comparing the spectra of WO_3

SMRs, pure MB and MB/WO3 complex, the MB/WO3 complex spectrum confirms the adsorption of MB and shows a ring stretched vibrational mode at 1603 cm^{-1}.[98, 99]

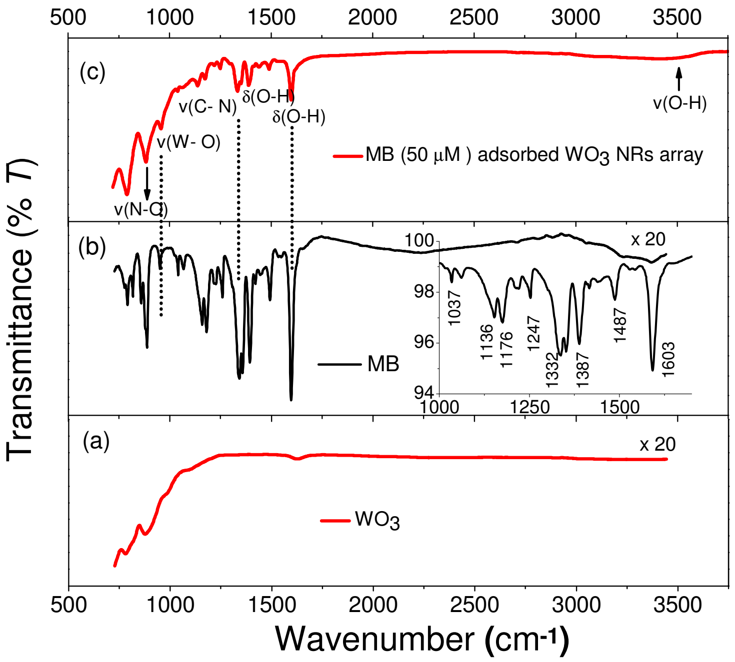

Fig. 3.6 FT-IR spectra of WO$_3$ SMRs before (a) and after MB-adsorption (c). Fig (b) shows the FT-IR spectrum of pure MB (for a comparison) with a zoom in spectra for 1000- 1700 cm^{-1} (inset)

3.3 Equilibrium Dye Adsorption

For dye adsorption experiments, decoloration of MB solutions was observed to cease after a certain period, about 30 min for $C_0 = 50$ μM and 60 min for $C_0 = 100$ μM. We regarded this time as equilibrium adsorption-time; and it varied with C_0. For different C_0, the equilibrium adsorption capabilities q_e were estimated from the equilibrium MB concentration C_e, by using the mass balance relationship,

$$q_e(mol/g) = \frac{(C_0 - C_e)(mol/L)V(L)}{m(g)}, \qquad (3.1)$$

where m and V are the mass of the adsorbent and volume of the MB solution, respectively. The C_e was estimated spectrophotometrically using a calibration curve (see Fig. 3.4(b)) and was examined for two different experimental conditions. One experiment measured the absorbance spectra for C_e of aliquot samples, where 2 mL volumes of mixture solutions of MB with WO_3 SMRs were pipetted out at predetermined times after shaking in an orbital-shaker without centrifugation (WOC). And in the other experiment, the aliquot samples were collected with centrifugation (WC) at 15,000 rpm for 1 min followed by the absorbance spectra measurement for C_e as described above.

In both cases, q_e were observed to increase with increasing C_0 while the percentage removals of MB concentrations $[(C_0 - C_e)/C_0 \times 100]$ were observed to decrease. It is worthwhile to mention that for the WOC process, 92.6 % removal of MB concentrations were observed for $C_0 = 50$ μM in 30 mins, while 74.6 % removal for $C_0 = 100$ μM in 60 mins. The WC process was observed to cause a further enhancement in adsorption capability. For the two concentrations above, the percentage removals were increased to 94.4 and 78.4 % respectively. The adsorption isotherms for both the WC and WOC processes were obtained after the adsorption for 90 min, and C_e/q_e *versus* C_e is plotted in Fig. 3.7. Both plots seem to follow a linear relationship, which indicates a Langmuir isotherm process, for which

$$\frac{C_e}{q_e} = \frac{1}{Q_m K} + \left(\frac{1}{Q_m}\right) C_e, \tag{3.2}$$

where Q_m and K are the Langmuir constants related to monolayer adsorption capacity (mol/g) and surface energy (L/mol) at equilibrium, respectively.[84, 100-102] Both the Q_m and K values can be obtained from linear fitting: for WOC process, $Q_m = 750 \pm 20$ μmol/g, K

= 0.21 L/μmol and for WC process, Q_m = 780 ± 20 μmol/g, K = 0.32 L/μmol. The equivalent Q_m values are estimated to be 240 and 250 mg/g respectively for WOC and WC.

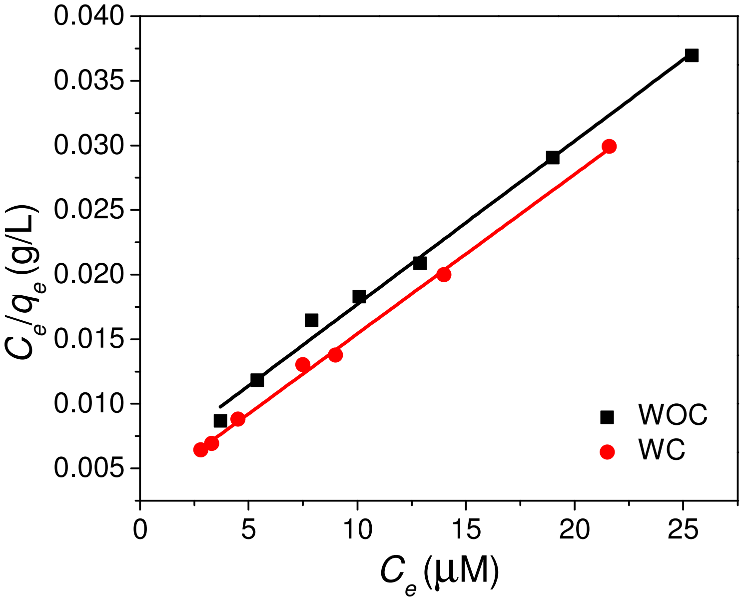

Fig. 3.7 Langmuir plot of adsorption isotherms.

These Q_m values are 30 ~ 31 times higher than those reported for crystalline WO_3 nanoparticles synthesized by combustion method[93] and comparable to granular activated carbon.[95] To the best of our knowledge, these amorphous WO_3 SMRs exhibited the best adsorption capacity among any other WO_3 nanostructures, fabricated by different methods.[93, 96, 97] Not surprisingly, we obtained a higher Q_m value for the WC experiment since the centrifugation can allow the MB molecules to access more WO_3 surfaces, such as nanopores or nano-fibrous surfaces. In addition, we observed that WC process break the WO_3 SMRs into sponge-like nanoscale networks as shown in the SEM and TEM images in Fig. 3.8 which further confirms the increase of surface area. Such a network structure is the result of high mechanical force applied to the sample during centrifugation. However, if the amorphous WO_3 SMRs were annealed to change their crystalline phase, the dye adsorption properties will also change. MB adsorption experiments have been performed on the WO_3 samples annealed at $T = 300$, 400, 500 and 550 °C, respectively (see Fig. 3.9). With increased annealing temperature, the MB adsorption decreases. This could be primarily due to the decrease in total surface area of the nanostructure *via* crystallization and coarsening of nanorods.

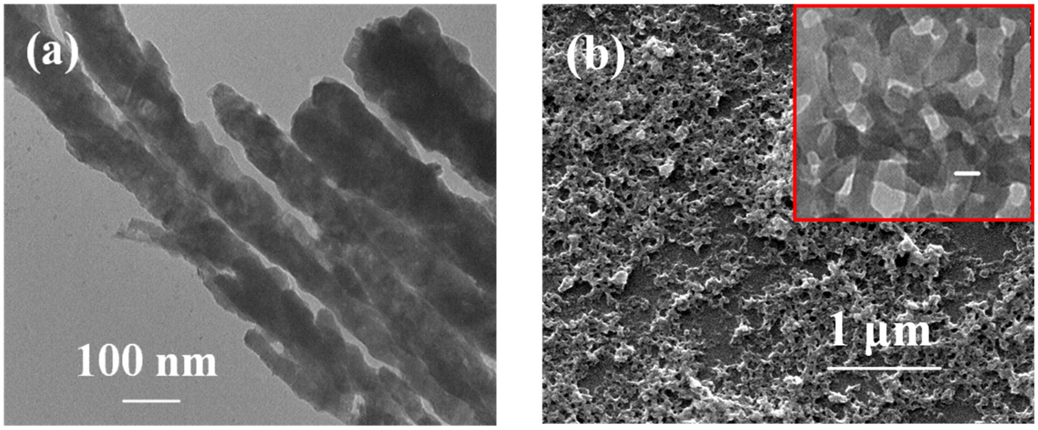

Fig.3.8 (a) TEM image of WO_3 SMRs after MB adsorption experiment without mechanical agitation such as shaking & centrifugation; and (b) SEM image of WO_3 SMRs after MB adsorption experiment with centrifugation (formation of sponge-like nanoscale networks). The inset shows a TEM image (scale bar = 20 nm) of disintegrated WO_3 SMRs after MB adsorption with centrifugation at 15,000 rpm.

Similar adsorption experiments have been performed on three other dyes for amorphous WO_3 SMRs, one cationic dye Rhodamine 6G (R6G), and two anionic dyes, Methylene Orange (MO) and Phenol (Ph) under similar experimental conditions. The adsorption capacity of R6G is similar to that of MB, while for MO and Ph little adsorption has been observed (see Table 3.2). This suggests that the dye adsorption process onto the WO_3 nanoorod surface is dominated by the electrostatic interaction.

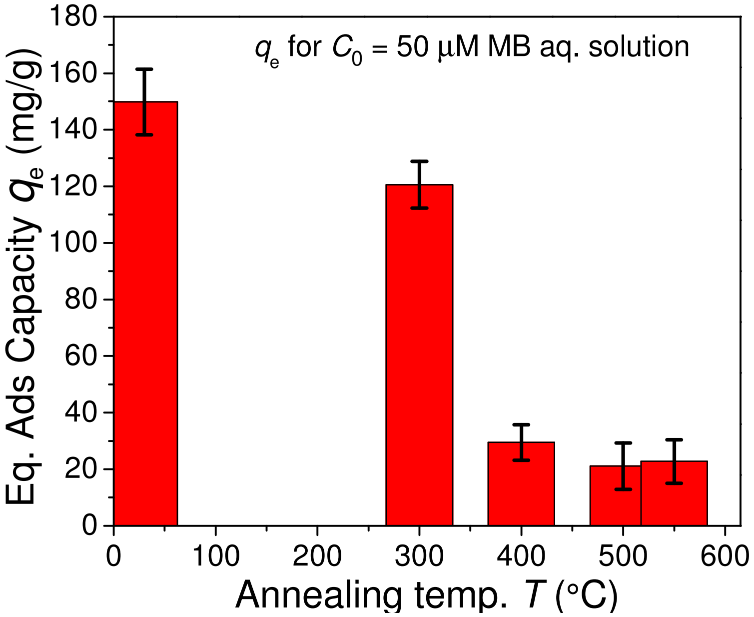

Fig. 3.9 Equilibrium adsorption capacity, q_e versus annealing temperature T of WO_3 SMR samples.

Table 3.2. Summary of q_e and other experimental parameters for cationic and anionic dye adsorptions.

Dye (fixed volume, V= 3 ml)		Mass of adsorbent, m (mg) (amorphous WO_3)	Equil. ads. cap., q_e (mg/g)
Dye/ type	Initial Conc. (C_0)		
MB/ cationic	50 µM	0.48 ± 0.04	149.8
R6G/ cationic	50 µM	0.48 ± 0.04	176.5
MO/ anionic	20 µM	0.48 ± 0.04	2.5
Ph/ anionic	50 µM	0.48 ± 0.04	3.0

3.4 Dye Adsorption Kinetics

Besides the adsorption capacities, the kinetics of dye removal is also investigated through the time-dependent MB concentration measurement during adsorption. A typical plot of remaining MB concentration in solution, $C(t)$, for C_0 = 50 μM versus adsorption time t is shown in Fig. 3.10 for both WC and WOC processes. The inset photographs show the color change of the solution before and after reaching adsorption equilibrium (t = 30 min). The rapid MB adsorption at the initial stage (~10 mins for 50 μM) may be attributed to stronger electrostatic attraction and also the more available surface area. This tendency becomes slower as the time passes due to the less vacant adsorption sites available for MB molecules (until the adsorption saturation is attained). From $C(t)$, the time dependent

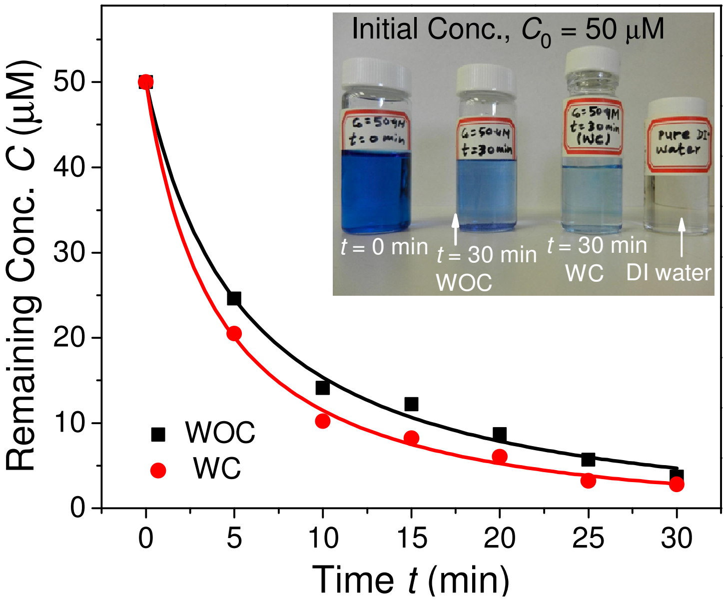

Fig. 3.10 Time dependent MB concentration C (t) for C_0 = 50 μM for WOC and WC processes. The inset shows the decoloration of MB solution before and after equilibrium adsorption.

quantity of adsorbed MB, q_t was calculated using Eqn. (3.1). Since the adsorption follows the Langmuir isotherm, the $q_t \sim t$ relation should be determined by a pseudo-second-order kinetic model,[101, 103, 104]

$$\frac{dq_t}{dt} = K_2 (q_e - q_t)^2 , \tag{3.3}$$

where K_2 is the rate constant of pseudo-second-order model. Eqn. (3.3) can be reduced to

$$\frac{t}{q_t} = \frac{1}{K_2 q_e^{\ 2}} + \frac{t}{q_e} \ . \tag{3.4}$$

The plot of t/q_t versus t should show a linear relation, and the data fitting can extract K_2 and $1/K_2 q_e^2$. The plots of t/q_t versus t, including fitting values of K_2, $K_2 q_e^2$, and fitting correlation coefficients are presented in below (see Fig. 3.11(a)-(g) and Table 3.3). The results show that the K_2 is a complex function of C_0, as described by Azizian's theoretical analysis.[103] In fact, based on Azizian's paper, the adsorption rates K_a, as a function of C_0, can be estimated by

$$K_a = \frac{2 q_e K_2}{\left[\frac{(C_0 - C_e)}{\theta_e} + C_0 + \sqrt{\left[\frac{(C_0 - C_e)}{\theta_e} + C_0 \right]^2 - 4 C_0 \frac{(C_0 - C_e)}{\theta_e}} \right]} , \tag{3.5}$$

and K_a can be used to describe the adsorption process. Fig. 3.12 shows that in general K_a decreases with C_0 monotonically (except the data point at $C_0 = 60$ μM). This result is consistent with a report by Tsai *et. al.* for adsorption of acid dyes from aqueous solution on activated bleaching earth.[105] However, at higher concentrations, $C_0 \geq 80$ μM, the K_a values were observed to approach a constant. This could be attributed to the fact that the MB adsorptions at higher concentration will not follow the Langmuir type adsorption, and a pseudo-first-order reaction can be used to better describe the process.[103] In fact, for high

MB concentration data ($C_0 \geq 80$ μM) the pseudo-first-order model gives better data fitting, and the results are summarized in Table 3.3.

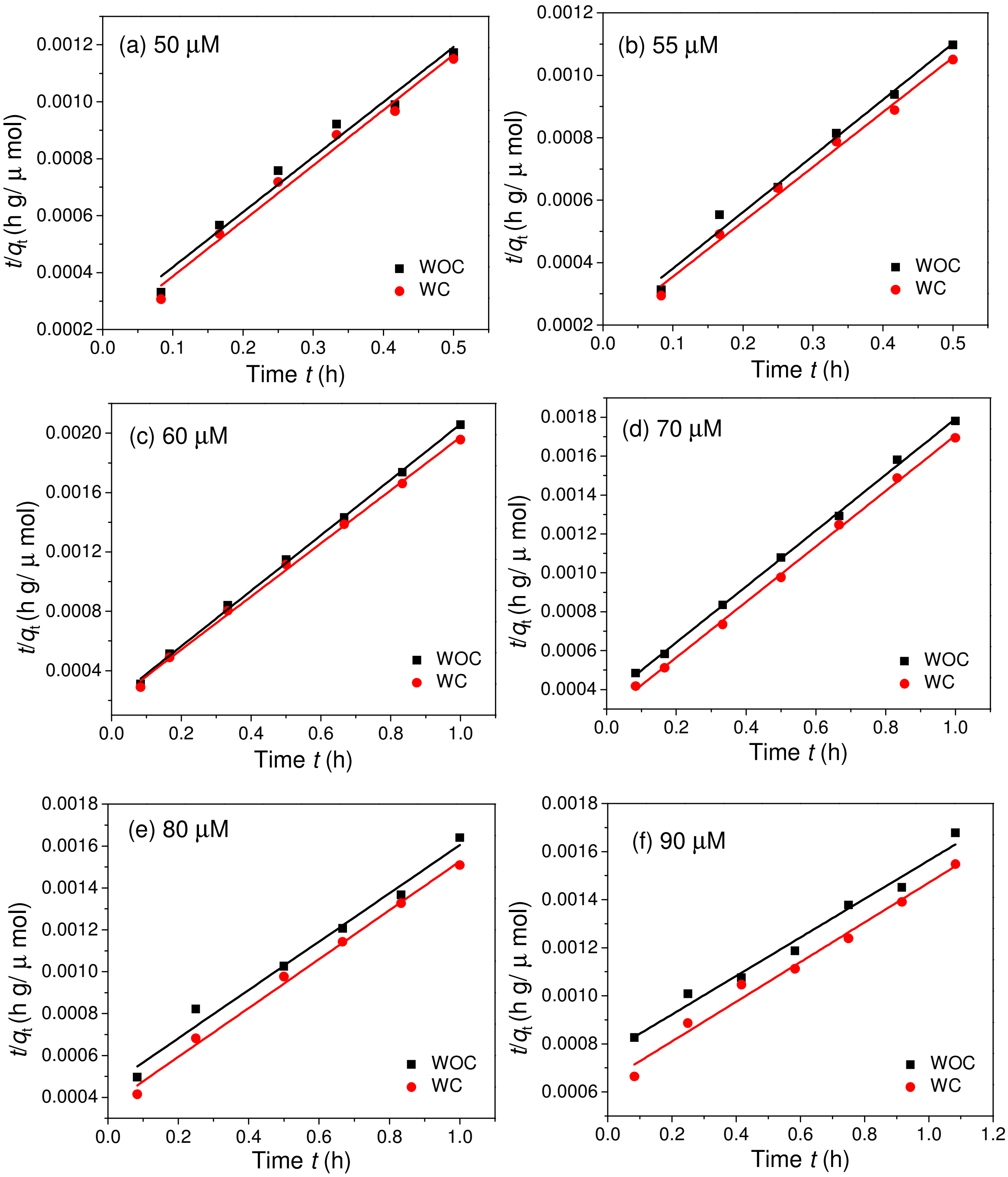

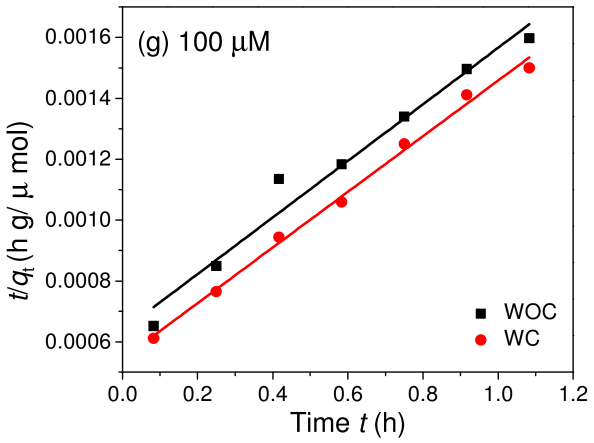

Fig. 3.11 Pseudo-second-order adsorption kinetics of MB onto WO_3 SMRs at various initial concentrations: (a) $C_0 = 50$ μM, (b) $C_0 = 55$ μM, (c) $C_0 = 60$ μM, (d) $C_0 = 70$ μM. (e) $C_0 = 80$ μM, (f) $C_0 = 90$ μM, and (g) $C_0 = 100$ μM.

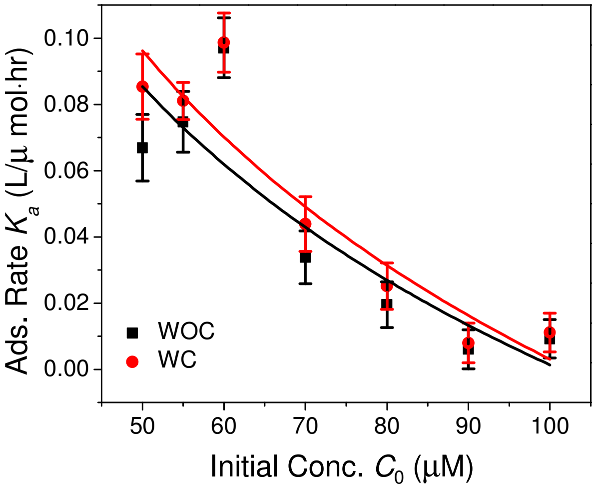

Fig.3.12 Adsorption constants K_a versus the MB concentration C_0 for WOC and WC cases. Symbols represent experimental data and the solid curves are a guide to eye. Error bars in the figure represent the estimated errors in data fittings.

Table 3.3. Adsorption kinetics parameter for the adsorption of MB onto WO_3 microrods for different initial concentrations (C_0) for both the WO and WOC cases.

Initial parameter, C_0 (μM), and sample description	**1st order kinetics**		**2nd order kinetics**		
	K_1 (h^{-1})	**Adj. R^2**	**h (= $K_2 q_e^2$) (μmol $g^{-1}h^{-1}$)**	**K_2 (g $\mu mol^{-1}.h^{-1}$)**	**Adj. R^2**
50 -WOC	5.23	0.921	4425	0.016	0.971
50 -WC	5.61	0.915	5193	0.020	0.980
55 -WOC	8.02	0.944	4969	0.016	0.985
55 -WC	6.25	0.962	5567	0.017	0.990
60 -WOC	4.69	0.976	5262	0.018	0.999
60 -WC	4.21	0.965	5463	0.018	0.998
70 -WOC	3.40	0.960	2819	0.006	0.999
70 -WC	3.47	0.965	3580	0.007	0.998
80 -WOC	3.46	0.944	2216	0.003	0.980
80 -WC	3.34	0.959	2780	0.004	0.994
90 -WOC	3.63	0.985	1313	0.001	0.979
90 -WC	2.96	0.986	1551	0.001	0.982
100 -WOC	2.46	0.980	1571	0.001	0.967
100 -WC	2.46	0.997	1838	0.002	0.994

3.5 Photocatalytic Activity of WO_3 SMRs

Fig. 3.13(a) shows the concentration profile of MB solution (C_0 = 50 μM) recorded with and without the UV-irradiation during adsorption experiment. These experiments were performed under the same conditions as without centrifuging (WOC). An UV lamp (λ = 365 nm, UV; BLAK-RAY, Model B 100AP) was used for illumination. The incident UV light intensity on sample was kept constant (=10 mW/cm^2), and was measured by an optical power meter (Thorlabs PM100D/S310C). In-situ absorbance measurements system was used as shown in Chap. 2 for recording the absorbance in a time acquisition mode. The change in the intensity of the MB absorbance peak at λ_{max} = 664 nm was converted into concentration profile for each measurement. Reduction rate of MB concentration under light illumination (with control dark) was observed to be faster noticeably especially after about 30 min (see Fig. 3.13(a)). This result confirmed the fact that as-deposited WO_3 SMR samples were photocatalytically active.[73] Thus, we further characterized all as-deposited and annealed WO_3 SMR samples for MB degradation activity, *i.e.* under the same ideal experimental conditions but using two different intensities of UV and visible light sources. Decay rates were calculated using the pseudo-first order rate equation (Eqn. (2.11b), from chap. 2. Fig. 3.13(b) shows the photocatalytic degradation kinetics of MB estimated from linear form of Eqn. (2.11)b. Comparison of MB removal % with as deposited and annealed WO_3 SMR samples *via* adsorption and photocatalytic degradation have been tabulated in Table 3.4. The MB degradation rates estimated for 7 hrs of irradiation have also included to compare their kinetics with different samples.

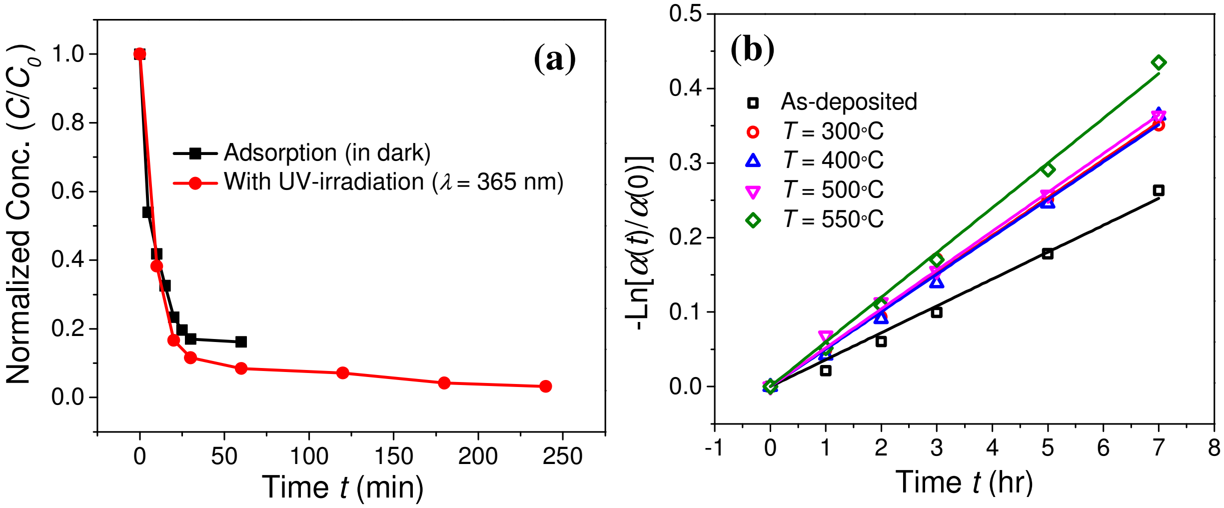

Fig.3.13 (a) Normalized concentrations of MB aqueous solutions due to dark adsorption and under the UV irradiation. The symbols are experimental data obtained from absorbance peak at λ_{max} = 664 nm and solid curves are a guide to eye, (b) kinematics of MB degradation, pseudo-first order fittings.

Table 3.4 MB removal comparison *via* adsorption and UV-induced photocatalytic degradation.

Samples	MB removal (%) *via* adsorption (and total time)	MB removal (%) *via* photocatalytic degradation/ k_c (hr^{-1}) (and total time)
As-deposited	74.6 (30 min)	23.14/ 0.036 ± 0.002 (7 hours)
T = 300 °C	60.0 (60 min)	29.57/ 0.050 ± 0.002 (7 hours)
T = 400 °C	14.7 (60 min)	30.51/ 0.052 ± 0.001 (7 hours)
T = 500 °C	10.5 (60 min)	30.44/ 0.054 ± 0.001 (7 hours)
T = 550 °C	11.4 (60 min)	35.25/ 0.063 ± 0.002 (7 hours)

3.6 Conclusions

In conclusion, we have demonstrated that the GLAD prepared amorphous WO_3 SMRs exhibit superior adsorption capability for MB. The adsorption kinetic studies show that the removal of MB from aqueous solution is a rapid process and adsorption rate strongly depends on the initial MB concentrations. The high adsorption of MB on amorphous WO_3 is associated with the combined effects of a large surface area and strong electrostatic interaction between cationic MB molecules and negative surface charge of WO_3 SMRs. The high adsorption capability along with the capability to break down toxic dyes into safe by-products, i.e. through the photocatalytic action under UV-irradiation, makes these WO_3 nanostructures promising candidates in the quest to remediate industrial pollution. However, for practical applications, besides the need of large quantities of the WO_3 SMRs, other environmental factors such as inorganic electrolytes and dissolved metal ions could affect the adsorption capability of WO3, and need to be studied extensively.

CHAPTER 4

Cu_xO (x=1, 2) NANOSTRUCTURES AND THEIR PHOTOCATALYTIC ACTIVTY

4.1 Introduction

As discussed in chap. 1, one approach to achieve VLAPs is to select low E_g materials. Among many other low bandgap single materials, shown in Fig. 1.4 (chap.1), copper oxides (Cu_xO; x = 1,2) hold the great promise due to their unique optical and charge transport properties.[30, 106-108] Both CuO and Cu_2O are P-type semiconductors, have a bandgap in the range from 1.7 to 2.6 eV, and are suitable for visible light absorption.[106, 109-111] Particularly, Cu_2O is more attractive since its conduction band is marginally above the water reduction potential (0 V *vs* NHE); and its bandgap is about 2.0 – 2.2 eV, which is larger than the water oxidation potential, 1.23 eV (see Fig 1.4).[27, 112] Thus, single or mixed phases of Cu_2O and CuO nanostructures have been studied extensively for solar energy conversion,[28] antimicrobial applications,[29] gas-sensing,[113] lithium-ion battery,[30] solar-water splitting,[107, 114] and so on. Among these applications, the use of Cu_2O nanostructure as a photocathode is very promising due to favorable energy band positions, with the CB lying at more negative below the H_2 evolution potential and the VB lying just positive above the O_2 evolution potential.[5, 115] However, according to the limited number of reports available for PEC properties of Cu_xO nanostructures, the stability of Cu_xO nanostructures could be a potential problem. This is because the redox potential for the Cu_2O reduction exists within its bandgap, and theoretically Cu_2O can be easily reduced to Cu by photoexcited electrons, which causes photo-reduction/corrosion (Cu^{2+}/Cu^{1+}; +0.16 V).[5, 28-30] Hara *et. al.*, in the year 1998, reported a lengthy water splitting test without any external bias potential on Cu_2O powders under solar irradiation and observed no noticeable activity loss for 1900 hours of experiments.[28] A year later, Jongh *et. al*. published a paper questioning the stability of Cu_2O nanostructure for photoelectrochemical (PEC) splitting of water *via* normal photocatalytic reaction.[116] Since then, several papers have been published showing controversial results on the photocatalytic stability of Cu_2O.[53, 54, 57, 115] In addition, Paracchino *et. al.*, and Zhang *et. al.*, have independently studied the stability of Cu_2O with and without the protecting layers of Al/ZnO/TiO_2 and CuO.[5, 57] Their results have shown that photocatalytic stability of Cu_2O nanostructures with the coatings has been enhanced. More importantly, Zhang *et. al.* has interpreted the enhanced stability due to the crystallographic orientation of Cu_2O along (111) plane.[29] The exact reason for these controversial observations is not clear yet. Recently, based on their calculation, Bendavid and Carter suggest that the stability of Cu_2O nanostructures are closely related to their crystallographic orientations,[117] which implies that the Cu_xO fabrication technique may play a dominant role.

In this Chapter, we take the advantage of OAD technique to prepare the Cu_xO NR array. The samples preparation strategy is to first deposit the porous Cu NRs using the OAD technique, then to oxidize the as-prepared Cu NRs in the ambient condition for a predetermined time at a given temperature. Depending on the oxidation temperature, one can obtain the single phase Cu_2O, and CuO, or the mixed phase Cu_2O/CuO NRs. The visible light induced photocatalytic activities of these Cu_xO NRs are investigated for degradations of both the cationic (methylene blue; MB) and anionic (methyl orange; MO) dyes. The PEC properties and stability of the Cu_xO NR samples are strongly dependent on applied bias potentials. All the nanostructures are stable for photodacay test and PEC measurements but the CuO NR sample is relatively more stable under the visible light illumination and at a negative bias potential.

4.2 Experimental Methods

4.2.1 Fabrication

Ti pallets (99.995%) and Cu shot (99.9+%) were used as source materials and were used as received. Both Ti adhesion layer, of 20 nm thick QCM reading and Cu OAD NR arrays of 2 μm were deposited onto the glass, Si and indium tin oxide (ITO) coated glass slides following the same protocol mentioned in chap. 3. Note that ITO substrates were cleaned with the Si substrates using the same piranha solution as described in previous Chapter. Ti adhesion layer was deposited at $\theta = 0°$ and Cu NRs were deposited at $\theta = 86°$. For both Ti and Cu depositions, the deposition rates were maintained at 0.4 nm/s. The as-deposited Cu NR samples were then oxidized in a quartz tube furnace at preset temperatures of 150, 190, 210, 240, 290, 340 and 380°C, respectively, in an ambient condition or under oxygen (O_2) flow (20 sccm) to obtain different phases of Cu_xO NRs. During all the treatments, the temperature was ramped at a rate of 5°C/min and the samples were maintained at the final temperature for 3 hours.

4.2.2 Characterization

The morphology and composition of the Cu and Cu_xO NR samples were examined by SEM and EDX analysis as described in section 2.1 (chap. 2). The crystal structure of the samples were characterized by the XRD data recorded with fixed incidence angle of 0.5°. The XRD measurement conditions were the same as described in chap. 3. XRD patterns were used to determine the crystal phase(s), their average crystallite size(s) and the relative mass percentage of Cu_2O/CuO of the samples oxidized at different temperatures. The optical transmittance of the samples were measured by the JASCO V-570 (as described in previous Chapter) over a wavelength range from 350 to 850 nm. While the reflectance of the samples were measured at normal incidence using home built spectrometer system described in section 2.2.

Photocatalytic activities of the Cu_xO NR samples were evaluated by the degradation of MB and Meth.O aqueous solutions under visible light irradiation at room temperature (25 ± 2 °C). The same experimental setup shown in section 2.3 was used for all dye degradation experiments. The starting concentrations of the dyes were chosen to be 31.3 μM for MB and 30.5 μM for Meth.O, and their respective pH values were 6.4 (± 0.2) and 5.7 (± 0.2). Prior to light irradiation, each sample in the dye solution was remained in dark for 30-60 mins for adsorption/desorption equilibrium. The visible light source was used with maintaining the constant intensity 65 mW/cm^2 reaching onto the sample's surface. The photodegradation kinetics of the MB and Meth.O were measured by examining their time dependent characteristic optical absorption peaks, at $\lambda = 664$ nm for MB and $\lambda = 465$ nm for Meth.O.[11, 72] The time dependent absorption data are fit by using the same method described in previous Chapter in order to obtain the decay constant κ_c.

PEC measurements were performed using the same experimental setup as shown in section 2.4. The Cu_xO NR samples deposited on ITO substrates were placed inside the PEC cell, with the deposited NRs facing directly towards illuminating light through the quartz window. The exposure areas of the Cu_xO NR samples (called WE) were of 1 cm × 1 cm. The RE and CE were also the same as described in chap. 2. The electrolyte, 0.5 M sodium sulfate (Na_2SO_4) solution, was aerated by N_2 for an hour; the initial pH value of the electrolyte was 6.9 ± 0.2. The cyclic voltammetry (CV) of the samples were measured in dark at room temperature (25 ± 2 °C), while the photoresponse and IPCE measurements were performed with a solar simulator and a monochromatic light. The illumination area of the monochromator beam, onto the Cu_xO NR samples, was 0.6 cm × 0.4 cm while area of collimated beam from solar simulator was about 1 cm × 1 cm. The incident intensity of the solar simulator, at the quartz window of the PEC cell, was adjusted to be 100 mW/cm^2 (1 sun equivalent). And the IPCE measurements were performed from 350 nm to 750 nm at every 10 nm interval. The resolution of the monochromatic source light was adjusted to 2.5 nm. All the PEC measurements were performed under the bias potential -0.5 V (*vs* Ag/AgCl). Note that the value of bias potentials, V (*vs* Ag/AgCl) is not the same as reversible Hydrogen electrode (RHE) or normal Hydrogen electrode (NHE) potentials, but they can be converted according to[56] $V(\text{RHE or NHE}) = V_{\text{Ag/AgCl}} + 0.197\ \text{V} + \text{pH}\ (0.059\ \text{V})$. Therefore, all the potential values listed below are V versus $V_{\text{Ag/AgCl}}$, unless otherwise stated.

4.3 Morphology and Structure

Fig. 4.1(a) shows the representative top and cross-sectional view SEM images of as-deposited Cu NR samples. Morphology related parameters such as the direction of vapor incident angle θ, NR tilting angle β, NR vertical thickness h, and NR diameter D are also defined in Fig. 4.1(a). Fig. 4.1(a) reveals that the as-prepared Cu nanostructure consist of well-aligned and tilted NRs. From the top-view SEM image, the NR density η is estimated to be $\eta = 50 \pm 10$ rods/ μm^2. These NRs are straight and exhibit relative smooth side surface, which is consistent with the result reported by Li. *et. al.*[71] The cross-sectional image in Fig.

4.1(a) shows that the Cu NRs are of nearly cylindrical shape with increasing diameter towards the top. The average width (or diameter) of the NRs near the top is $D = 40 \pm 10$ nm. To make a consistent comparison, we measured the diameters of both the Cu and Cu_xO NRs at about 100 nm below the top surface. Those Cu NRs are tilting away from the substrate normal at $\beta = 70 \pm 5°$ and $h = 350 \pm 20$ nm. The measured value of β does not match with the angle predicted by both the tangent rule,[65] $\beta = \arctan(1/2 \tan \theta) = 82°$; and cosine rule,[66] $\beta = \theta - \arcsin(1\text{-}\cos(\theta/2)) = 58°$, for OAD. However, the material dependent models described in the literature can be used to explain the resulting β angle.[118, 119] Fig. 4.1(b) to (d) show the representative SEM images for Cu_xO NR samples obtained at oxidation temperature T = 150, 240, and 380°C, respectively. Compared to Fig. 1(a), the changes in morphology of Cu_xO NR samples are obvious; visually one can see that the NR diameter becomes larger after oxidation, which is expected. Other morphological parameters, such as h, β, and η are also changed, and the results are summarized in Table 4.1. The increase in diameter could be interpreted as oxidation and coarsening of NRs with increasing oxidation temperature. As a result, the NR density is found to be decreased with T. Regardless of the oxidation temperatures, the β values are observed to be almost unchanged.

The crystal structures of Cu_xO NRs are characterized by XRD. Fig. 4.2(a) shows the XRD patterns of Cu_xO NR samples oxidized at different temperatures. XRD spectrum of the as-deposited Cu NRs (Fig. 4.2(a)) is also included as a reference, and the result shows that those samples are polycrystalline Cu with no detectable impurities (as compared with JCPDS Ref. No. 085-1326). All the diffraction peaks of the sample oxidized at T =

150 °C, namely at $2\theta = 29.58°, 36.44°, 42.33°, 61.41°$, and $73.56°$, are consistent with the diffraction patterns of Cu_2O (JCPDS Ref. No. 078-2076), representing the Cu_2O crystal

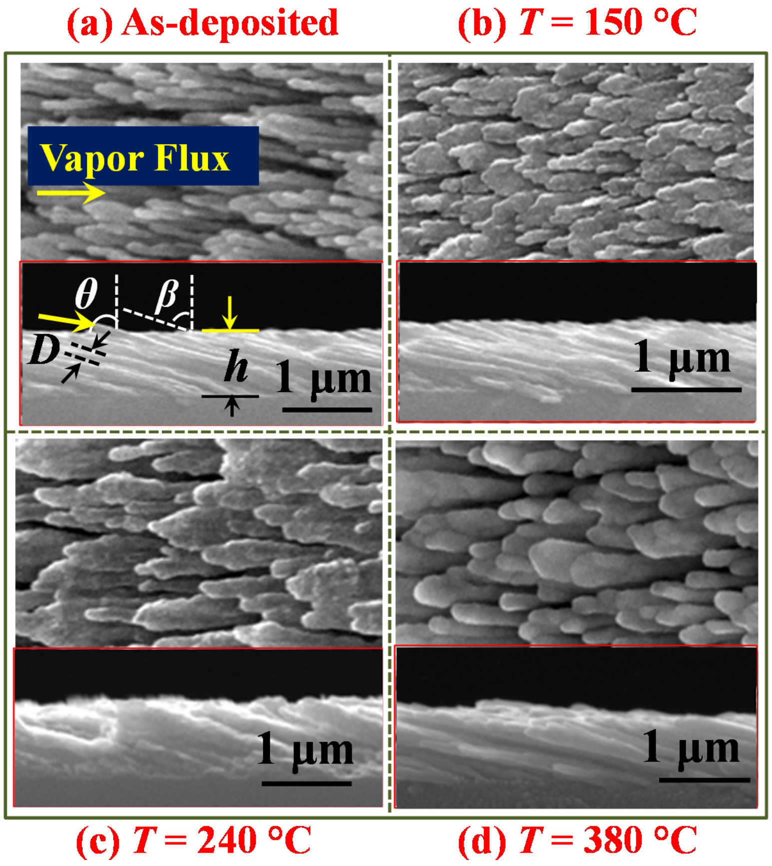

Fig. 4.1. Morphology of as-deposited Cu and thermally oxidized Cu_xO NRs samples: representing top-view of (a) as-deposited Cu NRs, (b) Cu_2O NRs, oxidized at T = 150°C, (c) Cu_xO NRs (mixed-phase of both Cu_2O & CuO), oxidized at T = 240°C, and (d) represent the CuO NRs, oxidized at T = 380°C. Figure insets represent their respective cross-sectional views. Note that the samples oxidized at other temperatures (not included here) cannot be distinguished with their sequential orders to represent the morphology change, by visual inspection.

Table 4.1 summary of SEM images analysis for morphology of Cu and Cu_xO NRs.

Phase	**As-deposited** **Cu**	**T_a= 150°C** **Cu_2O**	**T_a= 240°C** **Cu_xO (mixed)**	**T_a= 380°C** **CuO**
NR Tilting angle, β (°)	70 ± 5	70 ± 5	70 ± 5	74 ± 5
NR Thickness, *h* (nm)	350 ± 20	340 ± 20	340 ± 20	320 ± 20
Density, η (#/μm^2)	50 ± 10	45 ± 10	45 ± 10	40 ± 10
NR diameter, *D* (nm)	40 ± 10	50 ±10	60 ± 10	70 ± 10

planes of (110), (111), (200), (220), and (311), respectively. While the sample oxidized at T = 380 °C is composed of pure single phase CuO (JCPDS No. 048-1548) as confirmed by the peaks at 2θ = 32.51°, 35.42°, 35.54°, 38.71°, 38.90°, 48.72°, 53.49°, 58.26°, 61.53°, 65.81°, 66.22°, 67.90°, 68.12°, 72.37°, 74.98°, and 75.24°, which represent the (110), (002), $(11\bar{1})$, (111), (200), $(20\bar{2})$, (020), (202), $(11\bar{3})$, (022), $(31\bar{1})$, (113), (220), (311), (004) and $(22\bar{2})$ crystal planes of CuO. Nevertheless, all the samples oxidized in the temperature range, 150 °C < T < 380 °C, indicate the presence of a mixture of Cu_2O and CuO phases, which is consistent with the thin film results reported in literature.[108, 109]

The phase evolution and nanocrystal growth of Cu_2O and CuO NRs can be further understood through detailed XRD analysis. First, the average crystalline sizes can be estimated using the most prominent peaks of Cu_2O (111), CuO (111), and CuO $(11\bar{1})$ planes by the Debye-Scherrer'r equations, $d = K\lambda / \beta' \cos\theta$, where d is the diameter of the crystalline grain, K = 0.9, λ (Cu-Kα1) = 1.5405980 Å, and β' is the full width at half maximum of the selected diffraction peak. Results of crystallite sizes are summarized in -

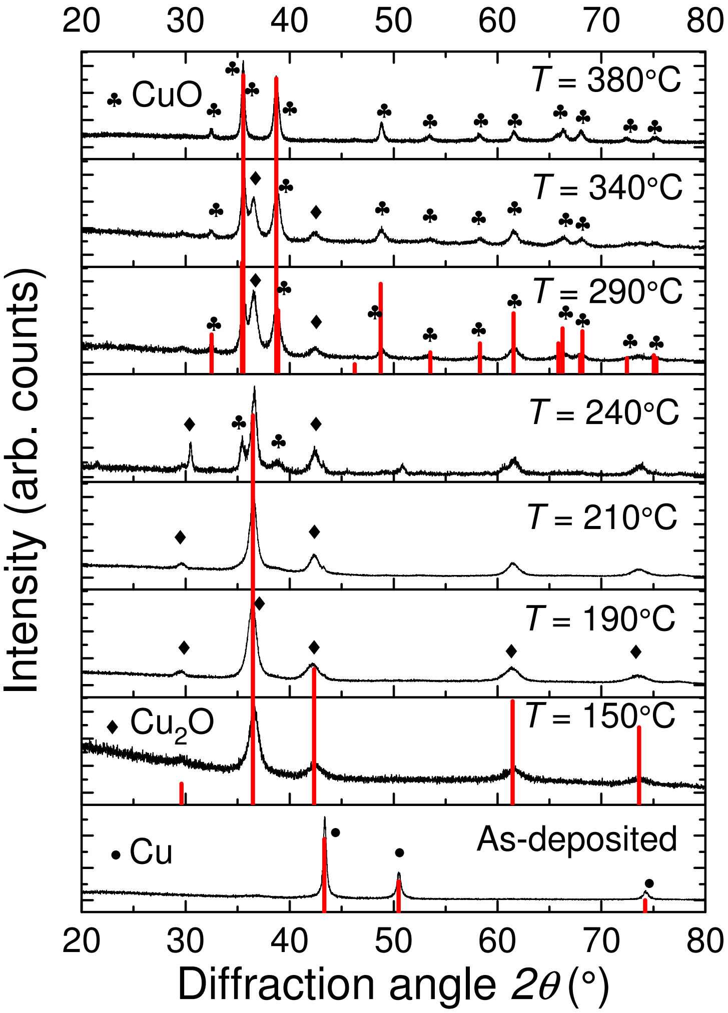

Fig. 4.2(a) Comparison of XRD spectra of as-deposited Cu and annealed Cu_xO NR samples.

Table 4.2. Overall, the Cu_2O crystalline size decreases with T while the CuO crystalline size increases with T (with an exception for the sample annealed at T = 240 °C). This deviation could be attributed to the peak broadening due to the phase change from Cu_2O to CuO, *i.e.*, changing the XRD peak position from $2\theta = 36.44°$ of Cu_2O to 35.42° and 35.54° of CuO (see Fig. 2(a)). Besides, a general trend of increasing the crystallite size of CuO at

higher T is in good agreement with the observed NR coarsening.[114] In addition, the XRD data can also be used to roughly estimate the Cu_2O/CuO composition ratio through a semi-quantitative analysis utilizing the Rietveld program using the FullProf software as described in the literature.[120, 121] Fig. 2(b) shows the relative percentage of Cu_2O/CuO for different oxidation temperatures. The Cu_2O percentage in the Cu_xO NR samples oxidized at T = 150, 190, 210°C, 240, 290, 340, and 380°C is estimated to be 100%, 96%, 92.5%, 53%, 21.6%, 9.2%, and 0%, respectively. This results can also be confirmed by using ratios of the most prominent peaks of Cu_2O (111) and CuO (111), as described in the literature.[109, 122] The estimated results is shown by a blue line in Fig. 2(b).

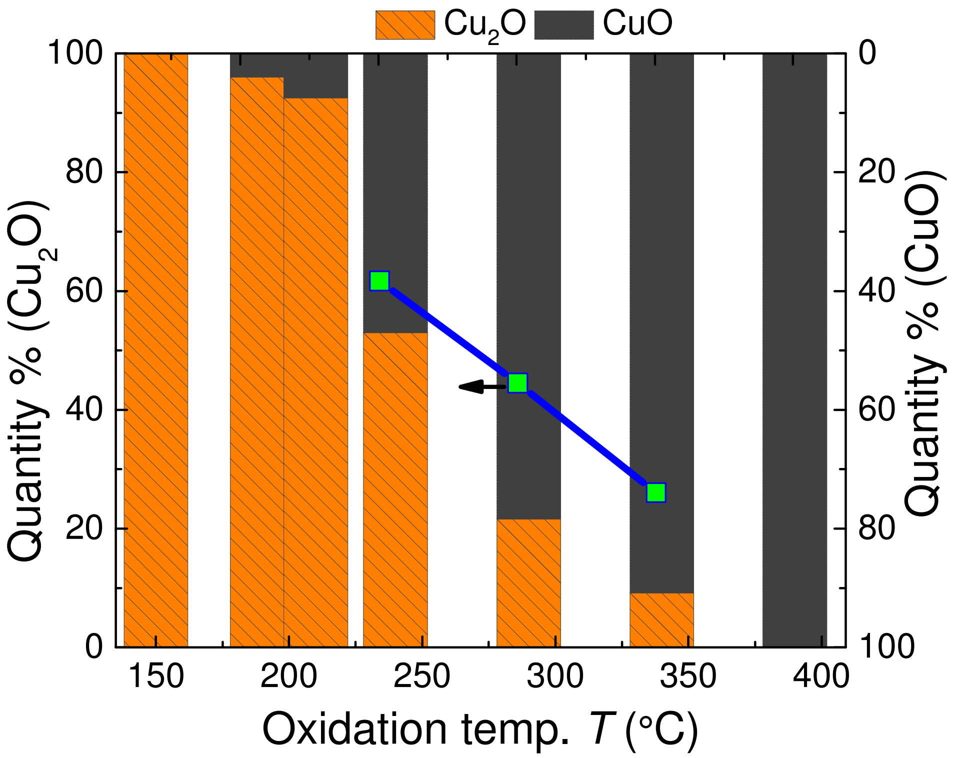

Fig. 4.2(b) Showing a change in the content of Cu_2O and CuO in the Cu_xO NR samples, as a function of oxidizing temperature.

Table 4.2 Structural and optical parameters of Cu_xO NR samples.

Sample	Structural parameters		Optical parameters	
	Grain size (nm) at (111) in Cu_xO phase	**Grain size (nm) at (11-1) in Cu_xO phase**	**Direct bandgap**	**Indirect bandgap**
T = 150 °C	30.4 (in Cu_2O)	--	2.54	2.02
T = 190 °C	31.2 (in Cu_2O)	--	2.51	2.04
T = 210 °C	21.3 (in Cu_2O)	--	2.50	2.06
T = 240 °C	16.5 (in Cu_2O)	--	2.50	1.94
T = 290 °C	35.6 (in CuO)	21.3 (in CuO)	2.45	2.16
T = 340 °C	35.6 (in CuO)	39.5 (in CuO)	2.24	--
T = 380 °C	42.8 (in CuO)	84.8 (in CuO)	2.13	--

4.4 Optical Properties

The appearance of an as-deposited Cu NR sample and some representative oxidized Cu_xO NR samples are shown in inserts of Fig. 4.3(a). The Cu NR sample is optically opaque and highly reflective by visual inspection. After oxidation, the Cu_xO NR samples appear to be pale yellowish in color at lower oxidizing temperatures (≤ 240 °C) and then change slowly into darker reddish black with increasing T (240 °C $\geq T \leq$ 380 °C). This shows that the visible light absorption of the sample is increased at higher T values. To determine the best estimation for optical absorbance spectra, $A(\lambda)$ of the Cu_xO NR samples, both the transmittance (%T') and reflectance (%R) spectra are accounted in the calculation as described in section 2.2. Representative transmittance and reflectance spectra of the Cu_xO NR samples are shown in Fig. 4.3(a) and Fig.4.3 (b) respectively; and the estimated

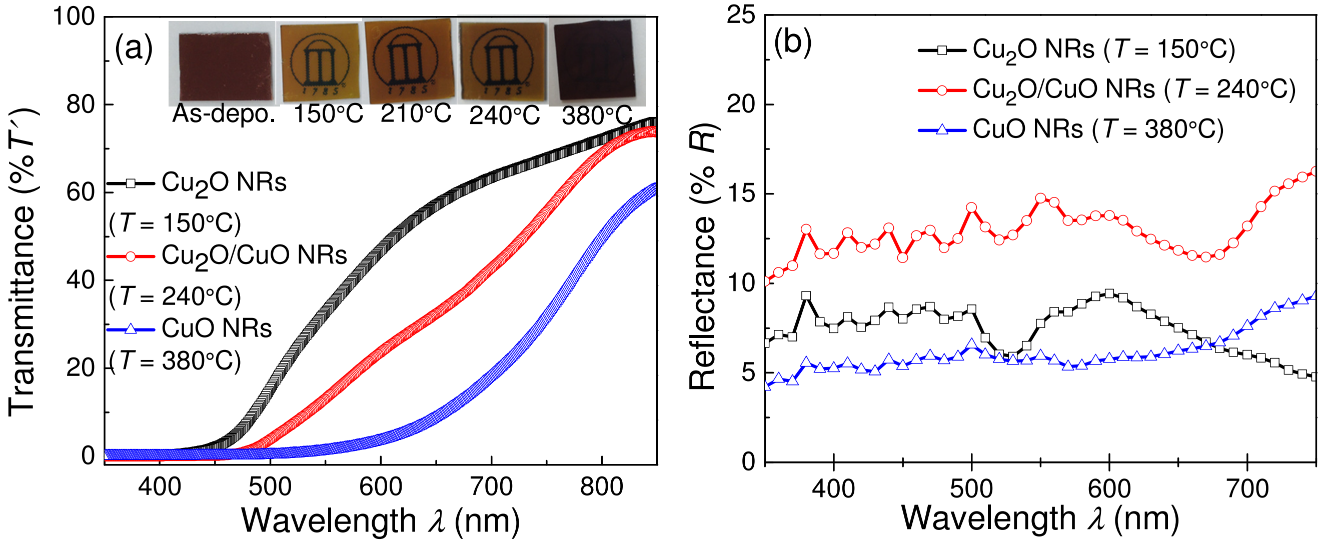

Fig. 4.3 (a) Transmittance (%T′) and (b) Reflectance (%R) of some selected Cu_xO NR samples. Insets in (a) show the digital photographs of Cu_xO NR samples oxidized at different T, placed over the Univ. of Georgia logo.

UV-Vis absorbance spectra of these samples are shown in Fig. 4.4(a). The absorption edges of the oxidized samples are red-shifted with increasing *T* (with an exception for the sample oxidized at *T* = 190 °C). This general trend can be attributed to the crystal phase change, as confirmed by the XRD results. The optical bandgaps of those Cu_xO NR samples are estimated using the Tauc plots (defined in section 2.2).[10, 107] As reported by the literature, Cu_xO could exhibit both direct and indirect bandgaps behaviors.[107, 108] Therefore, Tauc's plots are obtained for both the direct and indirect allowed transitions. Fig. 4.4(b) shows an example of the Tauc's plots for Cu_2O NR sample at *T* = 150 °C. The direct and indirect bandgaps of Cu_2O NRs are determined to be E_g^D = 2.54 and E_g^I = 2.02 eV, respectively. The Tauc's plots for all other Cu_xO NR samples are shown in Fig. 4.5(a) - (b); and the resulting bandgap values are summarized in Table 4.2. Results show that the single phase Cu_2O and the mixed phase Cu_2O/CuO samples exhibit both the direct and indirect bandgaps while the single phase CuO NR samples only exhibit a direct transition (see Fig. 4.5(b)). The direct bandgap of the single phase CuO NRs is 2.13 eV. Similar -

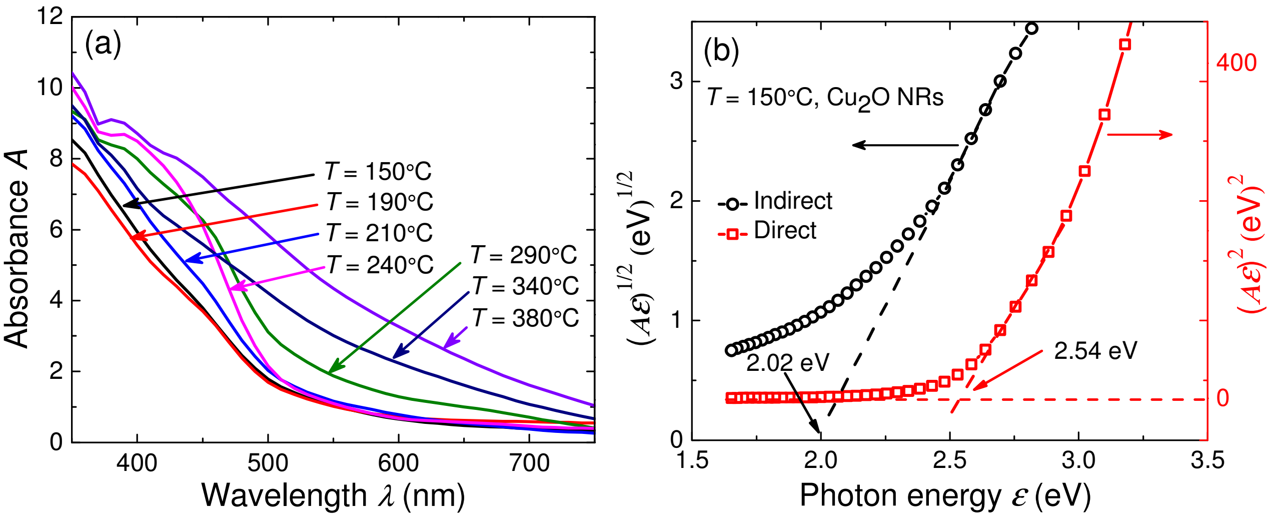

Fig. 4.4. (a) Absorption spectra of Cu_xO NR samples, and (b) the representative Tauc's plot showing a direct and an indirect bandgap for Cu_2O NR sample.

phenomenon for the Cu_2O and CuO films have been reported by Heinemann *et. al.*, and Zoolfakar *et. al.*[107, 108] The estimated direct bandgap values of Cu_2O NRs (E_g^D = 2.54 eV) are in good agreement with the results reported for Cu_2O thin films which are in the range of E_g = 2.1-2.6 eV.[31, 108, 123] However, the estimated values for indirect bandgaps of our

Cu_2O NR samples are slightly lower than those reported in the literature (2.1 -2.21 eV).[107, 108, 124] These observed lower values could be due to various reasons, such as heat treatment (during oxidation), change or restriction in grain sizes during crystal phase change occurred, composition of mixed phases, etc., as reported by Zoolfakar *et al.*[107]

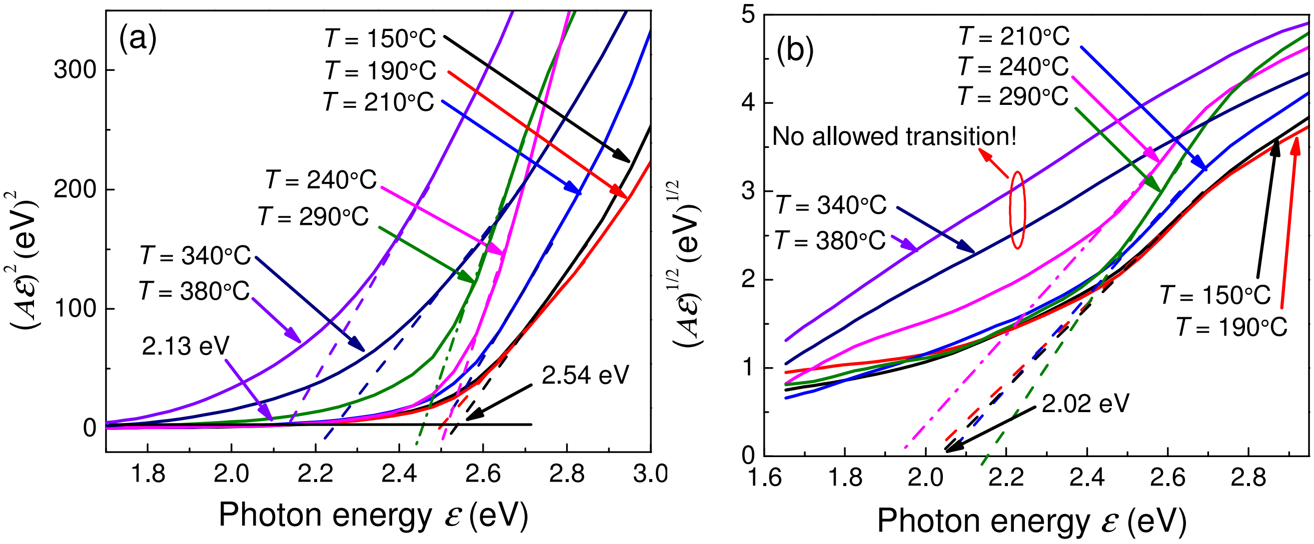

Fig. 4.5 Tauc's plot for direct (a) and indirect (b) bandgap calculation for Cu_xO NR samples.

4.5 Photocatalytic Activity of Cu_xO NRs

The PDD of both the MB and Meth.O aqueous solutions are tested to characterize the catalytic activity of Cu_xO NR samples under visible light irradiation. The reason for choosing both the MB and Meth.O dyes is to investigate the effect of the dye adsorption property on different Cu_xO samples since different dyes have different molecular weights, sizes and charges, and could exhibit different intake capacity for different Cu_xO NR samples *via* dark adsorption. Two control experiments are performed. First experiment is to monitor the dark adsorption of dyes onto the Cu_xO NRs by keeping the dyes in dark with Cu_xO samples for 30 to 60 mins. No significant dark adsorption of both the dyes are observed with all the Cu_xO NR samples. Second is to investigate the direct photodecay of the dyes by irradiating the light to the dye solutions without the Cu_xO NR samples. We observed a slow decrease in absorption spectra of MB solution but no change for Meth.O solution as shown in Fig. 4.6(a)-(b). The decay rate constant for MB is estimated to be k_{light}^{MB} = 0.003 ± 0.001 hr^{-1}. This result suggests that there is a self- degradation of MB under visible light irradiation. The plots of MB and Meth.O absorption peak versus illumination time are shown in Fig. 4.7(a)-(b). The photocatalytic decay rates, κ_c value extracted from these plots as a function of T can be seen in Fig. 4.8. We observed two trends: first, the photodecay rates for both MB and Meth.O follow the same trend with respect to T; second, the MB degradation rates are relatively higher than those of the Meth.O degradation rates.

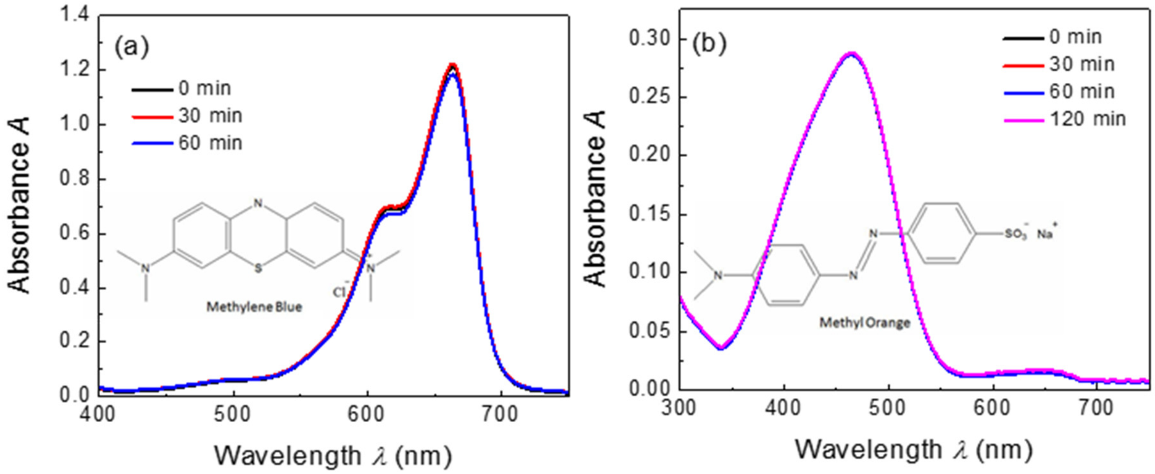

Fig. 4.6 comparison of self-degradation of MB (a) and Meth.O *(b) dyes under the visible light irradiation (without the Cu_xO NRs samples). Fig. insets (a) and (b) respectively represents the molecular structure of MB and* Meth.O.

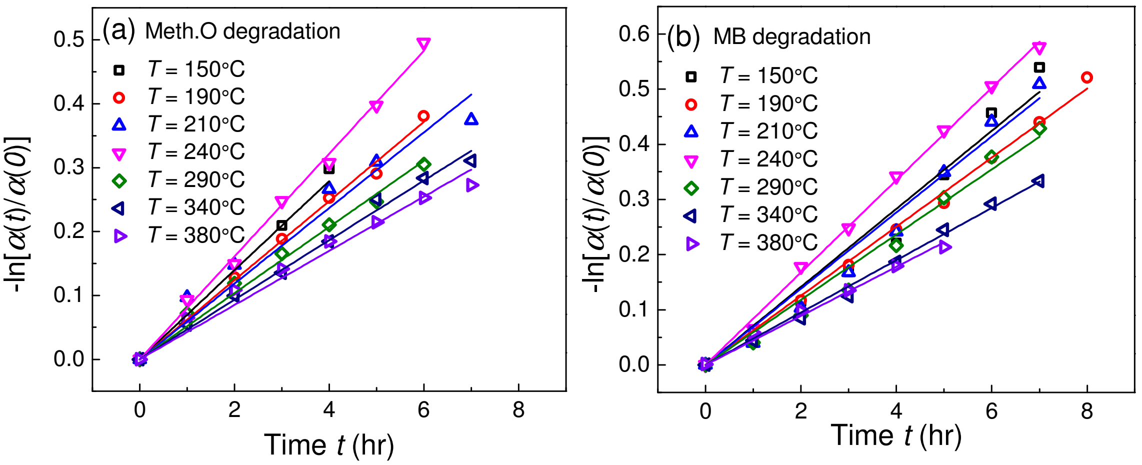

Fig. 4.7 Photocatalytic degradation kinetics of MB (a) and Meth.O (b) with different Cu_xO NR samples, under visible light irradiation.

The photodecay rates at T = 150 °C are quite larger, k_c^{MB} = 0.071 ± 0.003 hr^{-1}, $k_c^{Meth.O}$ = 0.070 ± 0.003 hr^{-1}. Then they decrease slightly, k_c^{MB} = 0.063 ± 0.001 hr^{-1}, $k_c^{Meth.O}$ = 0.062 ± 0.001 hr^{-1} at T = 190 °C. At T = 240 °C, these values reach the maximum, k_c^{MB} = 0.084 ± 0.001 hr^{-1}, $k_c^{Meth.O}$ = 0.080 ± 0.001 hr^{-1}. When T increases further, $k_c^{MB(Meth.O)}$ decreases monotonically with T and reaches the lowest values k_c^{MB} = 0.044 ± 0.001 hr^{-1}, $k_c^{Meth.O}$ = 0.042 ± 0.001 hr^{-1} at T = 380 °C. This trend follows the crystal structure and optical properties change of Cu_xO NRs. It is clear that under the same testing conditions, the single phase CuO NR samples give the lowest photocatalytic performance for both the cationic and anionic dyes while the single phase Cu_2O NR samples show relatively higher decay rates. However, it is interesting to note that the mixed phase Cu_2O/CuO NR samples obtained at T = 240 °C exhibited the highest photocatalytic activity. Since the experimental conditions for all the samples are the same, and all the samples have strong optical absorbance in the visible wavelength range as shown in Fig. 4.4(a), the difference in PDD activity may be -

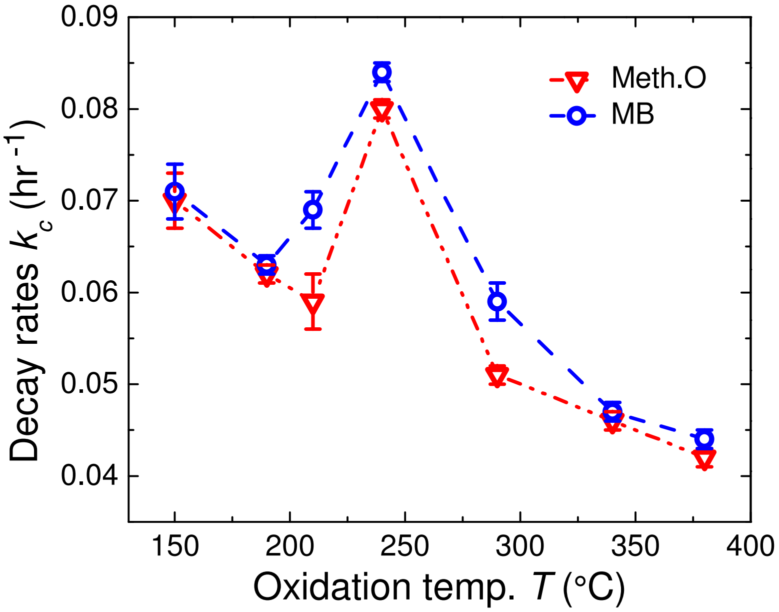

Fig. 4.8 Photocatalytic decay rates of Cu_xO samples against Meth.O and MB degradation under visible light irradiation. Symbols represent the experimental data points and the error bar denote the standard deviation (dash lines are guidelines to the eye).

due to two factors, the band edge location and charge separation of the Cu_xO NR samples. The band edges of semiconductors is one of the most important factors in determining the PDD activity. It is well known that the amount of ROS produced on the surface of photocatalyst determines the PDD activity.[125-127] The generation of ROS is strongly dependent on the amount of photogenerated CB electrons and VB holes, and more importantly on the redox potentials of a photocatalyt as shown in Figs. 4.9(a) and 4.9(b). The higher ROS generation rate can be expected if the CB edge is more negative and the VB edge more positive. Thus, the low degradation rate with the single phase CuO NR sample compared to that of single phase Cu_2O NR sample could be due to its CB edge lying in a position unfavorable for multiple electron transfer (see Fig. 4.9 (b)).[53, 128] For CuO sample, its CB edge is approximately located at +0.0 to 0.03 V (V *vs* NHE) while the required O_2 reduction potential is -0.28 V as shown in Fig. 4.9 (b).[16, 129] Therefore, the CB location could not provide a sufficient potential to reduce the molecular O_2 through electron transfer, $O_{2(ads)} + e^- \rightarrow O_2^{\bullet -}$.[16, 18] But its VB edge is located more positively than the H_2O oxidation potential (+1.23 eV), which can generate hydroxyl radical, $OH^-_{(ads)} + h^+ \rightarrow OH^\bullet_{(ads)}$, leading to generation of hydrogen peroxide, $2OH^\bullet \rightarrow H_2O_2$. Overall, this results a low efficiency in generating ROS. In contrast, the single phase Cu_2O samples have a more negative CB edge, reported to be located at -1.2 to -1.4 V (V *vs* NHE), and its VB edge located around +1.1 to +1.3 V (V *vs* NHE) (deduced from the bandgap), which is potentially for higher ROS generation rate.[18, 129] The superior PDD activity of

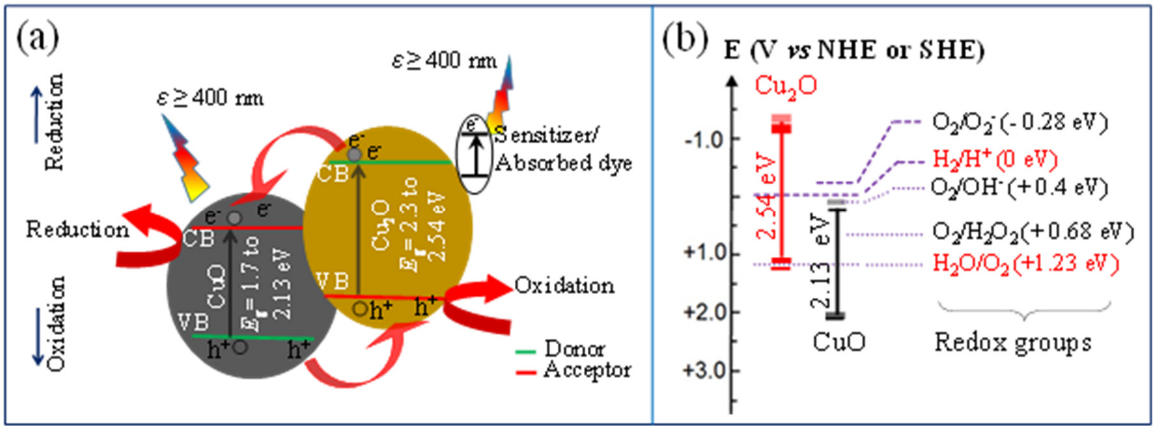

Fig. 4.9 The proposed mechanism for the enhancement of the photocatalytic activity for MB and Meth.O with the mixed phase Cu_2O/CuO NR samples. (a) Generation and transfer of charge carriers. Note that the electrons and holes transfer direction for Cu_2O/CuO composites are shown by red arrows, and (b) energy band edges of single phase Cu_2O and CuO NRs with redox couples in water.

mixed phase Cu_2O/CuO samples take the advantages of band edge locations of both the Cu_2O and CuO, which are assisted with the charge separation effect due to the energy band miss-alignment as shown in Fig. 4.9 (a) and 4.9 (b). As shown in Fig. 4.9 (a), a charge separation process could occur: The CB electrons of higher energy from Cu_2O can move to the CB of CuO (lower energy) while the VB holes from CuO could transfer to the VB of Cu_2O (energetically favorable). In these processes, the Cu_2O sample acts as an electron donor and hole acceptor while the opposite applies for CuO sample. Charge separation at the interface of the mixed phase Cu_2O/CuO samples is very advantageous in extending the life-time of photogenerated e^-- h^+ pairs, to avoid their recombination, which may result an enhanced PDD activity.[13, 130, 131] Similar mechanisms have described in the literature for heterojunction of metal oxides semiconductors.[62, 109, 114] These mechanisms are also evidence when considering the Cu_2O/CuO composition change as revealed by XRD (see Fig. 4.2(b)). There is approximately an equal amount of Cu_2O and CuO (53: 47 by wt.%) present at T = 240 °C samples, which results in the best photodecay rates since the charge separation effect is expected to be maximized. With increasing T, the Cu_2O to CuO composition ratio decreases, and more Cu_2O is turned into CuO, resulting in that the k_c value is approaching for single phase CuO.

In order to explain the difference in decay rates of MB and Meth.O, we need to consider the role of dyes played in the photodecay characterization. According to the literature, the overall photocatalytic activity observed are governed by two pathways, the direct semiconductor photoexcitation and indirect dye photosensitization.[47] The latter process of photosensitization (also called photo-assisted degradation) involves a two-step process: excitation of dye *via* visible light absorption and transfer/injection of excited electron(s) onto the CB of a photocatalyst as shown in Fig. 4.9(a).[49] For this process, the amount of light absorbed by individual dye determines the indirect photosensitization process and hence contribute for the total decay rate. It is expected that under the same conditions, the more light absorbed by a dye, the higher the photodecay rate. Therefore, we compare the absorbance spectra of the dye solutions, the Cu_xO NR samples, and the emission spectrum of the light source used for the photocatalytic experiments. As seen from the Fig. 4.10, the MB absorbs the light in the wavelength range of 550 to 700 nm (λ_{max} at 664 nm) while Meth.O absorbs light from 380 to 530 nm (λ_{max} at 465 nm). MB has a larger absorption band and the source light covers entire MB absorption spectra. As a consequence, more photoexcited electrons are expected to be injected into the CB of photocatalyst resulting in a higher MB degradation rate. As described above, the self-degradation of MB solution may also contribute to the higher decay rates.

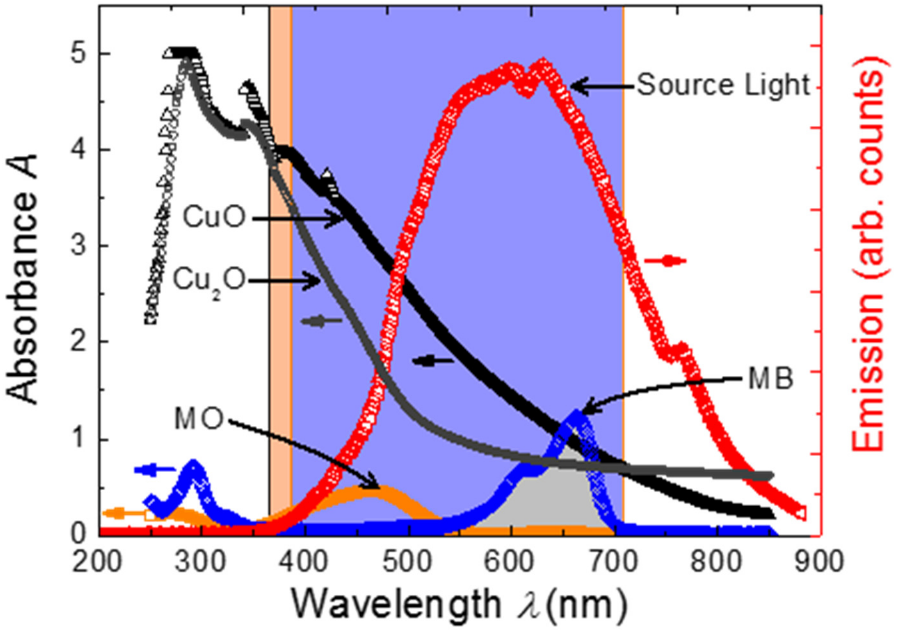

*Fig. 4.10. The comparison of the absorbance spectra of Cu_xO NR samples, and dye absorbance spectra (*Meth.O *& MB) as well as the emission spectrum of illuminating light.*

To confirm the stability of the Cu_xO NR samples in PDD reactions, MB and Meth.O degradation experiments are repeated for three successive cycles for each of the CuxO sample. Then both the decay rates and the XRD data after each test and with reference to the fresh sample, are used to compare their stability. Fig. 4.11 shows the representative results of MB degradation with Cu_2O NR sample, used for total 21 hrs of experiments. The photocatalytic activities are observed to remain about the same (less than 5% change in the total degradation), indicating that the prepared Cu_2O NR samples are stable in aqueous solution and under visible light irradiation. Similarly, other Cu_xO NR samples also retained their photocatalytic activity after multiple experiments. Fig. 4.12 shows a representative XRD spectra of some selected Cu_xO NR samples before and after the dye degradation -

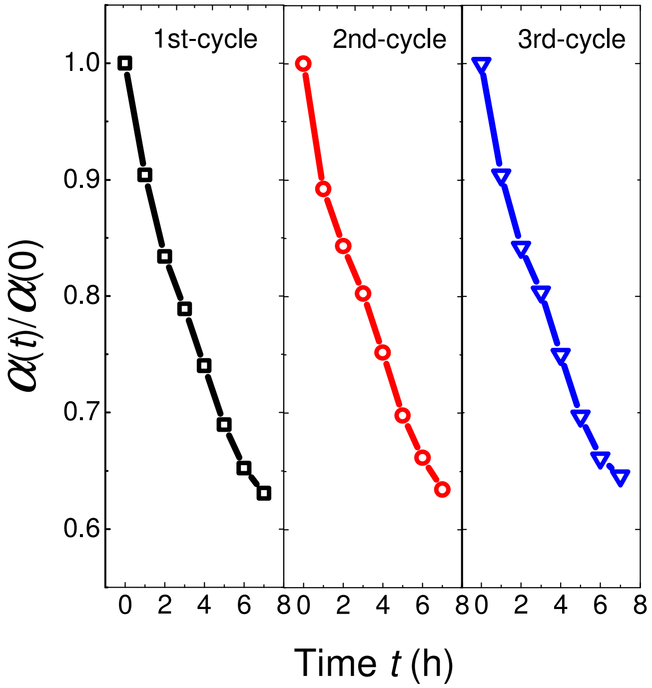

Fig. 4.11 The cycling test of Cu_2O NR sample for MB degradation under visible light irradiation.

experiments. No changes in the crystal structures are observed under the detection limit of XRD, indicating these Cu_xO NR samples are fairly stable during the photocatalytic reaction in aqueous solution. These results could be attributed to the dominated crystallographic orientation of Cu_2O, *i.e.* along the plane (111) as confirmed by the XRD (see Fig. 4.2(a)).[117] While the stability for mixed phase Cu_2O/CuO and the single phase CuO samples are in good agreement with the literature: single phase CuO is reported to be the most stable and it also improves the stability of Cu_2O by acting as a protecting layer.[53, 57]

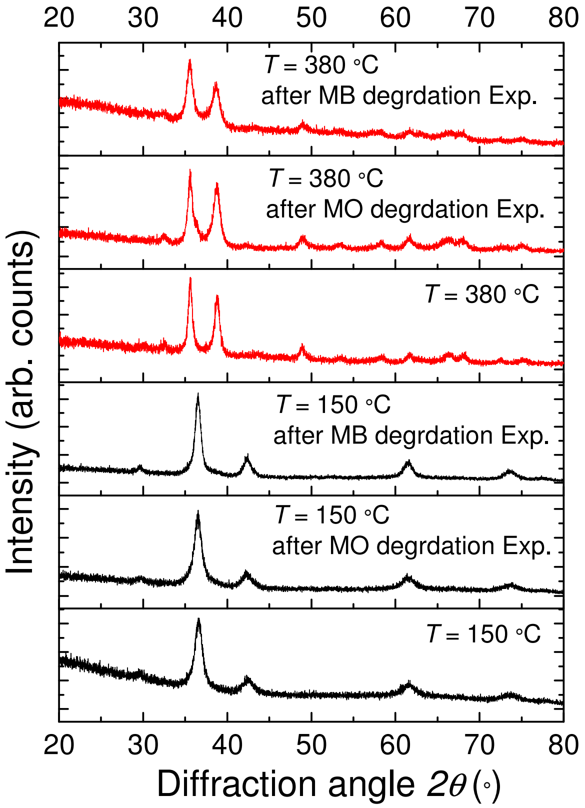

Fig. 4.12 XRD spectra of the selected Cu_xO NR samples recorded before and after the dyes degradation experiments. T = 150 °C represents the Cu_2O phase while T = 380 °C represents CuO.

4.6 Photoelectrochemical (PEC) properties of Cu_xO NRs

The CV, dynamic photoresponse, and IPCE measurements are performed to characterize the PEC properties of Cu_xO NR samples.[5, 58] Three representative samples, namely, a single phase Cu_2O NR sample (T = 150 °C), a mixed phase Cu_2O/CuO NR sample (T = 240 °C), and a single phase CuO NR sample (T = 380 °C), are characterized. Multi-cycle CV measurements are used to determine the redox potentials, and the stability of these samples, inside the electrolyte solution. Some of the selected cyclic voltammograms are shown in Fig. 4.13 (a) to (c). Three different scanning rates, 100 mV/s, 50 mV/s, and 10 mV/s, are chosen to confirm if any oxidative and reductive peaks are missing at the highest scan rate. Unless otherwise stated, here we show the cyclic voltammograms results from -0.6 to + 0.6 V obtained from a scan rate of 100 mV/s. As seen in Fig. 4.13 (a) to (c), over the entire potential range, both the cathodic and anodic peaks are observed for all three samples. The single phase Cu_2O and the mixed phase Cu_2O/CuO NR samples are observed to be relatively unstable for the first few minutes (Figs. 4.13 (a) & (b)), but stabilized in about 10 minutes while the CuO NR sample is observed to be the most stable one (see Fig. 4.13(c)). The cathodic and anodic peaks for Cu_2O NR sample are observed at the potentials V_c = -0.16 V, V_c = -0.42 V, and V_a = +0.52 V, which are consistent with the reported characteristic reduction and oxidation peaks of Cu_2O and CuO.[53] For the mixed phase Cu_2O/CuO NR sample, with the increased number of cycles, initially the observed V_a = +0.25V moves towards more positive values as shown in Fig. 4.13(b) while the V_a = +0.01V almost disappeared. The CV of CuO NR sample exhibits only one cathodic (V_c = -0.39 V) and one anodic (V_a = +0.25V) peaks (Fig. 4.13(c)). The observed variations in the voltammograms, for different samples, demonstrate that the stability of Cu$_x$O NRs are strongly phase dependent where the CuO NR sample exhibit the most stable phase. These results are in good agreement with the report by Zhang *et. al.*, who have reported an enhanced stability of Cu$_2$O nanostructures -

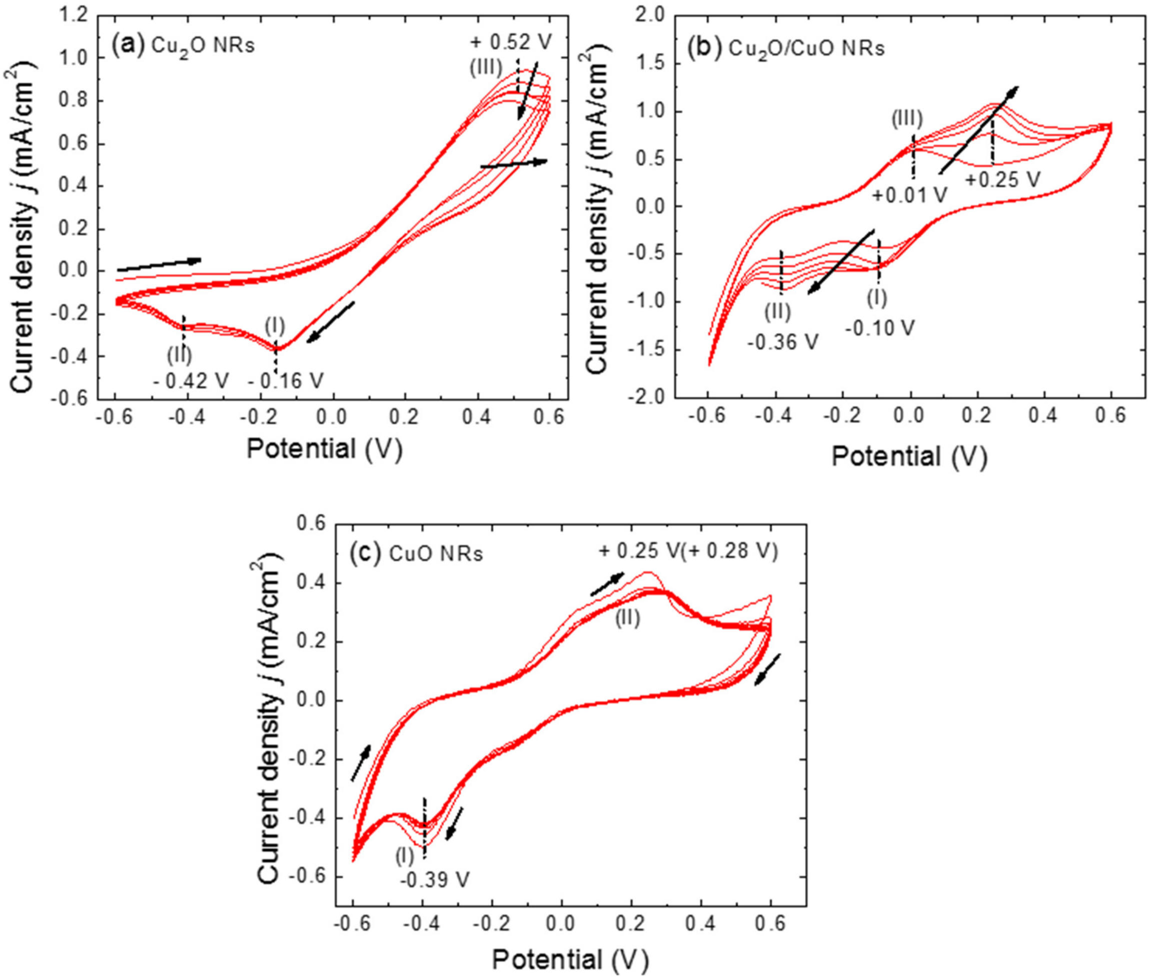

Fig. 4.13 The CV curves of selected Cu$_x$O NR samples: (a) Cu$_2$O (T = 150°C), 5 cycles; (b) Cu$_2$O/CuO (T = 240°C), 5 cycles; and (c) CuO (T = 380°C), 10 cycles.

by coating a protecting thin layer of CuO.[57] For Cu$_2$O NR sample, the maximum stable cathodic and anodic current density values are observed to be $J_c = 0.38$ mA/cm^2 and $J_a = 0.85$ mA/cm^2, respectively. Further, it is observed that the cathodic current density decreases beyond V_c = -0.16 V until it reach another plateau at V_c = -0.42 V where the cathodic current becomes stabilized to J_c = 0.31 mA/cm^2. For the mixed phase Cu_2O/CuOsample, the maximum cathodic and anodic current densities are J_c = 0.82 mA/cm^2 and J_a = 1.2 mA/cm^2, respectively. Beyond the cathodic peak, V_c = -0.36 V, for $V \leq$ -0.5 V, J_c is observed to increase almost linearly with the applied potential. The maximum stable cathodic and anodic current densities for single phase CuO NR sample are J_c = 0.5 mA/cm^2 and J_a = 0.35 mA/cm^2. The J_c - V_c also shows a linear relationship for $V \leq$ -0.5 V. This linear behavior for the both single phase Cu_2O and mixed phase Cu_2O/CuO samples could be attributed to the increased reduction while the absence in Cu_2O NR sample could be due to the diffusion control current.[132, 133]

Fig.4.14(a) shows the dynamic photocurrent generation curves, the photocurrent density J_{ph} versus time t, for three samples tested in 0.5 M Na_2SO_4 at a bias potential of V_c = -0.5 V and under the illumination of AM 1.5G. The chopping frequency is 0.033 Hz. The observed photo-induced cathodic currents demonstrate the p-type semiconductor nature of these samples.[54, 132] For all the three samples the J_{ph} - t curves show that the initial J_{phs} are large, and then decrease with chopping times, which is consistent with the results from most of the PEC measurements. The observed J_{ph} will eventually stabilized after multiple times. Note that the J_{ph} decay for single phase Cu_2O sample and the mixed phase Cu_2O/CuO sample takes longer time, while for the single phase CuO sample, J_{ph} reaches a stable value almost after one chopping. In addition, the single phase Cu_2O sample show the lowest stable J_{ph} = 0.06 mA/cm^2 while the Cu_2O/CuO sample demonstrates the highest J_{ph} (= 0.24 mA/cm^2). The CuO sample has moderate J_{ph} = 0.18 mA/cm^2. This result is consistent with the observed PDD results, discussed in previous section, except for the single phase CuO and Cu_2O samples. The main reason for mixed Cu_2O/CuO sample to have the maximum J_{ph} could be due to the charge separation effect at the Cu_2O/CuO interface, as explained above. The applied negative bias to the single phase CuO causes its CB to move towards more negative, resulting in an enhanced J_{ph} values. Similar argument can be applied to the single phase Cu_2O where a more negative CB location far beyond the O_2 reduction potential results in a low reaction efficiency, hence a lower photoresponse.[55, 56]

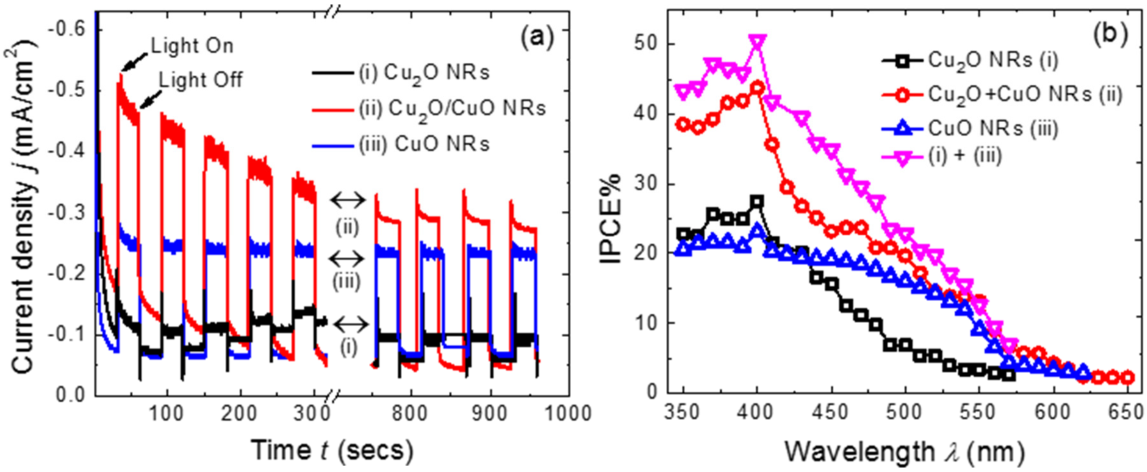

Fig. 4.14(a) Photocurrent response and (b) PEC spectra of selected Cu_xO NR samples.

The IPCE spectra for the three samples are shown in Fig. 4.14(b) for the bias V_c = -0.5V. As expected, the overall higher IPCE% is observed for the mixed phase Cu_2O/CuO NR sample: the highest IPCE% value is estimated to be 44% at λ = 400 nm and it decreases monotonically with increase of wavelength. At λ = 550 nm, the IPCE is still about 10% which indicates that the most of the visible photons have been successfully converted into photocurrents. The IPCE values for Cu_2O and CuO NR samples are observed almost the same and remain as a constant (20 - 27%) in a wavelength regime of $\lambda \leq 430$ nm. The Cu_2O NR sample exhibits a slightly higher efficiency (example at $\lambda = 400$ nm, 27% for Cu_2O and 23% for CuO). However, when $\lambda > 400$ nm, the IPCE for Cu_2O decrease quickly from 27% to 7% at $\lambda = 500$ nm, while for CuO, it decreases very slowly from 23% at $\lambda = 400$ nm to 16% at $\lambda = 500$ nm. This explains why the J_{ph} of CuO sample is larger than that of Cu_2O samples. By closely examining the IPCE spectra of the three samples, one notices that he IPCE response of Cu_2O/CuO sample almost overlap with that of the CuO samples when $\lambda > 500$ nm while for $\lambda < 400$ nm, Cu_2O/CuO sample and Cu_2O have similar spectral shape. In Fig. 4.14(b) we also plot the sum of the IPCE spectra of single phase CuO and Cu_2O and compare it with that of the mixed phase Cu_2O/CuO. Besides the difference in the magnitude for $\lambda < 550$ nm, the spectra shapes are very similar. Clearly the mixed phase Cu_2O/CuO sample greatly enhanced the PEC efficiency. However, it is difficult to compare the IPCE values with the results form literature because of large variations in the reported experimental parameters such as applied bias, concentration and pH values of electrolyte, material morphology, light illumination intensity and wavelength, and so forth.

4.7 Conclusion

In summary, we have synthesized the single phase Cu_2O and CuO, and the mixed phase Cu_2O/CuO NR samples with different mass ratios of Cu_2O/CuO by a simple OAD and post-deposition oxidation method. The single phase Cu_2O NRs have both the direct ($E_g = 2.54$ eV) and indirect ($E_g = 2.02$ eV) electronic transitions while the single phase CuO samples only exhibit a direct transition ($E_g = 2.13$ eV). All of the Cu_xO samples are active and efficient in PDD and PEC under the visible light irradiation. We have also found that all Cu_xO NR samples are stable in PDD reactions while for PEC performance the single phase CuO NR sample is the most stable. However, for both single phase Cu_2O sample and mixed phase Cu_2O/CuO sample, the photocurrents stabilize after multiple cycles, which could be due to slight photocorrosion. Among the three samples, the mixed phase Cu_2O/CuO sample shows the best PEC performance, with the stable photocurrent J_{ph} = -0.24 mA/cm^2 under AM 1.5G, and broad spectra response, with IPCE = 44% at λ = 400 and 10% at λ = 550 nm. Clearly, the mixed phase Cu_2O/CuO NR array could be a good candidate for photocatalysis and PEC applications.

CHAPTER 5

α-Fe_2O_3 NANOSTRUCTURES AND THEIR PHOTOCATALYTIC ACTIVTY

5.1 Introduction

The antibacterial agents currently used in the food industry can be classified into two categories: organic and inorganic. The key advantages of inorganic antimicrobial agents over their organic counterparts are improved safety and stability at high temperatures and pressures.[134, 135] Therefore, the use of inorganic antimicrobial agents to treat food processing equipment and other food contact surfaces to reduce the chances of cross-contamination has attracted a lot of attention.[134, 136] In particular, photo-activated antimicrobial nanostructures are especially interesting.[135, 137, 138] These photocatalysts include various oxide semiconducting materials, their metal hybrid nanocomposites, and doped structures such as, TiO_2, ZnO, CuO, MgO, Ag/TiO_2, TiO_2/CuO, TiO_2/Pt, Au/TiO_2, Fe_2O_3/TiO_2, and N-, C-, S- doped TiO_2.[1, 50, 134, 135, 137-139] Inorganic materials can be used in different forms such as powders, coated on cellulose fibers, or as part of an inorganic/organic nanocomposite coating,[134] and they have been successful in inactivating a wide range of Gram-positive and Gram-negative bacteria.[140]

Of the inorganic antimicrobial agents, TiO_2 is the most common material used for biocidal application since its first introduction by Matsunaga *et al.*, in 1985. However, the practical use of TiO_2 nanostructures as a photocatalyst and bactericidal material is limited due to its large bandgap ($E_g = 3.2$ eV, $\lambda_g = 388$ nm).[1] This means that TiO_2 photocatalysis is generally unproductive under visible light illumination and can utilize no more than about 2-3 % of the incoming solar energy[139] or requires a special UV light source, which is generally harmful to humans. Recently, hematite (α-Fe_2O_3) has attracted a lot of attention for photocatalytic applications due to its ability to absorb a large part of the solar spectrum ($E_g = 2.2$ eV, $\lambda = 564$ nm), its chemical stability (stable through a large PH range), non-toxicity, abundance, and low cost.[141, 142] While magnetite (Fe_3O_4) and maghemite (γ-Fe_2O_3) have been shown to have antibacterial properties,[143-145] α-Fe_2O_3 has not attracted much attention for bactericidal applications, which is surprising because α-Fe_2O_3 materials have already been approved by the Food and Drug Administration (FDA) for food and medical applications. The few reports on the antimicrobial properties of hematite have utilized nanoparticle suspensions, and none have described a photo-induced killing mechanism. Sultana *et al.* detail the antimicrobial effects of nanoparticle solutions of α-Fe_2O_3 treated fly ash,[146] while Azam *et al.* report the inhibition of bacterial growth in α-Fe_2O_3 nanoparticle suspensions.[147] The antimicrobial effects of these nanoparticle solutions under ambient laboratory lighting conditions are related to the nanoparticle size effect, where the adsorption of nanoparticles on bacteria adversely affects the permeability of the cell wall.[148, 149] Not only would suspended nanoparticle adsorption methods be extremely difficult to implement in industrial settings, the cytotoxicity of such methods could make large scale implementation a public health concern.[150] Thus, an investigation of the photocatalytic and photo-induced biocidal properties of α-Fe_2O_3 films is necessary.

In this Chapter, both Fe_2O_3 thin films and Fe_2O_3 OAD nanorod arrays are deposited using electron beam evaporation and are characterized structurally and optically, and are further tested for photocatalytic and antimicrobial applications. The morphologies of the thin films are found to be arrays of very thin and closely-packed columnar structures with prismatic ends, while the OAD films are well-aligned nanorod arrays. All films were determined to be in an oriented α-Fe_2O_3 phase by X-ray diffraction and Raman spectroscopy. The optical properties of the films are found to be consistent with porous α-Fe_2O_3. We find that the thin films are more photocatalytically active than the nanorod arrays for methylene blue degradation under visible light irradiation, while the nanorod arrays have higher antimicrobial activity under visible light irradiation. The biocidal results are described quantitatively by a mathematical model that is based on chemotactic bacterial diffusion and surface deactivation and are explained qualitatively by the different bacteria adsorption and adherence properties of the two film morphologies, which are especially important parameter for α-Fe_2O_3 films due to slow charge transfer kinetics and the relatively low oxidation potential of α-Fe_2O_3.

5.2 Experimental Methods

The source material, Fe_2O_3 (99.85+%, metal base) was used as received to deposit both the α-Fe_2O_3 thin films and NR arrays, *i.e* using the same techniques described in Chapter 2: thin film were deposited at $\theta = 0°$ while OAD NRs at $\theta = 86°$. Samples were prepared on the both glass and Si substrates for different characterization purposes as described in Chapter 4. The deposition rate was maintained at 0.12 nm/s and the final QCM thicknesses reading for film was 1 μm, while for OAD samples the QCM reading was 2 μm. After the deposition, some of the as-deposited films and OAD samples were annealed under ambient conditions at temperatures $T = 250$, 350 and 450 °C, respectively (and using the same annealing furnace, described earlier). During annealing, the heating rate was set to 5 °C per minute, ramping up to the desired annealing temperature, and the samples were maintained at the final preset temperature for 4 hours.

5.3 Morphological Characterization

The morphologies of the prepared samples were examined by a field-emission scanning electron microscope (SEM) equipped with an energy dispersive X-ray spectroscopy (FEI Inspect F). The resulting morphology of the α-Fe_2O_3 films and the NR array samples are shown in Fig. 5.1.

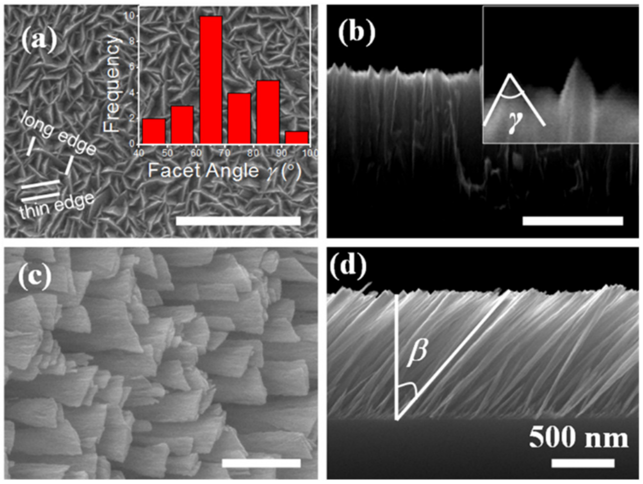

Fig. 5.1 SEM micrographs of (a) top-view and (b) cross-sectional view of the as-deposited Fe_2O_3 thin film, and (c) top-view and (d) cross-sectional view of the as-deposited Fe_2O_3 OAD NR film. Inset in (a) shows the histogram of the measured angle between the prismatic facets at the nanocolumn ends, which are defined in the inset in (b). The scale bars are all equal to 500 nm.

The top view SEM image shows that the Fe_2O_3 thin films have fine, elongated granular surface features (Fig. 5.1a), while the cross-section SEM shows that these surface features are the prismatic ends of vertical columnar-like structures (Fig. 5.1b). As measured from the top view SEM image, the thin edge of the surface grain structures have an average width of 60 ± 20 nm, and the long edge has an average length of 140 ± 30 nm. The angles between the prismatic facets, γ, on the top surface of the columns are measured from the cross-section SEM image (inset Fig. 5.1b) and are most frequently found to be between 60°-70° (inset Fig. 5.1a). The morphology of the thin film is interesting and is the result of the preferred orientation of the polycrystalline grains. This will be discussed in more detail below. The thickness of the thin film is determined to be 920 ± 20 nm. The morphological parameters of the thin films are consistent for all samples at different annealing temperatures.

Figures 5.1c and 5.1d show the top and cross-section views of the OAD Fe_2O_3 films, respectively. As expected, the overall morphology of the OAD films is found to be an array of well-aligned tilted NRs. The NRs are inclined at angle, $\beta = 46° \pm 4°$ with respect to the substrate normal, as indicated in Fig. 5.1d. This angle is also different than the angle predicted by both the Tangent and Cosine rules as it is observed for Cu_xO NRs in Chapter 4. As mentioned in Chapter 4, the material dependent model described by Tanto *et al.* is necessary to explain the tilting angle of the films.[151, 152] The average thickness of the OAD films is found to be 1030 ± 20 nm, while the average NR length is 1480 ± 30 nm. The diameter of the NR increases along the length of the NR, with the fanning out of the diameter being greater in the direction perpendicular to the vapor flux. The average diameter at the top of the NRs in the direction perpendicular to the vapor flux is 200 ± 40 nm, as measured from the top view SEM image. The average diameters of the NRs in the direction parallel with the vapor flux is 50 ± 10 nm at the bottom, 60 ± 10 nm at the middle, and 80 ± 10 nm at the top, as measured from the cross-section SEM image. The NR density (η) was found to be approximately 10 ± 2 rods/μm^2. Using these parameters, the voids of the OAD films are estimated to be greater than 64%.

5.4 Structural Characterization

The XRD data of the all as deposited and annealed samples (annealed at different *Ts)* were recorded with X-ray (Cu Kα radiation (λ = 1.5405980 Å)) incidence angle of 1.5°, in the 2θ range from 20°-80° at step size of 0.014°. Pole figures were measured using an open Eulerian cradle and poly-capillary lens with $\Delta\theta = 5°$ $\Delta\psi = 5°$ (see section 2.1.2, in Chapter 2 for detail). The OAD NR array samples were oriented such that tilting direction was pointed toward the X-ray source at $\theta = 0°$, $\psi = 0°$ for both the 2θ scans and pole figure measurements. Figs. 5.2a and 5.2b show the XRD patterns of the as-deposited and annealed Fe_2O_3 thin films and NRs. Both the thin films and NRs are observed to have similar diffraction peak positions, which, as indicated in Figs. 5.2a and 5.2b, correspond with either the peaks listed for the standard powder diffraction of rhombohedral α-Fe_2O_3 (JPCDS No. 00-033-0664) or with peaks associated with the Si substrate.

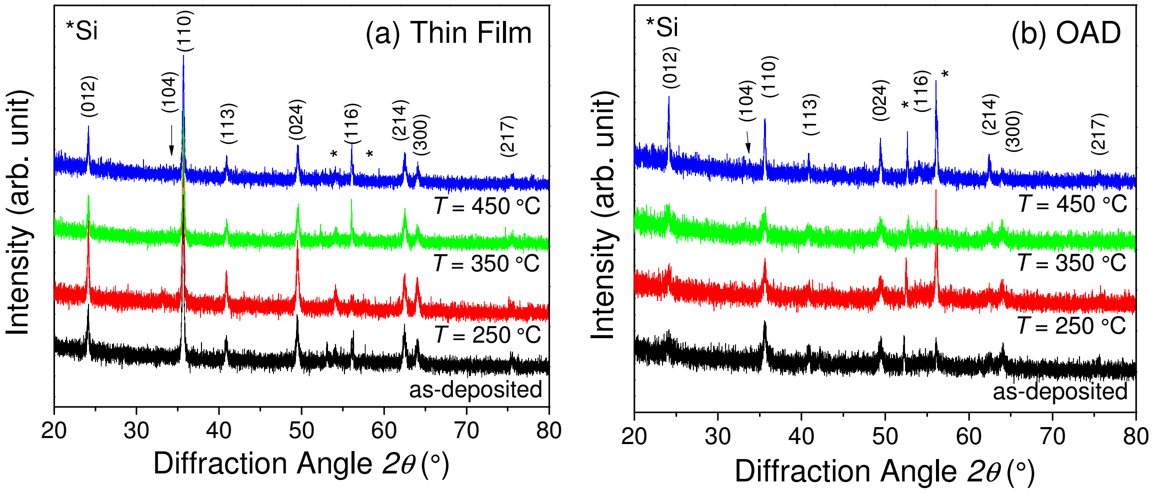

Fig. 5.2 XRD spectra with peak attributions of the Fe_2O_3 (a) thin films and (b) OAD NRs deposited on silicon substrates. Note that the spectra have been shifted vertically for clarity.

Thus, all of the films are in the hematite (α-Fe_2O_3) phase. For the thin films, the peak intensities and widths remain mostly constant across annealing temperatures, indicating that the as-deposited films are primarily polycrystalline α-Fe_2O_3 with a negligible amount of amorphous regions. For the NRs, the XRD peak intensities and widths remain mostly constant for annealing temperatures $T \leq 350$ °C, but at $T = 450$ °C, a moderate amount of peak sharpening is observed. This peak sharpening is not likely due to grain coarsening since coarsening is not seen in the thin films where it is more energetically favorable.[153] Thus, the peak sharpening indicates that the as-deposited OAD films are polycrystalline α-Fe_2O_3 but still contain amorphous regions, and after annealing at $T = 450$ °C, these amorphous regions begin to transition into the α-Fe_2O_3 phase.

Table 5.1 Average crystallite sizes calculated from the (110) and (012) diffraction peaks in the Fe_2O_3 thin films and NRs.

	Thin Films		Nanorods	
Sample	(110) (nm)	(012) (nm)	(110) (nm)	(012) (nm)
as-deposited	42	83	30	17
$T = 250$ °C	47	69	35	42
$T = 350$ °C	53	69	18	30
$T = 450$ °C	42	83	47	52

In order to quantify the behavior of crystallite growth, the average grain sizes of α-Fe_2O_3 crystallites for the samples are estimated using the Scherrer equation for the (110) and (012) crystal plane reflectances and are listed in Table 1. The average crystallite size of the thin films are in the range of 42-53 nm in the [110] direction (note that all crystal orientations are written in the hexagonal (*hkl*) notation, omitting the redundant index *i*). The estimated crystal sizes in the direction perpendicular to the (012) planes are larger than in the [110] direction and are 83 nm for the as-deposited and T = 450 °C samples and 69 nm for the T = 250 °C and T = 350 °C samples. The apparent lack of relationship between annealing temperature and crystallite size agrees well with the supposition that there is a negligible amount of amorphous region in the thin films to feed further grain growth at the higher annealing temperatures. The fluctuations in crystallite size for the different samples could be related to the local environment of the substrate during film growth. The average crystallite sizes of the NRs are generally smaller than those of the thin films; they are between 30-47 nm in the [110] direction and 17-52 nm perpendicular to the (012) planes (Table 1). Aside from the T = 350 °C sample, the crystallite size generally increases with annealing temperature, suggesting that there is grain growth occurring through an amorphous to α-Fe_2O_3 transition. The smaller crystallite size in the T = 350 °C sample could be the result of the local environment of that sample during film growth, and that larger grain growth is limited by the absence coarsening for temperatures $T \leq 450$ °C. As mentioned above, the columnar structures and prismatic facets observed in the SEM images of the thin films suggest that the Fe_2O_3 exhibits a preferential growth direction. In the standard powder diffraction pattern of α-Fe_2O_3, the (104) crystal plane reflectance is the most intense, but this reflectance is not observed in the XRD spectra of the OAD and thin films. Instead, the most intense reflectance for both sets of films, except for the OAD film annealed at T = 450 °C, is the (110) reflectance. In order to better understand the crystallite orientations of the films, the XRD pole figures for the (110), (012), and the (104) reflectances were measured for both the thin films and NRs deposited on glass substrates and annealed at T = 350 °C (Fig. 5.3). Note that the pole figures have not been corrected for background or defocusing. For the thin film, there appears to be a more intense region from ψ = 0°-30° in all pole figures (Fig. 5.3), which could be due to the background, defocusing, or to a changing orientation as film growth develops. However, it is clear that the (110) pole is centered over $\psi = 0°$, the (012) pole forms a ring around $\psi = 32°$, and the (104) pole figure has an intensity maximum at $\psi = 54°$. These positions are consistent with the [110] growth direction of α-Fe_2O_3, which would orient the poles of (110), (012), and (104) at $\psi = 0°$, $\psi = 36°$, and $\psi = 56°$, respectively. The [110] growth direction is likely responsible for the morphological parameters of the thin films seen in the SEM images.

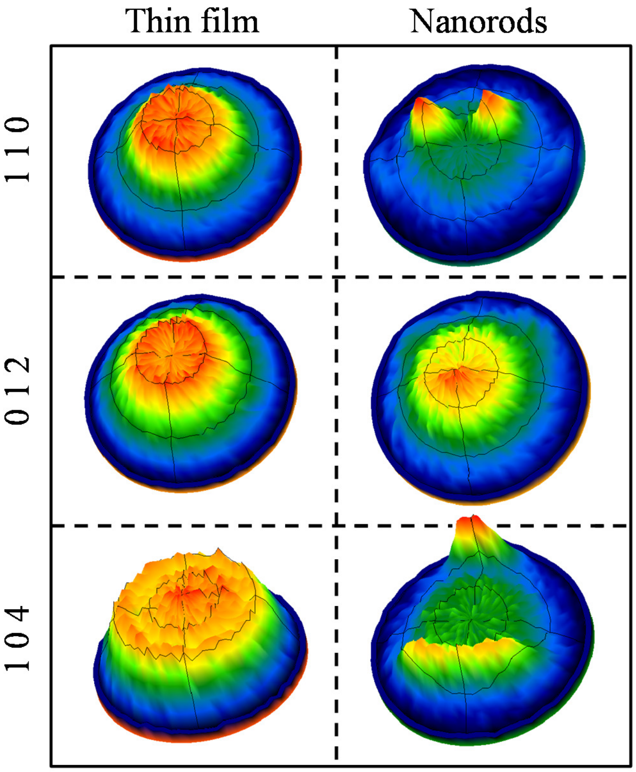

Fig. 5.3 Pole figures of the Fe_2O_3 thin film and OAD NRs annealed at T = 350 °C for the (110), (012), and (104) crystal plane reflectances of α-Fe_2O_3. Note that the NR sample was oriented such that the tilting direction was pointed toward the X-ray source at θ = 0°, ψ = 0°.

This can be seen in the columnar structures, as the (001) plane is normal to the substrate and is also a cleavage plane of α-Fe_2O_3. The width and length of the prismatic surface features are 56 ± 21 nm and 138 ± 33 nm, respectively and scale with the length of the unit axes of α-Fe_2O_3, which are a = 5.04 Å and c = 13.76 Å. The angles between the exposed facets of the prismatic columnar tips are found to be primarily between γ = 60°-70°, which matches well with the inner angle, 60°, between the (110) planes in α-Fe_2O_3.

The pole figures for the (110), (012), and the (104) reflectances of the OAD NRs are shown in Fig. 5.3. The (110) poles of the NRs are centered over ψ = 35°, the (012) poles are cantered over ψ = 10°, and the (104) poles are centered over ψ = 47° and ψ = 73°. The orientation of the [110] direction in the NRs is tilted away from the substrate normal at ψ = 35°, but it is not fully aligned with the material growth direction, which is at β = 46°. While the [110] directions of the thin and OAD films are oriented differently relative to the substrate, both appear to be influenced by the direction of material growth. However, the slight misalignment between the material growth direction and the [110] direction might contribute to the greater amorphization of the NRs compared to the thin films. Material growth in the [110] direction for both films could be the result of oxygen deficiency in the incoming vapor flux. The [110] direction is Fe-rich, and the (110) planes are relatively Fe-deficient[154] and have among the lowest surface energies of the main faces of α-Fe_2O_3 crystallites.[155] It is interesting to note that growth in the [110] direction appears to be common in hematite nanostructure synthesis and has been seen in nanostructures fabricated by hydrothermal methods,[156] chemical vapor deposition,[157] pulsed laser deposition,[158] and thermal oxidation.[154]

In order to further confirm crystal phases of the Fe_2O_3 films, Raman spectroscopy measurements were carried out for both the as-deposited and the T = 450 °C annealed samples. Raman spectroscopy measurements were recorded using a Bruker Senterra Raman microscope, by exciting the samples with a 532 nm wavelength laser at room temperature, with a 10 sec exposure time and 1 mW power. Fig. 5.4(a)-(b) show the measured spectra for film and NR arrays.

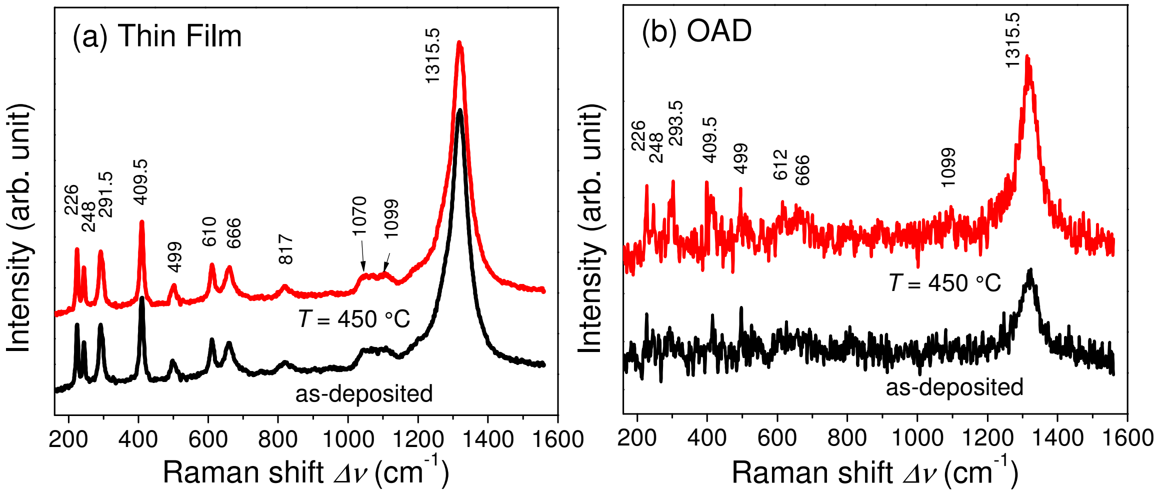

Fig. 5.4 Raman spectra of the as-deposited and 450 °C annealed Fe_2O_3 (a) thin films and (b) OAD NRs. Note that the spectra have been shifted vertically for clarity.

Each spectrum represents the average of three measurements, which were recorded over the detection range from $\Delta\nu$ = 200 - 1600 cm^{-1} at room temperature. Both the thin films and NRs are observed to have similar peak positions, although there is a greater noise level in the NR samples due to the smaller material volume. For both sets of films, the peak positions do not change after annealing at T = 450 °C. Importantly, all of the observed Raman peaks are attributed to α-Fe_2O_3. The peaks at $\Delta\nu$ = 226, 248, 292, 410, 499, and

610 cm^{-1} respectively correspond with the A_{1g}, E_g, E_g, E_g, A_{1g}, and E_g modes of α-Fe_2O_3.[159] The peak at $\Delta\nu$ = 1316 cm^{-1} is attributed to a second order phonon mode of α-Fe_2O_3.[160] The peak appearing at $\Delta\nu$ = 666 cm^{-1} is attributed to an IR mode that that can manifest in the Raman spectra of α-Fe_2O_3 due to the relaxation of Raman selection rules in nanostructured materials.[159] The peak at $\Delta\nu$ = 820 cm^{-1} agrees well with the predicted Raman shift due to one magnon scattering.[161] Finally, the smaller peaks at $\Delta\nu$ = 1070 and 1099 cm^{-1} are consistently seen in the Raman spectra of pure α-Fe_2O_3, but are typically unassigned.[159, 162, 163] Thus, the Raman spectroscopy measurements confirm the XRD results in showing that the films are purely hematite.

5.5 Optical Properties

The optical properties of the samples were characterized from the measured Transmittance spectra using the JASCO V-570 (and neglecting the reflectance), as shown in Fig. 5.5(a)-(b). Visual inspection suggests that the appearance of thin films and OAD films are optically similar to α-Fe_2O_3, as both sets of films exhibit the reddish-brown color, typical of hematite (photographic insets in Figs. 5.5a and 5.5b). Both sets of films show significant attenuation of visible light beginning around λ = 600 nm, with the OAD films being more transparent due to their smaller material volume and larger porosity. The interference fringes seen in the spectra of the thin films are not seen in the OAD films due to decoherence from the broadband diffuse scattering of the NRs. Using the interference fringes, the refractive index and porosity of the Fe_2O_3 thin films can be estimated *via* the envelope method.[164] As mentioned in Chapter 2, the refractive index is calculated using the equations:

$$n(\lambda) = \left[N + \left(N^2 - n_s^{\ 2} \right)^{1/2} \right]^{1/2}, \tag{5.1}$$

$$N(\lambda) = 2n_s \frac{T_{\max} - T_{\min}}{T_{\max} T_{\min}} + \frac{n_s^{\ 2} + 1}{2} \quad , \tag{5.2}$$

where T_{max} is the transmittance given by the maximum envelope function, T_{min} is the transmittance given by the minimum envelope function, and n_s is the refractive index of the substrate (n_s =1.52, for glass). The film porosity, P, can be estimated from the index of refraction, n, using,[165]

$$P = \left[1 - \frac{n^2 - 1}{n_d^2 - 1} \right] \times 100, \tag{5.3}$$

where $n_d = 2.87$ is the pore-free refractive index of α-Fe_2O_3 at $\lambda = 750$ nm. The results are summarized in Table 2. As expected, the refractive indices of the thin films are less than the literature value due to the nanocolumnar morphology. The porosities of the thin films vary, with the as-deposited film being the least porous with 28% void and the T = 350 °C film being the most porous with 43% void. The porosity of the thin film scales with the -

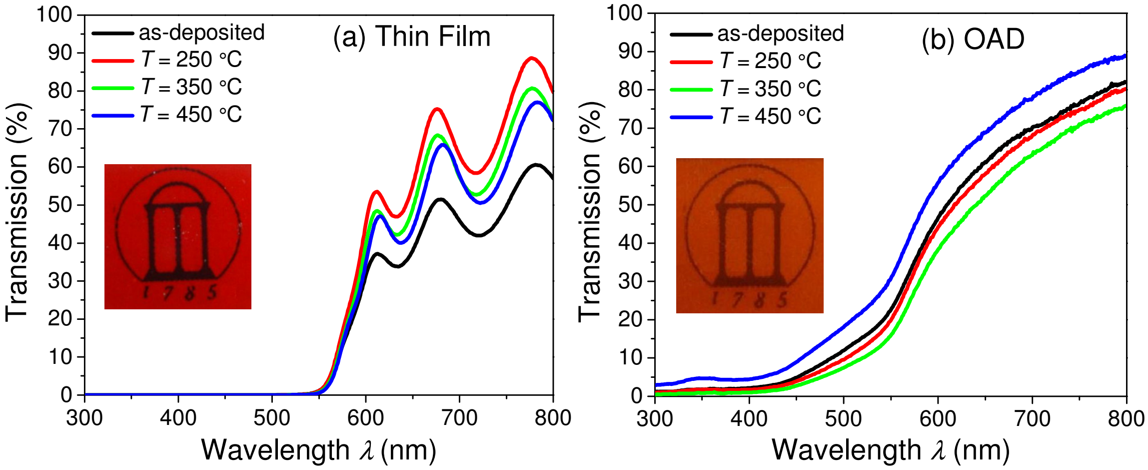

Fig. 5.5 Transmittance spectra of the Fe_2O_3 (a) thin films and (b) OAD NRs. Insets show a representative photographic image of a (a) thin film and (b) nanorod sample, deposited on glass substrates placed over a University of Georgia logo.

estimated crystallite size in the direction perpendicular to the (012) planes and not with the crystallite size in the [110] direction. This observation is consistent with the preferred orientation of the Fe_2O_3 thin films seen in the XRD analysis and with the supposition that the columnar morphology is primarily responsible for the porosity in the thin films. The varying porosities are not expected to be the result of the annealing treatment; instead, they are likely the result of different local environments during film growth.

The optical absorption coefficient $\alpha(\lambda)$ is calculated from the transmittance ($\%T$) by neglecting the reflectance (*i.e.* using Eqn. 1.12). Then used the estimated $\alpha(\lambda)$ to obtain the Tauc's plot, using Eqn. 2.5 and hence estimated the bandgaps. The estimated bandgaps from Tauc's plot analyses for the Fe_2O_3 thin films and NRs are summarized in Table 5.2, below. For the thin films, E_g = 2.17 - 2.21 eV, while for the NRs E_g = 2.07 - 2.11 eV. The bandgap energies are similar within each set of samples, but the extrapolated bandgaps of the NRs are less than the thin films. This is likely due to the increased diffuse scattering of the OAD NRs at longer wavelengths, but also could be attributed to a wider Urbach tail. However, these results agree fairly well with previously reported results for the hematite bandgap, E_g = 2.1- 2.7 eV. [166-169]

Table 5.2 Derived optical parameters of the Fe_2O_3 thin films and nanorods.

	Thin Films			Nanorods
Sample	Refractive Index at 750 nm	Porosity (%)	Bandgap (eV)	Bandgap (eV)
as-deposited	2.49	28.1	2.21	2.09
T = 250 °C	2.36	36.9	2.19	2.08
T = 350 °C	2.26	43.2	2.17	2.07
T = 450 °C	2.46	30.2	2.17	2.11

5.6 Photocatalytic Dye Degradation

The photocatalytic activities of the samples were evaluated from the MB degradation, of initial concentration ~31 μM, under the visible light irradiation. The same experimental procedures, described in previous Chapter, were followed to estimate the degradation rates of MB. The incident light intensity was also maintained the same as used for previous photodecay measurements (Chapter 4). Based on the observed results from control experiments, that were performed with the same photocatalyst but no light and with the light but no photocatalyst, and the photocatalytic dye degradation results of the photocatalysts, it can be concluded the that degradation of dye was a true photocatalytic activity. As see in Fig. 5.6(a)-(b), all Fe_2O_3 samples exhibit the appreciable dye degradation/decomposition rates (represented by the decreasing normalized peaks). The change in the intensity of the MB absorbance peak at λ = 663.7 nm versus time for all samples exhibits exponential decay behavior (a pseudo-first order behavior as explained in Chapter 2). So, we obtain the decay rates κ_c by fitting the Eqn. (1.30). The fitting results are shown in Fig. 5.6 as solid curves, and the rate constants, κ_c, for different samples are summarized in Table 5.3. For the thin films, the samples annealed at the higher temperatures are more efficient photocatalysts, with the sample annealed at T = 350 °C showing the highest decay rate at $\kappa_c = 0.127 \pm 0.005$ hr^{-1}. The slowest decay rate of all samples is the thin film annealed at T = 250 °C, which has a decay rate of $\kappa_c = 0.095 \pm 0.002$ hr^{-1}. The decay rates of the NRs are not a monotonic function of annealing temperature and are similar in value to the decay rates of thin films and range from κ_c = 0.100-0.121 hr^{-1}. While it is difficult to compare the results from different MB degradation experiments due to different experimental parameters and setups, it is worthwhile to note that the MB decay rates measured for the Fe_2O_3 samples are slower than some decay rates measured by other groups. For example, Zhang *et al.* found that α-Fe_2O_3 nanotube electrodes fabricated by sonoelectrochemical anodization under 100 mW/cm^2 white light illumination exhibited a decay rate of κ_c = 0.96 hr^{-1} in a 1 μM MB solution.[170] Also, hydrothermally-prepared α-Fe_2O_3 NRs (0.2 mg/ml) have been to shown to exhibit a decay rate of κ_c = 0.64 hr^{-1} under visible light illumination in a 10 μM MB solution.[171] Due to the difficulty in comparing results from other groups and experiments, we also fabricated α-Fe_2O_3 nanoparticles by co-precipitation to compare with the results for the NRs and thin films. We found that the nanoparticle MB photodegradation rate, $\kappa_c = 0.055 \pm 0.002$ hr^{-1}, was less than half the rate of the NRs and thin films under the same experimental conditions and for roughly the same amount of photocatalytic material, 0.6 mg. Thus, the nanorods and thin films do outperform α-Fe_2O_3 nanoparticles we synthesized using wet chemistry.

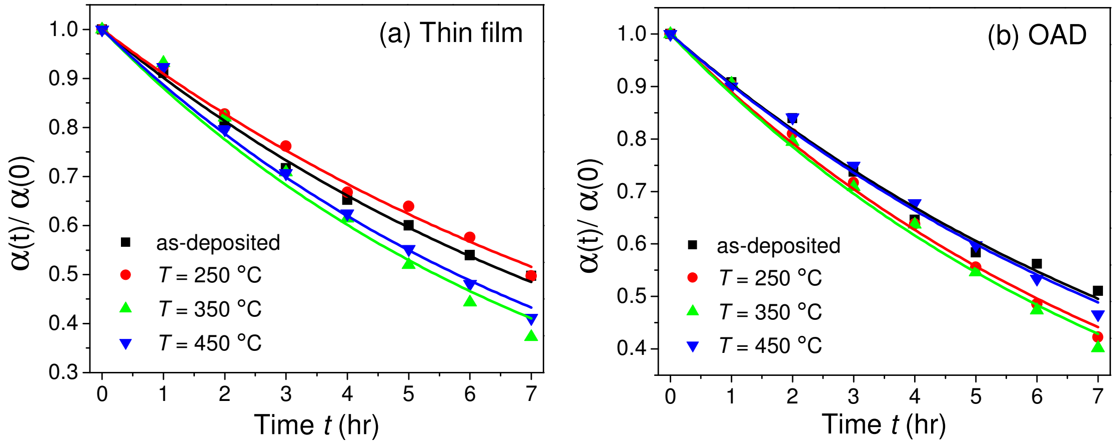

Fig. 5.6 Normalized MB absorbance intensities of the λ = 663.71 nm peak versus time for the Fe_2O_3 (a) thin films and (b) OAD NR*s. The curves correspond to the first-order exponential decay fittings of the data points, from which the decay rate, κ_c, was determined.*

Finally, it is interesting to note that the photodecay rates of the nanorods are slightly smaller than those of the thin films, even though the NRs have a larger porosity.

Effective photocatalysts are films that exhibit efficient charge transfer to and across the semiconductor-solution interface. The annealing process generally increases crystallite sizes and passivates defects, such as oxygen vacancies, improving charge life times. This is why the catalytic efficiency, for the most part, increases with annealing temperature for both the OAD and thin film samples. However, defects can be beneficial by acting as catalytic hot spots and increasing the conductivity of the material; thus, the removal of too many defects might explain the decrease in catalytic efficiency at the highest annealing temperature for both the OAD and thin films. It is well known that α-Fe_2O_3 has anisotropic charge transport properties. In particular, the conductivity in the [110] direction, or within the (001) plane, is known to be up to four magnitudes higher than in directions orthogonal to it.[172] Thus, the preferred orientation of the Fe_2O_3, as described above, could create an environment favorable for increased charge separation due to the larger crystalline sizes in the more conductive [110] direction, resulting in less grain boundary scattering and trapping of free charges.

However, in addition to efficient charge transfer within the nanostructure, charge transfer across the nanostructure-solution interface is equally important. As mentioned above, α-Fe_2O_3 is known to have slow kinetics at aqueous interfaces, but specific crystal planes have been found to be more reactive for certain photocatalytic and catalytic reactions. Gao *et al.* concluded that α-Fe_2O_3 NRs were more efficient for CO oxidation than α-Fe_2O_3 nanotubes and nanocubes due to their greater area of exposed (110) planes.[173] Similar results regarding the greater efficiency of (110) planes for CO oxidation have been reported elsewhere in the literature.[174, 175] The explanation for the greater efficiency of (110) planes is that CO adsorbs first to Fe atoms and then is subsequently oxidized by a -

Table 5.3 Photocatalytic decay rates, κ_c, and bacterial inactivation rates, κ_b, of the Fe_2O_3 thin films and nanorods.

	Methylene Blue, κ_c (hr^{-1})		*E. coli* O157:H7 κ_b (cm/s)	
Sample	Thin Film	Nanorods	Thin Film	Nanorods
as-deposited	0.103 ± 0.001	0.100 ± 0.002	1.2×10^4	4.6×10^4
T = 250 °C	0.095 ±0.002	0.117 ± 0.002	—	—
T = 350 °C	0.127 ±0.005	0.121 ± 0.003	1.5×10^4	4.8×10^4
T = 450 °C	0.120 ±0.003	0.102 ± 0.002	—	—

neighboring surface O atom. Since (110) planes have a large number of surface Fe atoms, more CO is adsorbed and oxidized there.[176] Similarly, Weiss *et al.* found that cationic Fe sites on the (001) surface were fundamentally important during the catalytic decomposition of ethylbenzene and styrene due to greater reactant adsorbance at these sites, and they postulate a general rule that the chemisorption reactivity of metal oxides requires the presence of acidic metal sites at the surface.[177] Finally, Zhou *et al.* found that the visible light photodegradation rate of rhodamine B by hematite nanoparticles in the presence of H_2O_2 strongly depended on the exposed facets of the hematite nanoparticles, when normalized to exposed surface area.[178] In particular, they found that the reactivity of different exposed planes obeyed the relationship, (110) > (012) >> (001). While the photocatalytic and catalytic reactions mentioned above are different than the MB degradation experiment described here, it is clear that reactant adsorption at active Fe surface sites is a critically important factor in determining the efficiency of α-Fe_2O_3 photocatalysts. Direct adsorption to a reactive α-Fe_2O_3 surface is especially important given the slow charge-transfer kinetics of hematite within the bulk and at interfaces. Furthermore, the reactant must be directly oxidized because the valence band of α-Fe_2O_3 is not sufficiently positive to generate hydroxyl radicals (at pH = 7), nor is the conduction band sufficiently negative to generate superoxides,[179, 180] which precludes oxidation at a distance *via* reactive oxygen species and requires direct contact of the reactant with the surface. Thus, it is likely that the exposed crystal planes of the Fe_2O_3 thin film provide more reactive adsorbance sites for MB molecules, which leads to the slightly higher photocatalytic efficiency of the thin films relative to the OAD films, even though the OAD films are more porous and have a higher surface area.

5.7 Bactericidal Activity

The visible light induced antimicrobial activities of the as-deposited and T = 350 °C samples Fe_2O_3 samples were compared against *E. coli* O157:H7 using the method described in Chapter 2. The choice of these two were to compare the antimicrobial activity the samples those showed the lowest and the highest performance. Figs. 5.7a and 5.7b show the experimental results for bactericidal activity. From the figures, it is observed that the NR samples are much higher performance (than the thin film samples). The as-deposited and T = 350 °C thin films show 1.1 and 1.5 log reductions in bacteria over 3 hours, respectively, while the as-deposited and T = 350 °C NR samples are exponentially more efficient, showing log reductions of 4.6 and 4.9 over 3 hours, respectively. It is difficult to compare these antimicrobial efficacy results with results from the literature due to large variations in reported experimental parameters such as initial bacteria concentration and strains, illumination intensity and wavelength range, substrate size, etc. Additionally, most antimicrobial tests of TiO_2 are conducted using UV light, while the Fe_2O_3 samples in this experiment were tested using visible light. However, it is worth noting that the log reductions of the NR samples compare favorably with results published in the literature for the photocatalytic inactivation of *E. coli* using state of the art TiO_2-based coatings, which have reported log reductions that range from ~3 to ~5 over three hours in recent experiments,[181-184] and also compare favorably with other photocatalytic materials such as sphalerite[185] and bismuth vanadate nanotubes,[186] both of which were recently reported to have log reductions of *E. coli* of ~2.5 over three hours. Furthermore, hematite is the most stable form of iron oxide and should maintain its efficacy over time. Thus, these initial results indicate that the Fe_2O_3 NRs are promising candidates for antimicrobial applications, especially given the intrinsic benefits of α-Fe_2O_3 such as low cost, abundance, non-toxicity, visible light utilization, and FDA approval for food and medical applications, as mentioned above.

The time dependent biocidal effect of a coated photocatalyst surface has not been well understood, though there are numerous models for suspended nanoparticle/biocidal solutions.[187-190] It is necessary to develop a physical model of the antimicrobial experiment in order to quantify the bacterial inactivation rate of the samples. We believe that this system can be described by diffusive transport combined with a reactive boundary condition. The one-dimensional chemotaxis diffusion equation is given by,[191]

$$\frac{\partial b}{\partial t} = -\frac{\partial}{\partial x}\left(-D\frac{\partial b}{\partial x} + \chi b\frac{\partial c}{\partial x}\right) , \qquad (5.4)$$

where $b(x, t)$ is the bacteria concentration, D is the bacteria diffusion coefficient, χ is the chemotactic sensitivity coefficient, and $c(x, t)$ is the chemoattractant concentration. If we assume that both D and χ are constant throughout the experiment and the chemoattractant gradient has no curvature, i.e., $\partial^2 c / \partial \mathrm{x}^2 = 0$, Eq. (5.4) reduces to the one-dimensional advection equation for $b(x, t)$,

$$\frac{\partial b}{\partial t} = D\frac{\partial^2 b}{\partial x^2} - \chi^* \frac{\partial b}{\partial x}, \tag{5.5}$$

where χ^* is the chemotactic sensitivity coefficient that has been modified by the chemoattractant gradient. The two boundary conditions are,

$$\left.\frac{\partial b}{\partial x}\right|_{x=0} = 0, \tag{5.6}$$

$$\left.\frac{\partial b}{\partial x}\right|_{x=L} = -\frac{\kappa_b}{D} b(x = L, t), \tag{5.7}$$

where L is distance from the solution/ambient interface ($x = 0$) to the solution/Fe_2O_3 interface ($x = L$), and κ_b is the bacterial inactivation rate of the sample. Equation 10 defines the biocidal effect of the surface. Thus, the major assumptions of this model are: the motional behavior of *E. coli* O157:H7 in an aqueous environment that is supported by a Fe_2O_3 film can be described by a one-dimensional chemotaxis equation; the volume of the aqueous environment does not change appreciably with time; bacteria cannot escape from ambient/solution interface; and bacteria are inactivated by the Fe_2O_3 film at a rate that is proportional to the bacteria concentration at the solution/Fe_2O_3 interface. Using the two boundary conditions, Eqn. (5.6) and Eqn. (5.7), and the initial condition that $b(x, t = 0) = b_0$, the solution to Eqn. (5.5) is given by (see Appendix C, for full derivation):

$$b(\xi, t) = \sum_{n=1}^{\infty} c_n e^{-D\lambda_n^2 t} \cos(\lambda_n \xi), \tag{5.8}$$

$$\xi = x - \chi^* t \,, \tag{5.9}$$

$$\lambda_n = \frac{\kappa_b}{D} \cot \lambda_n L \,, \tag{5.10}$$

$$c_n = \frac{2 b_0 \lambda_n \sin \lambda_n L}{\lambda_n{}^2 L + \lambda_n \sin \lambda_n L \cos \lambda_n L} \,. \tag{5.11}$$

The experiment was modeled using the following values for the parameters: $n = 50$; $b_0 = 10^7$ CFU/ml; $L = 0.1$ cm; $D = 2.6\times10^{-5}$ cm^2/s (average of Table II from Lewus and Ford);[192] $\chi^* = 4\times10^{-5}$ cm^2/s (10% of average of Table III from Lewus and Ford).[192] The bacterial inactivation rate, κ_b, was varied until the predicted curve matched the experimental datum at $t = 180$ min. The results for κ_b range from $\kappa_b = 1.2\times10^4$ cm/s for the as-deposited thin film sample to $\kappa_b = 4.8\times10^4$ cm/s for the nanorod sample annealed at $T = 350\ ^\circ$C; a summary is shown in Table 5.3 and the resulting curves are plotted in Fig. 5.7(a) and Fig. 5.7(b). The model and parameters predict a non-linear curve for the log reduction, and the agreement between the model and experimental data is reasonably good given the assumed values of D and χ^* and the approximations made during the derivation. Experimentally determined values of D and χ^* could improve the quality of the fitting.

The slight increase in bacterial inactivation rate for both sets of films after annealing is unsurprising. However, the superior performance of the NRs relative to the thin films is surprising, especially given the results from the photocatalytic experiment, where the thin films are found to be slightly more efficient than the NR samples. While the degradation pathways for both MB and *E. coli* O157:H7 rely on the oxidation processes, the physical sizes of MB (~1 nm) and *E. coli* O157:H7 (~1 μm) are different. Thus, the MB molecule can reach all of the exposed surfaces of the plate-like structures of

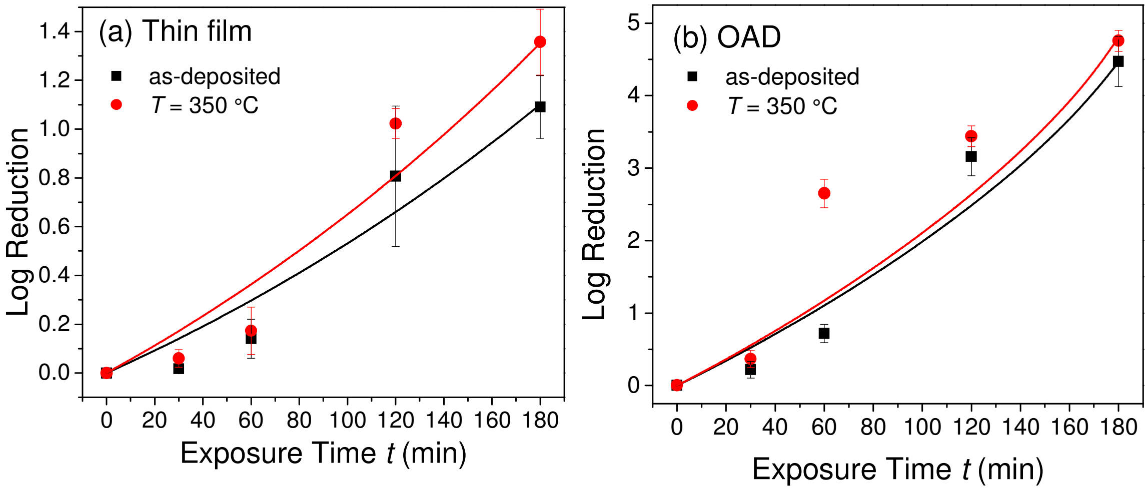

Fig. 5.7 Log reduction of E. coli O157:H7 as a function of irradiation time for the as-deposited and T = 350 $^{\circ}$C Fe_2O_3 (a) thin films and (b) OAD NRs. The solid curves are the chemotaxis model fits for the log reduction.

the thin films and the NRs of the OAD films, but *E. coli* O157:H7 is much larger than the lateral spacing of the thin films and NRs and is, therefore, confined to the top surfaces of each film. As described above, direct contact with the Fe_2O_3 surface is extremely important for oxidative processes given the slow aqueous kinetics and the relatively low oxidation potential of the Fe_2O_3 films. Furthermore, it has been shown that the rate of adsorption of *E. coli* on a photocatalyst's surface is positively correlated with its bactericidal effect.[193] Thus, it is clear that the ways in which *E. coli* O157:H7 adheres and interacts with the top surfaces of the thin films and NRs determine their relative efficacy for antimicrobial applications. Further studies are underway to characterize the differences between the behaviors of bacterial adhesion to NRs and thin films. However, given the greater biocidal effects of the NR samples, it is expected that the NR array morphology promotes longer contact times of *E. coli* O157:H7 with the Fe_2O_3 surface, while the bacteria should show an aversion to the prismatic ends of the thin film surface. The greater contact time with the α-Fe_2O_3 surface increase the likelihood that *E. coli* O157:H7 can be inactivated *via* the direct photochemical oxidation of intracellular coenzyme A.[50, 51] The effects of surface properties on cell adhesion are still not well understood and are currently a hot topic in the literature.

5.8 Conclusions

We have demonstrated that both Fe_2O_3 thin films and Fe_2O_3 nanorod arrays fabricated by electron beam evaporation are purely hematite (α-Fe_2O_3) using structural and optical methods. The thin films were found to be oriented nanocolumnar α-Fe_2O_3 with exposed (110) and (001) planes and the OAD films were found to be arrays of oriented α-Fe_2O_3 nanorods. Furthermore, the Fe_2O_3 thin films and Fe_2O_3 nanorods were found to be photocatalytically and antimicrobially active under visible light illumination. However, the different morphologies of the films (prismatic nanocolumn *versus* nanorod) and the different nature of the reactants (organic dye, ~1 nm, *versus* bacteria, ~1 μm) highlighted how adsorbate/surface interactions are an important consideration for photocatalytic and antimicrobial applications of α-Fe_2O_3 films. Specifically, adsorbance of molecular reactants and strong adhesion of bacteria to active surface sites are required to maximize photo-induced degradation. A chemotactic mathematical model of bacterial inactivation was developed to quantify the antimicrobial efficiency of surface coatings. These results are important considerations for future designs of α-Fe_2O_3 antimicrobial coatings for the inactivation of *E. coli* O157:H7. It is also important to note, that depending on the specific environment, the nanorod morphology will have some unique challenges if transitioned from the laboratory to an industrial setting. Nanostructures will have to be designed to accommodate the specific environment, which might compromise the antibacterial performance. However, this is true for any antibacterial agent working in a complicated environment where there could be interference at the bacteria/structure interface. Further experiments are underway in order to investigate how the morphology of electron beam evaporated α-Fe_2O_3 can be tuned to optimize bacterial contact with the photocatalytic surface in order to maximize its biocidal effects.

CHAPTER 6

CONCLUSIONS AND FUTURE WORK

In this dissertation, the photocatalytic activities of visible light activated MOs including Cu_xO (x= 1, 2), α-Fe_2O_3 and WO_3 nanostructures fabricated by OAD and DSG were studied. In particular, photocatalytic activities were analyzed for organic dye degradation, solar energy conversion, and bactericidal efficiencies, *i.e.*, depending on the individual material's morphological, structural, optical, and electronic properties. For instance, WO_3 SMRs were examined for dye degradation under both the UV and visible light irradiations while the Cu_xO (x = 1, 2) and α-Fe_2O_3 nanorods were additionally characterized for PEC and bactericidal properties respectively, *i.e.*, under visible light illuminations. Regardless of application types, we found that the photocatalytic activity of a MO photocatalyst depends on various factors including material properties and the experimental parameters. Material properties are associated with the material composition, morphology or the total active surface area, crystallinity and active facets, light absorption (bandgap) and charge generation property, CB and VB locations, charge diffusion length, life time of photocarrier, and charge transport on the material's surface (depending on the impurity/defects). More active surface area of a photocatalyst could results the better photocatalytic activity even if the two materials (of different kinds) have their other intrinsic properties the same, including their morphology, bandgap, band-edge locations etc. Similarly, crystallinity of a photocatalyst may improve the charge transfer and hence the photocatalytic activity (but some specific facets can be more active than others). Charge diffusion length is an intrinsic property of the materials. Short carrier diffusion length is one of greatest detrimental factors to reduce the photocatalytic activity (for example Fe_2O_3). In other words, longer life time of photogenerated charge carriers is always advantageous in environmental remediation and solar energy conversion applications. Experimental parameters that might affect the photocatalytic performance in above mentioned applications include: reaction temperature, redox potentials of the reactant couple, concentration and pH of the reaction medium, intensity of light source, the amount of catalyst used, the amount of oxidizing agent (added in the reaction solution) etc.

For photodecay, light absorption by the dye solution also affect the performance *via* dye sensitization reaction. In this case, activity could be enhanced by injecting the photoexcited charge carriers from dye molecules to the photocatalyst based on the HOMO/ LUMO alignment with CB and VB locations of the photocatalyst. For solar energy conversion, the external bias potential applied determine the photogenerated electrical output or the amount of H_2 produced depending on the majority and minority (*i.e.*, the photogenerated) carriers in the photocatalyst and the direction of applied bias. Suitable electrolyte, its pH value, and concentration could also affect the stability and photocatalytic performance. In bactericidal activity, the adsorption of photocatalyst (if the photocatalyst is suspended as nanoparticles in a solution) or the surface contact with the immobile photocatalyst are very important parameters to determine the overall inhibition rates.

The future direction will mainly be based on the above mentioned applications and to improve the efficiency and the stability of a VLAP. Firstly, based on the idea of charge separation at the co-doped or doped metal-semiconductor interfaces (of metal on oxide matrix) and at the semiconductor-semiconductor heterojunctions, one could design heterostructures that extend the life time of photogenerated charge carriers, thus make the photocatalyst more efficient. For instance, gold or silver nanoparticles can be doped to Fe_2O_3 to enhance charge separation. Similarly the heterostructured Cu_2O/ Fe_2O_3 could also be a good candidate. Secondly, one could even improve the activity of a single material by making more porous nanostructures, then optimizing the length, morphology, and structural parameters. For example, by adjusting the thickness or volume of the material, one could reduce the charge recombination. The estimation of required length/dimension to absorb the certain percentage of photons (of given energy) can be helpful to design the material thickness. Finally, one could combine the GLAD technique with other nanofabrication methods, such as hydrothermal, sol-gel, spray pyrolysis, etc., to further vary the material selection for heterostructures.

REFERENCES

1. M. R. Hoffmann, S. T. Martin, W. Y. Choi and D. W. Bahnemann, *Chemical Reviews*, 1995, **95**, 69-96.
2. A. Kubacka, M. Fernandez-Garcia and G. Colon, *Chemical Reviews*, 2012, **112**, 1555-1614.
3. Z. He, Q. Xu and T. T. Yang Tan, *Nanoscale*, 2011, **3**, 4977-4983.
4. A. Y. Booshehri, S. C.-K. Goh, J. Hong, R. Jiang and R. Xu, *Journal of Materials Chemistry A*, 2014, **2**, 6209-6217.
5. A. Paracchino, V. Laporte, K. Sivula, M. Graetzel and E. Thimsen, *Nature Materials*, 2011, **10**, 456-461.
6. X. Qiu, M. Miyauchi, K. Sunada, M. Minoshima, M. Liu, Y. Lu, D. Li, Y. Shimodaira, Y. Hosogi, Y. Kuroda and K. Hashimoto, *Acs Nano*, 2012, **6**, 1609-1618.
7. H. Yu, H. Irie, Y. Shimodaira, Y. Hosogi, Y. Kuroda, M. Miyauchi and K. Hashimoto, *Journal of Physical Chemistry C*, 2010, **114**, 16481-16487.
8. K. Hashimoto, H. Irie and A. Fujishima, *Japanese Journal of Applied Physics*, 2005, **44**, 8269-8285.
9. K. Sunada, T. Watanabe and K. Hashimoto, *Journal of Photochemistry and Photobiology a-Chemistry*, 2003, **156**, 227-233.
10. P. Basnet, G. K. Larsen, R. P. Jadeja, Y.-C. Hung and Y. Zhao, *ACS Appl. Mater. Interfaces*, 2013, **5**, 2085-2095.
11. P. Basnet and Y. Zhao, *Journal of Materials Chemistry A*, 2014, **2**, 911-914.
12. D. G. Nocera, *Accounts of Chemical Research*, 2012, **45**, 767-776.
13. H. Tong, S. X. Ouyang, Y. P. Bi, N. Umezawa, M. Oshikiri and J. H. Ye, *Advanced Materials*, 2012, **24**, 229-251.
14. R. Asahi, T. Morikawa, H. Irie and T. Ohwaki, *Chemical Reviews*, 2014, **114**, 9824-9852.
15. X. Zhang, Y. L. Chen, R.-S. Liu and D. P. Tsai, *Reports on Progress in Physics*, 2013, **76**, 046401.
16. S. J. A. Moniz, S. A. Shevlin, D. J. Martin, Z.-X. Guo and J. Tang, *Energy & Environmental Science*, 2015, **8**, 731-759.
17. L. Liao, Q. Zhang, Z. Su, Z. Zhao, Y. Wang, Y. Li, X. Lu, D. Wei, G. Feng, Q. Yu, X. Cai, J. Zhao, Z. Ren, H. Fang, F. Robles-Hernandez, S. Baldelli and J. Bao, *Nature Nanotechnology*, 2014, **9**, 69-73.
18. T. Hisatomi, J. Kubota and K. Domen, *Chemical Society Reviews*, 2014, **43**, 7520-7535.
19. J. Tian, Y. Sang, G. Yu, H. Jiang, X. Mu and H. Liu, *Advanced Materials*, 2013, **25**, 5075-5080.
20. J. Li and N. Wu, *Catalysis Science & Technology*, 2015, **5**, 1360-1384.
21. G. Liu, Y. Zhao, C. Sun, F. Li, G. Q. Lu and H.-M. Cheng, *Angewandte Chemie-International Edition*, 2008, **47**, 4516-4520.
22. F.-t. Li, X.-j. Wang, Y. Zhao, J.-x. Liu, Y.-j. Hao, R.-h. Liu and D.-s. Zhao, *Applied Catalysis B-Environmental*, 2014, **144**, 442-453.

23. G. Yang, T. Wang, B. Yang, Z. Yan, S. Ding and T. Xiao, *Appl Surf Sci*, 2013, **287**, 135-142.
24. M. Xing, Y. Wu, J. Zhang and F. Chen, *Nanoscale*, 2010, **2**, 1233-1239.
25. Z. Xiong and X. S. Zhao, *Journal of the American Chemical Society*, 2012, **134**, 5754-5757.
26. A. Kudo and Y. Miseki, *Chemical Society Reviews*, 2009, **38**, 253-278.
27. X. Chen, C. Li, M. Gratzel, R. Kostecki and S. S. Mao, *Chemical Society Reviews*, 2012, **41**, 7909-7937.
28. M. Hara, T. Kondo, M. Komoda, S. Ikeda, J. N. Kondo, K. Domen, M. Hara, K. Shinohara and A. Tanaka, *Chemical Communications*, 1998, 357-358.
29. G. Ren, D. Hu, E. W. C. Cheng, M. A. Vargas-Reus, P. Reip and R. P. Allaker, *International Journal of Antimicrobial Agents*, 2009, **33**, 587-590.
30. J. C. Park, J. Kim, H. Kwon and H. Song, *Advanced Materials*, 2009, **21**, 803-807.
31. B. K. Meyer, A. Polity, D. Reppin, M. Becker, P. Hering, P. J. Klar, T. Sander, C. Reindl, J. Benz, M. Eickhoff, C. Heiliger, M. Heinemann, J. Bläsing, A. Krost, S. Shokovets, C. Müller and C. Ronning, *physica status solidi (b)*, 2012, **249**, 1487-1509.
32. P. Y. Yu and M. Cardona, *Fundamentals of Semiconductors: Physics and Materials Properties*, Fourth edn., Springer, New York, 2010.
33. M. M. Cohen, *Introduction to the Quantum Theory of Semiconductors*, Gordon & Breach
Ltd., London, 1972.
34. J.-P. Colinge and C. A. Colinge, *Physics of Semiconductor Devices*, Springer, New York, 2005.
35. D. A. Neamen, *Semiconductor physics and devices: Basic principles*, Fourth edn., McGraw-Hill, New York, 2012.
36. C. Kittel, *Introduction to solid state physics*, Eighth edn., Wiley, 2005.
37. A. L. Linsebigler, G. Q. Lu and J. T. Yates, *Chemical Reviews*, 1995, **95**, 735-758.
38. A. Mills and S. LeHunte, *Journal of Photochemistry and Photobiology a-Chemistry*, 1997, **108**, 1-35.
39. S. J. A. Moniz, S. A. Shevlin, D. J. Martin, Z.-X. Guo and J. Tang, *Energy & Environmental Science*, 2015.
40. S. M. Sze, *Semiconductor Devices*, Second edn., John Wiley & Sons, Inc., New York, 2002.
41. M. Barroso, S. R. Pendlebury, A. J. Cowan and J. R. Durrant, *Chemical Science*, 2013, **4**, 2724-2734.
42. S. R. Pendlebury, M. Barroso, A. J. Cowan, K. Sivula, J. Tang, M. Graetzel, D. Klug and J. R. Durrant, *Chemical Communications*, 2011, **47**, 716-718.
43. J. Nelson, *The Physics of Solar Cells* Imperial College Press, London, 2006.
44. A. J. Cowan and J. R. Durrant, *Chemical Society Reviews*, 2013, **42**, 2281-2293.
45. A. Hagfeldt and M. Gratzel, *Chemical Reviews*, 1995, **95**, 49-68.
46. S. Hotchandani and P. V. Kamat, *Journal of Physical Chemistry*, 1992, **96**, 6834-6839.
47. J. Jiang, K. Zhao, X. Xiao and L. Zhang, *Journal of the American Chemical Society*, 2012, **134**, 4473-4476.

48. M. Ni, M. K. H. Leung, D. Y. C. Leung and K. Sumathy, *Renewable & Sustainable Energy Reviews*, 2007, **11**, 401-425.
49. I. K. Konstantinou and T. A. Albanis, *Applied Catalysis B-Environmental*, 2004, **49**, 1-14.
50. T. Matsunaga, R. Tomoda, T. Nakajima and H. Wake, *Fems Microbiology Letters*, 1985, **29**, 211-214.
51. T. Matsunaga, R. Tomoda, T. Nakajima, N. Nakamura and T. Komine, *Applied and Environmental Microbiology*, 1988, **54**, 1330-1333.
52. Zhebo Chen, Huyen N. Dinh and E. Miller, *Photoelectrochemical Water Splitting: Standards, Experimental Methods, and Protocols*, 2013.
53. L. Wu, L.-k. Tsui, N. Swami and G. Zangari, *Journal of Physical Chemistry C*, 2010, **114**, 11551-11556.
54. S. Emin, F. F. Abdi, M. Fanetti, W. Peng, W. Smith, K. Sivula, B. Dam and M. Valant, *Journal of Electroanalytical Chemistry*, 2014, **717–718**, 243-249.
55. L. Chen, S. Shet, H. Tang, H. Wang, T. Deutsch, Y. Yan, J. Turner and M. Al-Jassim, *J Mater Chem*, 2010, **20**, 6962-6967.
56. Y.-F. Lim, C. S. Chua, C. J. J. Lee and D. Chi, *Physical chemistry chemical physics :PCCP*, 2014, **16**, 25928-25934.
57. Z. Zhang and P. Wang, *J Mater Chem*, 2012, **22**, 2456-2464.
58. Y. Park, D. Kang and K.-S. Choi, *Phys. Chem. Chem. Phys.*, 2014, **16**, 1238-1246.
59. Y. He and Y. Zhao, *Nanoscale*, 2011, **3**, 2361-2375.
60. Y. He, J. Wu and Y. Zhao, *Nano Letters*, 2007, **7**, 1369-1375.
61. W. Smith, W. Ingram and Y. P. Zhao, *Chemical Physics Letters*, 2009, **479**, 270-273.
62. W. Smith, A. Wolcott, R. C. Fitzmorris, J. Z. Zhang and Y. Zhao, *J Mater Chem*, 2011, **21**, 10792-10800.
63. Y. Zhao, *Frontiers in Energy Research*, 2014, **2**.
64. J. Fu, *Optical sensors for bacteria detection based on nanostructures fabricated by dynamic shadowing growth*, University of Georgia, 2009.
65. I. Hodgkinson, Q. H. Wu and J. Hazel, *Applied Optics*, 1998, **37**, 2653-2659.
66. R. N. Tait, T. Smy and M. J. Brett, *Thin Solid Films*, 1993, **226**, 196-201.
67. Y. Zhao, D. Ye, G.-C. Wang and T.-M. Lu, 2003, 59-73.
68. J. Steele and M. Brett, *Journal of Materials Science: Materials in Electronics*, 2007, **18**, 367-379.
69. R. W. Smith and D. J. Srolovitz, *Journal of Applied Physics*, 1996, **79**, 1448-1457.
70. G. K. Larsen, Y. He, W. Ingram, E. T. LaPaquette, J. Wang and Y. Zhao, *Nanoscale*, 2014, **6**, 9467-9476.
71. H. F. Li, A. K. Kar, T. Parker, G. C. Wang and T. M. Lu, *Nanotechnology*, 2008, **19**, 335708.
72. P. Basnet, G. K. Larsen, R. P. Jadeja, Y.-C. Hung and Y. Zhao, *ACS Appl. Mater. Interfaces*, 2013, **5**, 2085-2095.
73. W. Smith, Z. Y. Zhang and Y. P. Zhao, *J Vac Sci Technol B*, 2007, **25**, 1875-1881.
74. A. Wolcott, W. A. Smith, T. R. Kuykendall, Y. P. Zhao and J. Z. Zhang, *Small*, 2009, **5**, 104-111.
75. W. He, H.-K. Kim, W. G. Warner, D. Melka, J. H. Callahan and J.-J. Yin, *Journal of the American Chemical Society*, 2014, **136**, 750-757.

76. E. Hauser, R. J. Zirke, J. Tauc, J. J. Hauser and S. R. Nagel, *Physical Review Letters*, 1978, **40**, 1733-1736.
77. J. Tauc, Grigorov.R and A. Vancu, *Physica Status Solidi*, 1966, **15**, 627-&.
78. D. L. Wood and J. Tauc, *Phys Rev B*, 1972, **5**, 3144-&.
79. A. B. Murphy, *Solar Energy Materials and Solar Cells*, 2007, **91**, 1326-1337.
80. F.-C. Wu and R.-L. Tseng, *Journal of Hazardous Materials*, 2008, **152**, 1256-1267.
81. G. Crini, *Bioresource Technology*, 2006, **97**, 1061-1085.
82. M. Rafatullah, O. Sulaiman, R. Hashim and A. Ahmad, *Journal of Hazardous Materials*, 2010, **177**, 70-80.
83. V. K. Garg, M. Amita, R. Kumar and R. Gupta, *Dyes and Pigments*, 2004, **63**, 243-250.
84. N. Kannan and M. M. Sundaram, *Dyes and Pigments*, 2001, **51**, 25-40.
85. C. D. Woolard, J. Strong and C. R. Erasmus, *Applied Geochemistry*, 2002, **17**, 1159-1164.
86. G. McKay, G. Ramprasad and P. P. Mowli, *Water Air and Soil Pollution*, 1986, **29**, 273-283.
87. M. T. Uddin, M. A. Islam, S. Mahmud and M. Rukanuzzaman, *Journal of Hazardous Materials*, 2009, **164**, 53-60.
88. T. Robinson, G. McMullan, R. Marchant and P. Nigam, *Bioresource Technology*, 2001, **77**, 247-255.
89. I. A. W. Tan, A. L. Ahmad and B. H. Hameed, *Journal of Hazardous Materials*, 2008, **154**, 337-346.
90. X. Zhuang, Y. Wan, C. Feng, Y. Shen and D. Zhao, *Chem Mater*, 2009, **21**, 706-716.
91. A. Gürses, Ç. Doğar, S. Karaca, M. Açikyildiz and R. Bayrak, *Journal of Hazardous Materials*, 2006, **131**, 254-259.
92. M. K. Purkait, A. Maiti, S. DasGupta and S. De, *Journal of Hazardous Materials*, 2007, **145**, 287-295.
93. W. Morales, M. Cason, O. Aina, N. R. de Tacconi and K. Rajeshwar, *Journal of the American Chemical Society*, 2008, **130**, 6318-6319.
94. L. Li, M. Krissanasaeranee, S. W. Pattinson, M. Stefik, U. Wiesner, U. Steiner and D. Eder, *Chemical Communications*, 2010, **46**, 7620-7622.
95. R. Zhu, S. Cong, Y. Tian, H. Li, M. Chen, Y. Huang, Z. Zhao and Q. Li, *Chemical Communications*, 2013, **49**, 5787-5789.
96. J. A. Zhu, S. L. Wang, S. H. Xie and H. X. Li, *Chemical Communications*, 2011, **47**, 4403-4405.
97. F. Wang, C. H. Li and J. C. Yu, *Sep Purif Technol*, 2012, **91**, 103-107.
98. Y. Yan, M. Zhang, K. Gong, L. Su, Z. Guo and L. Mao, *Chem Mater*, 2005, **17**, 3457-3463.
99. Z. Yu and S. S. C. Chuang, *The Journal of Physical Chemistry C*, 2007, **111**, 13813-13820.
100. I. Langmuir, *Journal of the American Chemical Society*, 1916, **38**, 2221-2295.
101. Y. S. Ho and G. McKay, *Process Biochemistry*, 1999, **34**, 451-465.
102. B. H. Hameed, A. L. Ahmad and K. N. A. Latiff, *Dyes and Pigments*, 2007, **75**, 143-149.
103. S. Azizian, *J Colloid Interf Sci*, 2004, **276**, 47-52.

104. M. Doğan, Y. Özdemir and M. Alkan, *Dyes and Pigments*, 2007, **75**, 701-713.
105. W. T. Tsai, C. Y. Chang, C. H. Ing and C. F. Chang, *J Colloid Interf Sci*, 2004, **275**, 72-78.
106. M. Yin, C.-K. Wu, Y. Lou, C. Burda, J. T. Koberstein, Y. Zhu and S. O'Brien, *Journal of the American Chemical Society*, 2005, **127**, 9506-9511.
107. A. S. Zoolfakar, R. A. Rani, A. J. Morfa, A. P. O'Mullane and K. Kalantar-zadeh, *Journal of Materials Chemistry C*, 2014, **2**, 5247-5270.
108. M. Heinemann, B. Eifert and C. Heiliger, *Phys Rev B*, 2013, **87**, 115111.
109. H. Yu, J. Yu, S. Liu and S. Mann, *Chem Mater*, 2007, **19**, 4327-4334.
110. T. Viet Pham, M. Rao, P. Andreasson, Y. Peng, J. Wang and K. B. Jinesh, *Applied Physics Letters*, 2013, **102**, 032101.
111. H. Pang, F. Gao and Q. Lu, *Chemical Communications*, 2009, 1076-1078.
112. Y. Xu and M. A. A. Schoonen, *American Mineralogist*, 2000, **85**, 543-556.
113. J. Zhang, J. Liu, Q. Peng, X. Wang and Y. Li, *Chem Mater*, 2006, **18**, 867-871.
114. W. Chen, Z. Fan and Z. Lai, *Journal of Materials Chemistry A*, 2013, **1**, 13862-13868.
115. P. E. de Jongh, D. Vanmaekelbergh and J. J. Kelly, *J Electrochem Soc*, 2000, **147**, 486-489.
116. P. E. de Jongh, D. Vanmaekelbergh and J. J. Kelly, *Chemical Communications*, 1999, 1069-1070.
117. L. I. Bendavid and E. A. Carter, *Journal of Physical Chemistry B*, 2013, **117**, 15750-15760.
118. B. Tanto, G. Ten Eyck and T.-M. Lu, *Journal of Applied Physics*, 2010, **108**, 026107.
119. H. Zhu, W. Cao, G. K. Larsen, R. Toole and Y. Zhao, *J Vac Sci Technol B*, 2012, **30**, 030606.
120. R. Köferstein, *J Alloy Compd*, 2014, **590**, 324-330.
121. J. Rodríguez-Carvajal, *Physica B: Condensed Matter*, 1993, **192**, 55-69.
122. A. Katsifaras and N. Spanos, *J Cryst Growth*, 1999, **204**, 183-190.
123. V. Figueiredo, E. Elangovan, G. Goncalves, P. Barquinha, L. Pereira, N. Franco, E. Alves, R. Martins and E. Fortunato, *Appl Surf Sci*, 2008, **254**, 3949-3954.
124. Y. Nakano, S. Saeki and T. Morikawa, *Applied Physics Letters*, 2009, **94**, 022111.
125. Y. Li, W. Zhang, J. Niu and Y. Chen, *Acs Nano*, 2012, **6**, 5164-5173.
126. R. Asahi, T. Morikawa, T. Ohwaki, K. Aoki and Y. Taga, *Science*, 2001, **293**, 269-271.
127. X. Lang, X. Chen and J. Zhao, *Chemical Society Reviews*, 2014, **43**, 473-486.
128. S. Somasundaram, C. Raman Nair Chenthamarakshan, N. R. de Tacconi and K. Rajeshwar, *International Journal of Hydrogen Energy*, 2007, **32**, 4661-4669.
129. G. Ghadimkhani, N. R. de Tacconi, W. Chanmanee, C. Janaky and K. Rajeshwar, *Chemical Communications*, 2013, **49**, 1297-1299.
130. L. Wang, J. Ge, A. Wang, M. Deng, X. Wang, S. Bai, R. Li, J. Jiang, Q. Zhang, Y. Luo and Y. Xiong, *Angewandte Chemie International Edition*, 2014, **53**, 5107-5111.
131. A. Houas, H. Lachheb, M. Ksibi, E. Elaloui, C. Guillard and J. M. Herrmann, *Applied Catalysis B-Environmental*, 2001, **31**, 145-157.
132. S. Chen and L.-W. Wang, *Chem Mater*, 2012, **24**, 3659-3666.

133. D. H. Evans, K. M. Oconnell, R. A. Petersen and M. J. Kelly, *Journal of Chemical Education*, 1983, **60**, 290-293.
134. J. Sawai, *J. Microbiol. Methods*, 2003, **54**, 177-182.
135. G. F. Fu, P. S. Vary and C. T. Lin, *Journal of Physical Chemistry B*, 2005, **109**, 8889-8898.
136. P. C. Maness, S. Smolinski, D. M. Blake, Z. Huang, E. J. Wolfrum and W. A. Jacoby, *Appl. Environ. Microbiol.*, 1999, **65**, 4094-4098.
137. Q. L. Li, S. Mahendra, D. Y. Lyon, L. Brunet, M. V. Liga, D. Li and P. J. J. Alvarez, *Water Research*, 2008, **42**, 4591-4602.
138. J. W. Liou and H. H. Chang, *Arch. Immunol. Ther. Exp. (Warsz.)*, 2012, 1-9.
139. S. Sakthivel, M. Janczarek and H. Kisch, *Journal of Physical Chemistry B*, 2004, **108**, 19384-19387.
140. H. A. Foster, I. B. Ditta, S. Varghese and A. Steele, *Appl. Microbiol. Biotechnol.*, 2011, **90**, 1847-1868.
141. B. M. Klahr, A. B. F. Martinson and T. W. Hamann, *Langmuir*, 2011, **27**, 461-468.
142. I. Cesar, A. Kay, J. A. Gonzalez Martinez and M. Grätzel, *Journal of the American Chemical Society*, 2006, **128**, 4582-4583.
143. N. Tran, A. Mir, D. Mallik, A. Sinha, S. Nayar and T. J. Webster, *Int. J. Nanomedicine*, 2010, **5**, 277.
144. H. Kong, J. Song and J. Jang, *Chem. Commun.*, 2010, **46**, 6735-6737.
145. T. Chen, R. Wang, L. Q. Xu, K. G. Neoh and E.-T. Kang, *Ind. Eng. Chem. Res.*, 2012, **51**, 13164-13172.
146. P. Sultana, S. Das, A. Bhattacharya, R. Basu and P. Nandy, *Mat. Sci. Eng. C*, 2012.
147. A. Azam, A. S. Ahmed, M. Oves, M. S. Khan, S. S. Habib and A. Memic, *Int. J. Nanomedicine*, 2012, **7**, 6003.
148. W. Zhang, B. Rittmann and Y. Chen, *Environ. Sci. Technol.*, 2011, **45**, 2172-2178.
149. W. Zhang, J. Hughes and Y. Chen, *Appl. Environ. Microbiol.*, 2012, **78**, 3905-3915.
150. N. Lewinski, V. Colvin and R. Drezek, *Small*, 2007, **4**, 26-49.
151. B. Tanto, G. Ten Eyck and T. M. Lu, *J. Appl. Phys.*, 2010, **108**, 026107-026107-026103.
152. H. Zhu, W. Cao, G. K. Larsen, R. Toole and Y. Zhao, *J. Vac. Sci. Tech. B*, 2012, **30**, 030606-030606-030604.
153. J. R. Groza, *Nanostruct. Mater.*, 1999, **12**, 987-992.
154. X. Wen, S. Wang, Y. Ding, Z. L. Wang and S. Yang, *J. Phys. Chem. B*, 2005, **109**, 215-220.
155. L. N. Demianets, S. V. Pouchko and R. V. Gaynutdinov, *J Cryst Growth*, 2003, **259**, 165-178.
156. L. C. C. Ferraz, W. M. Carvalho, D. Criado and F. L. Souza, *ACS Appl. Mater. Interfaces*, 2012, **4**, 5515-5523.
157. M. Cornuz, M. Grätzel and K. Sivula, *Chem. Vapor Depos.*, 2010, **16**, 291-295.
158. L. Li and N. Koshizaki, *J. Mater. Chem.*, 2010, **20**, 2972-2978.
159. D. Bersani, P. Lottici and A. Montenero, *J. Raman Spectrosc.*, 1999, **30**, 355-360.
160. K. F. McCarty, *Solid State Commun.*, 1988, **68**, 799-802.
161. T. Martin, R. Merlin, D. Huffman and M. Cardona, *Solid State Commun.*, 1977, **22**, 565-567.

162. D. L. A. de Faria, S. Venâncio Silva and M. T. de Oliveira, *J. Raman Spectrosc.*, 1997, **28**, 873-878.
163. J. Glasscock, P. Barnes, I. Plumb, A. Bendavid and P. Martin, *Thin Solid Films*, 2008, **516**, 1716-1724.
164. J. Manifacier, J. Gasiot and J. Fillard, *J. Phys. E Sci. Instrum.*, 2001, **9**, 1002.
165. B. E. Yoldas and D. P. Partlow, *Thin Solid Films*, 1985, **129**, 1-14.
166. A. A. Akl, *Appl Surf Sci*, 2004, **233**, 307-319.
167. M. A. Garcia-Lobato, A. I. Martinez, M. Castro-Roman, C. Falcony and L. Escobar-Alarcon, *Physica B*, 2011, **406**, 1496-1500.
168. F. L. Souza, K. P. Lopes, P. A. P. Nascente and E. R. Leite, *Solar Energy Materials and Solar Cells*, 2009, **93**, 362-368.
169. J. D. Desai, H. M. Pathan, S. K. Min, K. D. Jung and O. S. Joo, *Appl Surf Sci*, 2006, **252**, 2251-2258.
170. Z. Zhang, M. F. Hossain and T. Takahashi, *Appl. Catal. B*, 2010, **95**, 423-429.
171. G.-Y. Zhang, Y. Feng, Y.-Y. Xu, D.-Z. Gao and Y.-Q. Sun, *Materials Research Bulletin*, 2012, **47**, 625-630.
172. A. Kay, I. Cesar and M. Grätzel, *J. Am. Chem. Soc.*, 2006, **128**, 15714-15721.
173. Q.-X. Gao, X.-F. Wang, J.-L. Di, X.-C. Wu and Y.-R. Tao, *Catal. Sci Tech.*, 2011, **1**, 574-577.
174. X. Liu, J. Liu, Z. Chang, X. Sun and Y. Li, *Catal. Comm.*, 2011, **12**, 530-534.
175. Y. Zheng, Y. Cheng, Y. Wang, F. Bao, L. Zhou, X. Wei, Y. Zhang and Q. Zheng, *J. Phys. Chem. B*, 2006, **110**, 3093-3097.
176. B. V. Reddy, F. Rasouli, M. R. Hajaligol and S. N. Khanna, *Fuel*, 2004, **83**, 1537-1541.
177. W. Weiss and W. Ranke, *Prog. Surf. Sci.*, 2002, **70**, 1-151.
178. X. Zhou, J. Lan, G. Liu, K. Deng, Y. Yang, G. Nie, J. Yu and L. Zhi, *Angew. Chem. Int. Ed.*, 2012, **51**, 178-182.
179. K. L. Hardee and A. J. Bard, *J. Electrochem. Soc.*, 1977, **124**, 215-224.
180. M. Miyauchi, A. Nakajima, T. Watanabe and K. Hashimoto, *Chem. Mater.*, 2002, **14**, 2812-2816.
181. C. Chawengkijwanich and Y. Hayata, *Int. J. Food Microbiol.*, 2008, **123**, 288-292.
182. H. A. Foster, D. W. Sheel, P. Sheel, P. Evans, S. Varghese, N. Rutschke and H. M. Yates, *J. Photochem. Photobiol. A*, 2010, **216**, 283-289.
183. X. Qiu, M. Miyauchi, K. Sunada, M. Minoshima, M. Liu, Y. Lu, D. Li, Y. Shimodaira, Y. Hosogi, Y. Kuroda and K. Hashimoto, *ACS Nano*, 2011, **6**, 1609-1618.
184. C. W. Dunnill, Z. Ansari, A. Kafizas, S. Perni, D. J. Morgan, M. Wilson and I. P. Parkin, *J. Mater. Chem.*, 2011, **21**, 11854-11861.
185. Y. Chen, A. Lu, Y. Li, L. Zhang, H. Y. Yip, H. Zhao, T. An and P. K. Wong, *Environ. Sci. Technol.*, 2011, **45**, 5689-5695.
186. W. Wang, Y. Yu, T. An, G. Li, H. Y. Yip, J. C. Yu and P. K. Wong, *Environ. Sci. Technol.*, 2012, **46**, 4599.
187. C. Wei, W. Y. Lin, Z. Zainal, N. E. Williams, K. Zhu, A. P. Kruzic, R. L. Smith and K. Rajeshwar, *Environ. Sci. Technol.*, 1994, **28**, 934-938.
188. Y. Horie, D. A. David, M. Taya and S. Tone, *Ind. Eng. Chem. Res.*, 1996, **35**, 3920-3926.

189. Y. Koizumi and M. Taya, *Biochem. Eng. J*, 2002, **12**, 107-116.
190. D. D. Sun, J. H. Tay and K. M. Tan, *Water Res.*, 2003, **37**, 3452-3462.
191. E. F. Keller and L. A. Segel, *J. Theor. Biol.*, 1971, **30**, 225-234.
192. P. Lewus and R. M. Ford, *Biotechnol. Bioeng.*, 2001, **75**, 292-304.
193. G. Gogniat, M. Thyssen, M. Denis, C. Pulgarin and S. Dukan, *FEMS Microbiol. Lett.*, 2006, **258**, 18-24.

APPENDIX A

Langmuir Isotherm: Derivation

Let us consider adsorption and desorption of the dye molecule in the aqueous-solid interface, which can be expressed as

$$\mathrm{MB} + \mathrm{S}^* \underset{K_d}{\overset{K_a}{\longleftrightarrow}} \mathrm{MBS} \tag{A1}$$

where S^* is the empty or unoccupied surface site representing WO_3 SMR array (in our case) and MB representing dye molecules in aqueous solution. The product "MBS" represents the filled surface sites of WO_3 SMR arrays with MB molecules. The double-sided arrow represents the reversible reaction. Let x_0 and x respectively represent the total number of available sites on the WO_3 SMR arrays and the occupied sites so that the fractional coverage can be expressed as,

$$\theta = \frac{x}{x_0}\text{, which satisfies: } 0 \le \theta \le 1 \tag{A2}$$

Therefore, rate of adsorption can be written as,

$$R_{ads} = K_a(1-\theta)C_0 \tag{A3}$$

where K_a is the proportionality constant and also called a rate constant for adsorption. C_0 is the initial MB concentration. Similarly, the rate of desorption can be written as

$$R_{des} = K_d\theta \tag{A4}$$

Where K_d is the rate constant for desorption. From Eqns. (A3) and (A4), for equilibrium we obtain

$$K_a(1-\theta_e)C_e = K_d\theta_e \tag{A5}$$

where θ_e and C_e are the equilibrium fractional coverage and equilibrium concentration of MB in aqueous-phase. Re-arranging Eqn. (A5), we get

$$\theta_e = \frac{KC_e}{(1+KC_e)}, \tag{A6}$$

where $K = K_a / K_d$ is called equilibrium constant. This Eqn. (A6) represents the Eqn. (1.29) introduced in Chapter 1. The Eqn. (A6) is closely related to the experimentally measured parameters. Below presents the derivation for linearized form of Langmuir Eqn. 3.2, *i.e.* used in Chapter 3 to analyze the observed results.

The total amount of MB molecules adsorbed on the WO_3 SMRs can be expressed as

$$N_{MB} = (C_0 - C_e)V \text{ mole}, \tag{A7}$$

where V is the total volume of the MB solution. If each MB molecule occupies an effective surface area of A_{MB}, the total WO_3 surface area covered by MB molecules is $A_e = N_{MB}\, N_A A_{MB}$ (N_A is the Avogadro's number). The equilibrium surface coverage θ_e in terms of the total surface area of the WO_3 SMRs, S_{tot} can be estimated as

$$\theta_e = \frac{N_A\, A_{MB}\, (C_0 - C_e)\, V}{S_{tot}}. \tag{A8}$$

Equating Eqns. (A6) and (A8), we obtain,

$$\frac{KC_e}{(1+KC_e)} = \frac{N_A\, A_{MB}\, (C_0 - C_e)\, V}{S_{tot}}. \tag{A9}$$

Eqn. (A9) can be re-written as

$$\frac{KC_e}{(1+KC_e)} = q_e (N_A\, A_{MB} / S), \tag{A10}$$

where S is the specific area of the adsorbent that can be defined as the ratio of total surface area (S_{tot}) to the mass (m) of adsorbent (m^2/g). q_e is defined in Eqn. (3.1). After simple arrangement, Eqn. (A10) takes the form

$$\frac{C_e}{q_e} = \frac{1}{Q_m K} + \left(\frac{1}{Q_m}\right) C_e, \tag{A11}$$

where $Q_m = (S / N_A A_{MB})$ has the same unit as q_e; and it can be defined as the maximum amount of solute adsorbed onto the WO_3 surface per unit mass of adsorbent (mg/g or mol/g). Eqn. (A11) above is a well-known linearized Langmuir isotherm used to describe the gas adsorption on solids, and it was previously derived by Langmuir with a different method. Note that Eqn. (A10) or (A11) can also be used to determine the specific surface area of the nanostructure.

APPENDIX B

IPCE: Derivation

Background. IPCE results can be utilized to obtain a better understanding of the measured wavelength dependent photocurrent density (of a semiconductor photocatalyst, in this case). Thus, we will estimate and compare the IPCE% for different wavelengths depending on the photocatalyts' light bandgap.

IPCE %, from its literal definition, $\text{Quantum yield} = \dfrac{\#\text{ of carriers, } n}{\#\text{ of photons, } N}$

Note that the both the quantities in numerator and enumerator can be divide by the area

$$\phi = \frac{e\,n}{e\,N} = \frac{e\,n/s}{e\,N/s} = \frac{I(\text{amp})/cm^2}{(e\,N/s)/cm^2} \tag{B1}$$

Incident power, *p(λ)*

$$p\left(\frac{J}{s\,cm^2}\text{or}\frac{w}{cm^2}\right) = N\,h\,\upsilon = N\,h\frac{c}{\lambda} = N\,(6.62\times10^{-34}\,Js)\,\frac{3\times10^8\,(m/s)}{\lambda(m)\times10^{-9}\,nm}$$

$$\frac{N}{s\,cm^2} = \frac{Power\,(w/cm^2)\times\lambda(m)\times10^8}{19.86} = \frac{Power\,(w/cm^2)\times\lambda(nm)\times10^{17}}{19.86} \tag{B2}$$

Substituting Eqn. (B2) to Eqn. (B1), we can write

$$\phi = \frac{I(\text{amp}/cm^2)\times19.86}{e\times p\,(\text{w}/cm^2)\,\lambda(nm)10^{17}} = \frac{I(\text{amp}/cm^2)\times19.86}{1.6\times10^{-19}\times p\,(\text{w}/cm^2)\,\lambda(nm)10^{17}}$$

$$= \frac{I\,(\mathrm{amp}/cm^2)}{p\,(\mathrm{w}/cm^2)} \times \frac{1240}{\lambda(nm)} \times 100 \qquad \text{(B3)}$$

Now, if the area of the light beam is the same for the electrode and diode (see Fig. 2.6 and 2.7), Eqn. (B3) takes the form,

$$IPCE\,\% = \frac{I\,(\mathrm{amp})}{p\,(\mathrm{w})} \times \frac{1240}{\lambda(nm)} \times 100 \qquad \text{(B4)}$$

Eqn. (B4) is the same as Eqn. (2.6).

APPENDIX C

Bacteria-diffusion Modeling

The one-dimensional chemotaxis model for bacterial diffusion is given by

$$\frac{\partial b}{\partial t} = -\frac{\partial}{\partial x}(-D\frac{\partial b}{\partial x} + \chi b\frac{\partial c}{\partial x}), \tag{C1}$$

where $b(x, t)$ is the bacteria concentration, D is the bacterial diffusion coefficient, χ is the chemotactic sensitivity coefficient, and $c(x, t)$ is the chemoattractant concentration. If we assume that both D and are χ constant over the region of interest and the chemoattractant gradient has no curvature, $\frac{\partial^2 c}{\partial x^2} = 0$, we can write

$$\frac{\partial b}{\partial t} = D\frac{\partial^2 b}{\partial x^2} - \chi^* \frac{\partial b}{\partial x}, \tag{C2}$$

where χ^* is the chemotactic sensitivity coefficient that has been multiplied by the chemoattractant gradient. This is the one-dimensional advection equation for $b(x, t)$. Using the well-known coordinate transformation, $\xi \rightarrow x - \chi^* t$, the advection equation can be written as

$$\frac{\partial b}{\partial t} = D\frac{\partial^2 b}{\partial \xi^2}, \tag{C3}$$

where Eqn. (C3) is the one-dimensional diffusion equation for $b(\xi(x, t), t)$. Letting $b(\xi, t) = T(t)\,\Xi(\xi)$, the partial differential equation can be solved using the separation of variables method

$$b(\xi, t) = T(t)\,\Xi(\xi) = (a_1 e^{-D\lambda^2 t} + a_2 e^{D\lambda^2 t})(c_1 \sin\lambda\xi + c_2 \cos\lambda\xi). \tag{C4}$$

For $t \to \infty$, we have $b(\xi, t) = 0$; thus, $a_2 = 0$. Introducing the other boundary conditions is slightly more complicated. In the x coordinate we have

$$\left.\frac{\partial b}{\partial x}\right|_{x=0} = 0, \tag{C5}$$

$$\left.\frac{\partial b}{\partial x}\right|_{x=L} = -\frac{\kappa}{D} b(x = L, t), \tag{C6}$$

where κ is the bacterial inactivation rate and L is the height of the solution. Using the chain rule, we have, $\frac{\partial b}{\partial x} = \frac{\partial b}{\partial \xi}\frac{\partial \xi}{\partial x} = \frac{\partial b}{\partial \xi}$, since $\frac{\partial \xi}{\partial x} = 1$. Thus, we have for all t

$$\left.\frac{\partial b}{\partial \xi}\right|_{\xi=-\chi^* t} = 0, \tag{C7}$$

$$\left.\frac{\partial b}{\partial \xi}\right|_{\xi=L-\chi^* t} = -\frac{\kappa}{D} b(\xi = L - \chi^* t, t). \tag{C8}$$

Before proceeding with evaluating boundary conditions Eqn. (C7) and (C8), we first note that $\chi^* << 1$ since χ is typically on the order of 10^{-4} - 10^{-5} and that the concentration gradient is expected to be small, $\frac{\partial c}{\partial x} << 1$. Thus, we have $\chi^* t << 1$ for finite t. Therefore, we have the following identities for finite λ

$$\sin[\lambda(L - \chi^* t)] = \sin(\lambda L)\,\cos(\lambda\chi^* t) - \cos(\lambda L)\,\sin(\lambda\chi^* t) \approx \sin(\lambda L), \tag{C9}$$

$$\cos[\lambda(L - \chi^* t)] = \cos(\lambda L)\,\cos(\lambda\chi^* t) + \sin(\lambda L)\,\sin(\lambda\chi^* t) \approx \cos(\lambda L), \tag{C10}$$

since $\sin(\chi^* t) \approx 0$ and $\cos(\chi^* t) \approx 1$. Thus, boundary condition Eqn. (C7) implies that $c_2 = 0$. For boundary condition Eqn. (C8), we have

$$-\lambda \sin[\lambda(L - \chi^* t)] = -\frac{\kappa}{D}\cos[\lambda(L - \chi^* t)], \tag{C11}$$

$$\lambda \sin \lambda L = \frac{\kappa}{D} \cos \lambda L \ , \tag{C12}$$

$$\lambda_n = \frac{\kappa}{D} \cot \lambda_n L \ , \tag{C13}$$

where identities (C9) and (C10) were used to get Eqn. (C12) and λ_n are the eigenvalues of the solution for $b(\xi, t)$. Each λ_n is a solution to Eqn. (C13) and must be determined numerically. These solutions asymptotically approach, $\lambda_n \approx \frac{n\pi}{L}$, at a rate that depends on the magnitude of κ.

Therefore, we have

$$b(\xi,t) = \sum_{n=1}^{\infty} c_n e^{-D\lambda_n^2 t} \cos(\lambda_n \xi) , \tag{C14}$$

where $\xi = x - \chi^* t$ and λ_n is given by Eqn. (C13). Given the initial conditions, $b(\xi, 0) = b(x, 0) = b_0$, we have

$$b(\xi,0) = b_0 = \sum_{n=1}^{\infty} c_n \cos(\lambda_n \xi) , \tag{C15}$$

$$\int_0^{L-\chi^* t} b_0 \cos(\lambda_m \xi)\, d\xi = \int_0^{L-\chi^* t} \sum_{n=1}^{\infty} c_n \cos(\lambda_n \xi) \cos(\lambda_m \xi)\, d\xi , \tag{C16}$$

$$\int_0^{L-\chi^* t} b_0 \cos(\lambda_m \xi)\, d\xi = \sum_{n=1}^{\infty} \int_0^{L-\chi^* t} c_n \cos(\lambda_n \xi) \cos(\lambda_m \xi)\, d\xi , \tag{C17}$$

$$\int_0^{L-\chi^* t} b_0 \cos(\lambda_m \xi)\, d\xi = \int_0^{L-\chi^* t} c_m \cos^2(\lambda_m \xi)\, d\xi . \tag{C18}$$

We have used the orthogonality property of solutions to Sturm-Liouville equations to go from Eqn. (C17) to Eqn. (C18). Taking the integrals, using the identities (C9) and (C10), and solving for the constant c_m, we can determine the full solution:

$$b(\xi,t)=\sum_{n=1}^{\infty}c_n e^{-D\lambda_n{}^2 t}\cos(\lambda_n\xi)\,, \tag{C19}$$

where $\xi = x-\chi^* t$; $\lambda_n = \dfrac{\kappa}{D}\cot\lambda_n L$; $c_n = \dfrac{2b_0\,\lambda_n\sin\lambda_n L}{\lambda_n{}^2 L+\lambda_n\sin\lambda_n L\cos\lambda_n L}$.